Namensnennung-Keine kommerzielle Nutzung-Keine Bearbeitung 2.5 Schweiz

---

Sie dürfen:

das Werk vervielfältigen, verbreiten und öffentlich zugänglich machen

Zu den folgenden Bedingungen:

Namensnennung. Sie müssen den Namen des Autors/Rechteinhabers in der von ihm festgelegten Weise nennen (wodurch aber nicht der Eindruck entstehen darf, Sie oder die Nutzung des Werkes durch Sie würden entlohnt).

Keine kommerzielle Nutzung. Dieses Werk darf nicht für kommerzielle Zwecke verwendet werden.

Keine Bearbeitung. Dieses Werk darf nicht bearbeitet oder in anderer Weise verändert werden.

- Im Falle einer Verbreitung müssen Sie anderen die Lizenzbedingungen, unter welche dieses Werk fällt, mitteilen. Am Einfachsten ist es, einen Link auf diese Seite einzubinden.
- Jede der vorgenannten Bedingungen kann aufgehoben werden, sofern Sie die Einwilligung des Rechteinhabers dazu erhalten.
- Diese Lizenz lässt die Urheberpersönlichkeitsrechte unberührt.

Die gesetzlichen Schranken des Urheberrechts bleiben hiervon unberührt.

Die Commons Deed ist eine Zusammenfassung des Lizenzvertrags in allgemeinverständlicher Sprache: http://creativecommons.org/licenses/by-nc-nd/2.5/ch/legalcode.de

Haftungsausschluss:
Die Commons Deed ist kein Lizenzvertrag. Sie ist lediglich ein Referenztext, der den zugrundeliegenden Lizenzvertrag übersichtlich und in allgemeinverständlicher Sprache wiedergibt. Die Deed selbst entfaltet keine juristische Wirkung und erscheint im eigentlichen Lizenzvertrag nicht. Creative Commons ist keine Rechtsanwaltsgesellschaft und leistet keine Rechtsberatung. Die Weitergabe und Verlinkung des Commons Deeds führt zu keinem Mandatsverhältnis.

Quelle: http://creativecommons.org/licenses/by-nc-nd/2.5/ch/ Datum: 3.4.2009

Mechanisms of pattern processing in olfactory bulb-like circuits

Inauguraldissertation

zur Erlangung der Würde eines Doktors der Philosophie

vorgelegt der

Philosophisch-Naturwissenschaftlichen Fakultät der Universität Basel

von

Martin Takeo Wiechert

aus Rüsselsheim, Deutschland

Basel, 2010

Genehmigt von der Philosophisch-Naturwissenschaftlichen Fakultät
auf Antrag von

Prof. Dr. Silvia Arber, Dr. Rainer Friedrich und Dr. Botond Roska

Basel, den 21. September 2010

Dekan

Prof. Dr. Martin Spiess

Summary

The scope of brain research spans several orders of magnitude ranging from small groups of amino acid residues in ion channels to fMRI signals reflecting activity averaged over thousands of neurones. From a theoreticians point of view very interesting questions arise at an intermediate level of cellular but not sub-cellular resolution. How do neuronal units interact to process information? Is it possible to find general laws or a repertoire of computational motifs that would allow mastering the enormous challenge posed by the brain's sheer complexity?

Here I took advantage of the zebrafish olfactory bulb which combines a number of features that make it an ideal target for theoretical analysis. Firstly, the primary input to the olfactory bulb is known and can be administered by the experimenter, allowing for both, control over and an obvious interpretation of evoked activity. Secondly, due to the small size of the olfactory bulb (20.000—30.000 neurones) a substantial fraction of all neurones participating in an odour response can be recorded from in a single experiment. Finally, the synaptic architecture of the olfactory bulb is comparatively well-understood and simple.

In this study I used computational models to identify the structural features of the olfactory bulb that are essential to its function. In order to mechanistically understand this relation I complemented computer simulations with mathematical analysis.

It is known from large-scale imaging experiments that peripheral odour representations consisting of overlapping spatial patterns of afferent activity are transformed into less overlapping representations carried by mitral and tufted cells, the output elements of the olfactory bulb. It is hypothesised that in refining odour representations for the benefit of downstream circuits this pattern decorrelation serves an important function (see chapter 1). Interestingly, a minimalistic circuit model (chapter 1) was sufficient to reproduce most aspects of experimentally observed mitral cell responses suggesting that decorrelation in the olfactory bulb is a network phenomenon rather than a consequence of sophisticated computational properties of individual neurones. In addition, the model was mathematically tractable which allowed me to describe to a high level of detail and stringency the mechanism by which this circuit achieves universal pattern decorrelation. In the course I could explain why sparse connectivity and a high mitral cell spontaneous activity lead to effective pattern decorrelation.

In simulations I also observed that symmetric connectivity further improves decorrelation performance. In chapter 2 I present partial results towards a theoretical analysis of this effect.

I also performed computer simulations with more detailed models consisting of integrate-and-fire units. These were mostly exploratory in nature and are therefore not described in this thesis. I did, however, include technical documentation for the simulator I programmed (appendices 4 and 5) in the hope that it will be useful.

The final chapter makes a simple observation regarding odour categorisation.

Contents

Chapter 1

Mechanisms of pattern decorrelation by recurrent neuronal circuits

Nat. Neurosci. **13**, 1003—1010 (2010)

Martin T. Wiechert[1], Benjamin Judkewitz[2], Hermann Riecke[3], Rainer W. Friedrich[1]

1 Friedrich Miescher Institute for Biomedical Research, Maulbeerstr. 66, CH-4058 Basel, Switzerland

2 University College London, Wolfson Institute for Biomedical Research, Cruciform Building, Gower Street, London, WC1E 6BT, United Kingdom

3 Northwestern University, Engineering Sciences and Applied Mathematics, 2145 Sheridan Rd, Evanston, IL 60208-3101, USA

Contact:
Dr. Rainer Friedrich
Friedrich Miescher Institute for Biomedical Research
Maulbeerstr. 66
CH-4058 Basel
Switzerland
phone +41 61 69 78614
fax +41 61 69 73976
email rainer.friedrich@fmi.ch

Decorrelation is a fundamental computation that optimizes the format of neuronal activity patterns. Channel decorrelation by adaptive mechanisms results in efficient coding, whereas pattern decorrelation facilitates the readout and storage of information. Mechanisms achieving pattern decorrelation, however, remain unclear. We present a theoretical framework that relates high-dimensional pattern decorrelation to neuronal and circuit properties in a mathematically stringent fashion. We demonstrate for a generic class of random neuronal networks that pattern decorrelation emerges from neuronal nonlinearities and is amplified by recurrent connectivity. This mechanism does not require adaptation of the network, is enhanced by sparse connectivity, depends on the baseline membrane potential, and is robust. Connectivity measurements and computational modelling suggest that this mechanism is involved in pattern decorrelation in the zebrafish olfactory bulb. These results reveal a generic relationship between the structure and function of neuronal circuits that is likely relevant for pattern processing in various brain areas.

Sensory stimuli and neuronal activity often represent relevant information in a highly inefficient manner. Natural images, for example, may convey different messages even though their pixel distributions are nearly identical. A fundamental strategy to improve neuronal codes is decorrelation, which can reduce the redundancy between neuronal responses, distribute neuronal activity patterns more evenly over coding space, and enable the brain to extract information from small differences between overlapping sensory inputs. Decorrelation is therefore an important computation not only for neuronal processing[1–3], but also in engineering and computer science.

Two forms of decorrelation have to be distinguished that perform different tasks and are referred to as “channel” and “pattern” decorrelation. Channel decorrelation decreases the overlap, and thus the redundancy, between response profiles of individual channels (neurons) to a set of stimuli, resulting in a code that is “efficient” because information conveyed by different channels is largely complementary. Efficient coding has been implicated in various neuronal processing tasks[4,5]. For example, the receptive fields of neurons in primary visual cortex and the tuning of auditory nerve fibers can be described by filters that achieve channel decorrelation and result in efficient coding of natural images or sounds, respectively[6–9]. In non-neuronal systems, channel decorrelation methods including independent component analysis (ICA) have been used for blind source separation and other operations[10–13]. Most channel decorrelation methods must be adapted to a particular task based on prior knowledge about inputs. As a consequence, adaptive methods can efficiently decorrelate channels with known properties but may perform poorly on unexpected inputs.

Pattern decorrelation, in contrast, reduces the overlap between combinatorial patterns of activity across populations of neurons. Pattern decorrelation can therefore make neuronal representations more distinct, which facilitates subsequent readout by a simple classifier. In addition, decorrelated representations are most likely important for robust memory storage by associative networks because correlated representations may be confused or erased by catastrophic interference[1,2,14,15]. Pattern decorrelation has been observed experimentally in various brain areas including the olfactory bulb[16–18] and hippocampus[19], and may be involved cerebellar motor learning[20]. The mechanisms underlying pattern decorrelation are, however, not well understood.

Previous work showed that the correlation between patterns or channels can be decreased by thresholding, a fundamental nonlinearity in neuronal transfer functions imposed by the mechanism of action potential generation[20–22]. To examine pattern decorrelation, we therefore mathematically analyzed networks of randomly connected threshold-linear units. We first proved that, given normally distributed input patterns, thresholding invariably causes decorrelation. In feed-forward circuits, however, this decorrelation is accompanied by sparsening of output activity and therefore requires large numbers of output units. We then extended our analysis to recurrent networks and proved that random feedback connections amplify pattern decorrelation. Recurrent networks can therefore achieve pattern decorrelation with far fewer output units. Analysis of a simplified computational model indicated that this mechanism is likely to contribute strongly to pattern decorrelation in the olfactory bulb. These results reveal a generic, non-adaptive and biologically plausible pattern decorrelation mechanism, and provide stringent mathematical insight into the underlying principles.

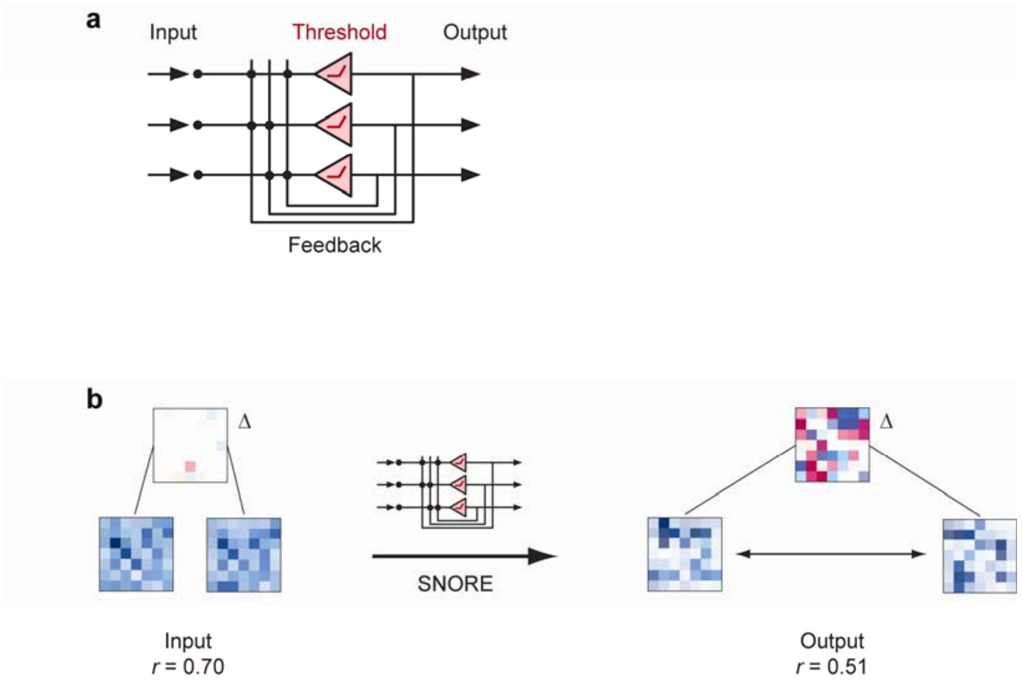

Figure 1 | Pattern decorrelation by SNOREs. **a**, Schematic illustration of a SNORE (stochastic network of rectifying elements). Red line indicates thresholding (rectification). **b**, Example of pattern decorrelation. Two random patterns across 10,000 units with correlation $r = 0.7$ were processed by a SNOREs with sparse connectivity. Images show input and output of 49 units and their differences Δ (blue: positive; red: negative). Pearson correlation coefficients r represent the similarity of the full input and output patterns.

RESULTS

Pattern decorrelation by SNOREs

To examine how networks of neurons can achieve pattern decorrelation we mathematically analyzed a generic class of recurrent networks that we call stochastic networks of rectifying elements (SNOREs; see Online Methods: Theoretical framework). SNOREs consist of threshold-linear units that are randomly connected by synapses of uniform weight (**Fig. 1a**). The output ("firing rate") of each unit is zero if its state variable ("membrane potential") is below a given threshold and linearly increases when the threshold is exceeded. We consider input patterns with joint normal intensity distribution so that pairs of input patterns are binormally distributed. The overlap between input patterns is thus parameterized by the Pearson correlation coefficient r_a. If the number of channels (neurons) is large, the overlap r_x between the corresponding steady state response patterns depends only on r_a and on the structural parameters of the SNORE. Throughout most of this study, we analyze the relationship between properties of SNOREs and their pattern decorrelation performance.

For simplicity, we will limit our presentation to purely inhibitory circuits; however, all results generalize to mixed excitatory-inhibitory SNOREs (see Online Methods: Theoretical framework and Theorems). A SNORE is then characterized by six parameters: the mean $\mu(a)$ and s.d. $\sigma(a)$ of input patterns, the absolute firing threshold η, the time constant τ, the synaptic strength λ and the number p of connections per neuron. The baseline membrane potential is included in $\mu(a)$. For a wide range of these parameters the system converges to a steady state (**Appendix A1**). The first three parameters can be condensed into a single normalized threshold $\eta_a = \dfrac{\eta - \mu(a)}{\sigma(a)}$ because the readout of interest, the correlation r_x between steady state response patterns, depends only on η_a but not on $\mu(a), \sigma(a), \eta$ individually. For example, changing the input mean $\mu(a)$ and the threshold η by a common offset will simply add the same offset to the response membrane potentials and will not affect the response firing rates. Therefore r_x only depends on the difference $\eta - \mu(a)$. Furthermore, r_x is independent of the time constant because τ has no influence on the steady state. The steady state response correlation r_x is therefore a function of the three parameters λ, p and η_a.

To explore how pattern decorrelation $r_a - r_x$ depends on these parameters we first simulated SNOREs containing 10,000 units and found that some SNOREs produced substantial pattern decorrelation (**Fig. 1b**). We noticed that pattern decorrelation depended systematically on network parameters, as shown in detail below. Briefly, decorrelation increased with the inhibition strength λ, which is expected because stronger coupling should generally enhance network effects. More surprisingly, pattern decorrelation increased with connection sparseness $1/p$ when the total coupling strength $\Lambda = -\lambda p$ (number of synapses × synaptic weight) was kept constant. Hence, networks with sparse but strong connections decorrelated input patterns more effectively than networks with dense but weak connections, even though overall activity levels remained similar. Furthermore, for networks with sufficiently strong coupling (**Appendix A1**), pattern decorrelation increased with the baseline membrane potential of the units, which is included in $\mu(a)$. This is noteworthy because in feed-forward networks correlations increase, rather than decrease, with increasing baseline membrane potential[21].

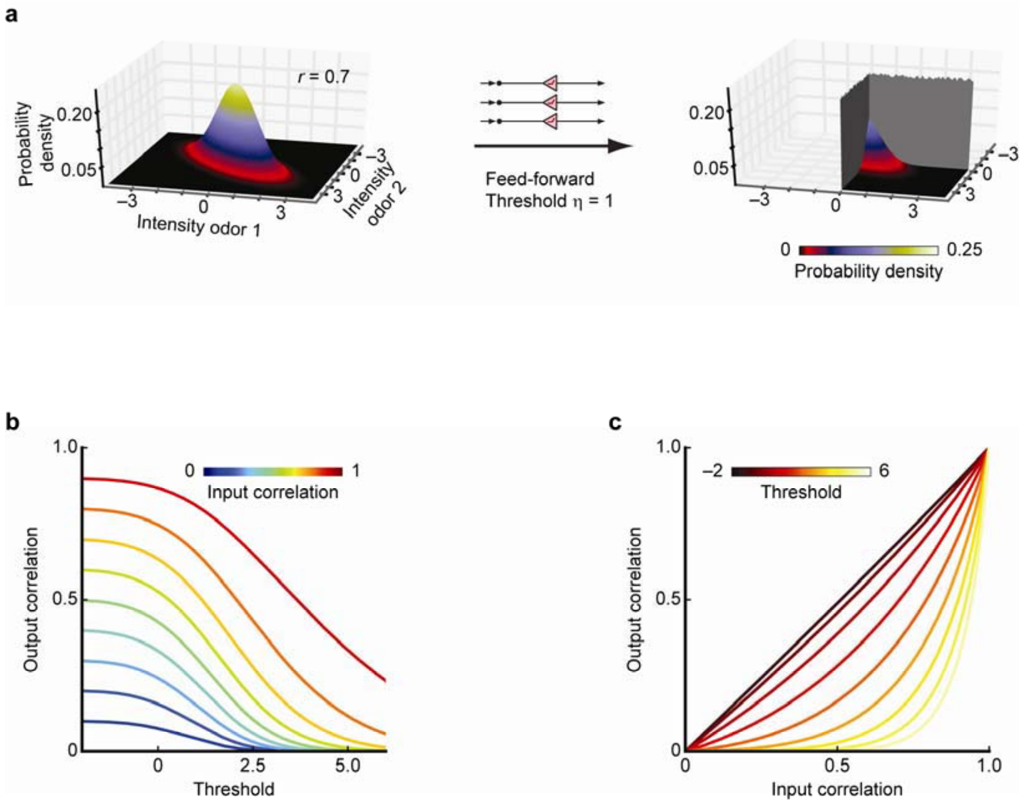

Figure 2 | Threshold-induced decorrelation (TIDe). **a**, Standard binormal probability density with correlation $r = 0.7$ before and after applying threshold $\eta = 1$. Walls indicate peaks of Dirac distributions. **b**, Output Pearson correlation as a function of threshold for different input Pearson correlations. **c**, Output Pearson correlation as a function of input Pearson correlation for different thresholds.

Mathematical analysis of pattern decorrelation by SNOREs

To understand the mechanism underlying pattern decorrelation by SNOREs and to explain its unexpected dependence on connection sparseness and baseline membrane potential we mathematically analyzed the equations describing SNOREs (see Online Methods: Theoretical framework). Since nonlinearities are known to have well-defined effects on the Pearson correlation of a given distribution[23], we first determined how pattern decorrelation depends on the threshold in the input-output function of SNORE units. For correlated jointly normally distributed input, we mathematically proved that this nonlinearity always results in decorrelation, and that decorrelation monotonically increases with the threshold level (Theorem 1 in Online Methods; **Fig. 2**). For a rigorous mathematical analysis of this threshold-induced decorrelation (TIDe) see **Appendix A1** and **Supplementary Fig. 1**. Thresholding of inputs approximates the passage through an array of neurons that do not interact with each other. Hence, a simple feed-forward array of neurons acts as a pattern decorrelator, consistent with previous observations[20,21].

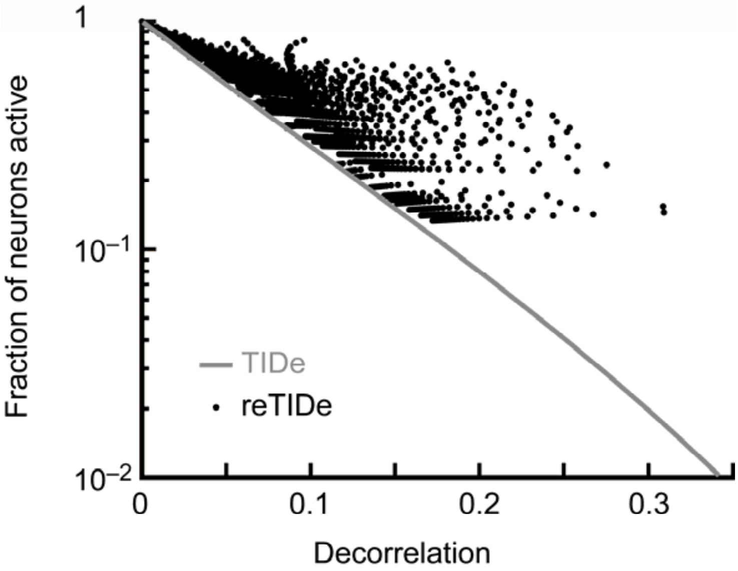

Figure 3 | Sparsening of output activity by thresholding. The fraction of active neurons is plotted against the decorrelation achieved by TIDe (gray line) and reTIDe (dots). Different dots correspond to SNOREs with different parameter combinations (see **Fig. 4e**). As decorrelation increases, the fraction of active neurons decreases systematically for TIDe, but not for reTIDe.

Increasing the threshold level can, in theory, result in arbitrarily strong decorrelation by TIDe (**Fig. 2b**,**c**). However, high thresholds will silence the majority of neurons so that a large number of neurons are required to generate meaningful output (**Fig. 3**). TIDe alone may therefore not be sufficient to achieve substantial pattern decorrelation in circuits with limited numbers of neurons.

We next analyzed how TIDe is affected by recurrent connectivity. Recurrent connections feed the thresholded, and therefore decorrelated, output patterns back into the network where they become part of the input (**Fig. 1a**). Consequently, the Pearson correlation of the total input, i.e. the sum of the external and the feedback inputs, is reduced. This in turn further decorrelates the output patterns until the steady-state is reached. We mathematically demonstrated that this effect increases the decorrelation produced by TIDe (Theorem 2 in Online Methods; for a rigorous mathematical analysis see **Appendix A1**). In recurrent networks, TIDe therefore seeds a regenerative loop that progressively amplifies pattern decorrelation (**Supplementary Fig. 2**). This recurrence-enhanced TIDe (reTIDe) is more powerful than TIDe alone and can achieve substantial decorrelation with dramatically fewer units (**Fig. 3**).

The formal proof of reTIDe is based on a mathematical theory (see Online Methods: Theoretical framework) that predicts pattern decorrelation by a SNORE from its parameters. We validated this SNORE theory against simulations and found that theoretical predictions were in excellent quantitative agreement with simulation results throughout a wide parameter range (**Fig. 4**; **Supplementary Fig. 3**). Small deviations were detected only for very sparse connectivity. This is expected because the assumption of normally distributed feedback, which depends on the central limit theorem, starts to break down in this regime (**Fig. 4e**, right).

SNORE theory can therefore be used to analytically derive relationships between network parameters and pattern decorrelation. Analysis of SNORE equations shows that reTIDe necessarily increases with connection sparseness $1/p$ when the total coupling strength Λ is kept constant (**Fig. 4a**,**e**), and that reTIDe increases with the baseline membrane potential when coupling is sufficiently strong (**Fig. 4c**,**e**; **Supplementary Fig. 3**). Hence, SNORE theory not only accurately predicts pattern decorrelation, but also analytically explains the relationships between pattern decorrelation and network parameters (see Online Methods; **Appendix A1**).

Our analytical results lead to an intuitive understanding of the dependence of pattern decorrelation on connection sparseness (**Supplementary Fig. 2**; Theorem 3.1 in Online Methods). The effectiveness of the regenerative loop underlying reTIDe depends on the relative contributions of the external input pattern and the feedback pattern to the Pearson correlation of the total input pattern. Larger variance of the feedback pattern leads to a lower Pearson correlation of the total input and, thus, enhances pattern decorrelation. In networks with dense and weak connections, the variance in the feedback pattern is low because the recurrent input to each unit is an average over many presynaptic neurons. In sparsely connected networks, in contrast, the variance can become large because each neuron averages only over a small number of recurrent inputs, resulting in more pronounced pattern decorrelation (**Supplementary Fig. 2**). For a rigorous mathematical analysis see **Appendix A1**.

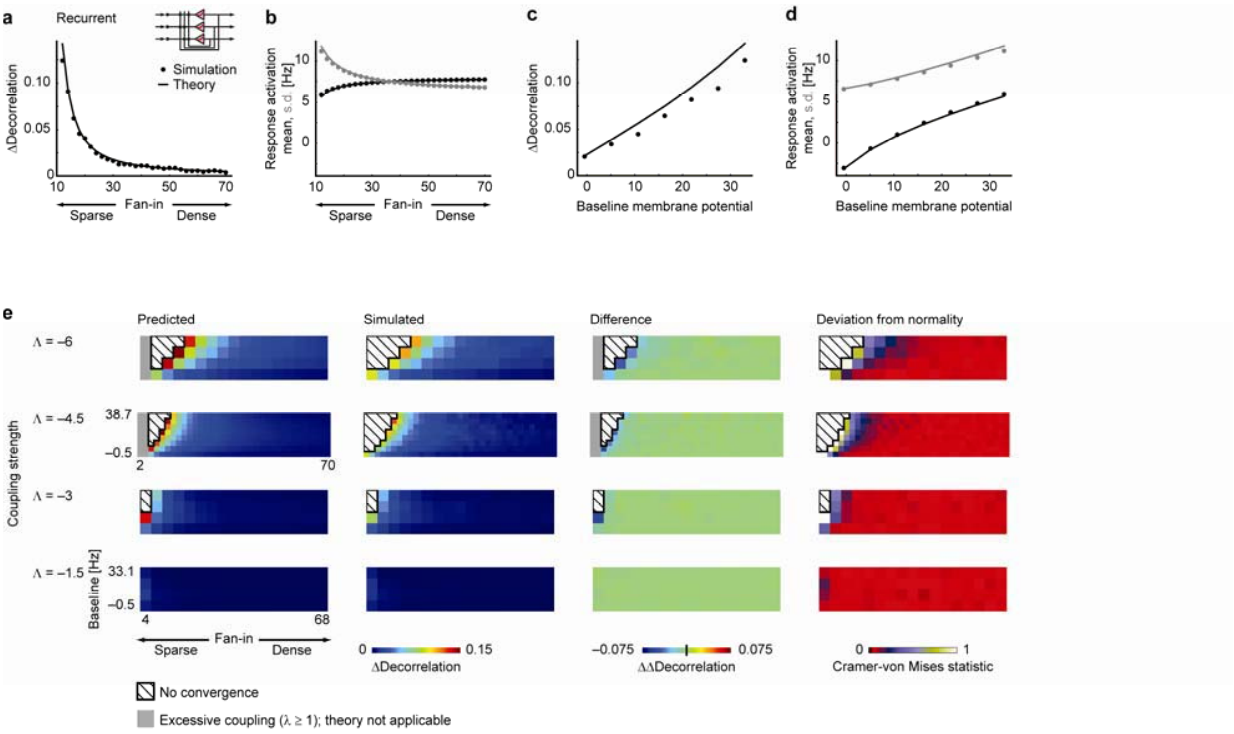

Figure 4 | Recurrence-enhanced TIDe (reTIDe). **a**, Difference in pattern decorrelation between recurrent networks (SNOREs) and feed-forward networks (Δdecorrelation) as a function of connection density (fan-in: variable p in equations). Average over the 10 most similar stimulus pairs. Lines: predictions of SNORE theory. Dots: simulation results. Baseline membrane potential $\mu(a)$ = 34.5 Hz (potentials and firing rates have the same units in the model). **b**, Mean (black) and standard deviation (gray; across units) of network activation patterns as a function of connection density. Baseline membrane potential $\mu(a)$ = 34.5 Hz. **c**, ΔDecorrelation as a function of baseline membrane potential $\mu(a)$ (in Hz). Fan-in $p = 12$. **d**, Mean (black) and standard deviation (gray) of network activity patterns as a function of baseline membrane potential ($\mu(a)$, in Hz). Fan-in $p = 12$. **e**, ΔDecorrelation for a wide range of SNORE parameter combinations. First three columns show prediction from SNORE theory, simulation results (10,000 randomly connected threshold-linear units), and their difference. Right column shows deviation of the steady-state across-population distribution of activation in simulation results from a normal distribution, quantified by the Cramer-von Mises statistic (high values indicate large deviation from normality). Note that differences between predicted and observed Δdecorrelation are well explained by departure from normality. Gray areas depict parameter combinations for which the theory is not applicable because coupling is too strong ($\lambda \geq 1$). Hatched areas depict parameter regimes where convergence to a steady-state does not occur in theoretical predictions or simulations. Note that the match between predicted and observed convergence is perfect.

The dependence of pattern decorrelation on baseline membrane potential can be understood by considering the interplay between baseline membrane potential and thresholding (Theorem 3.3 in Online Methods). Changes in baseline membrane potential have two opposing effects on reTIDe. First, when baseline membrane potential is increased, thresholding eliminates less of the variance in the input signal. As a consequence, reTIDe is enhanced because the variance in the feedback pattern is increased. Second, increasing baseline membrane potential reduces TIDe (Theorem 1.2 in Online Methods) and therefore results in less efficient seeding of reTIDe. The net effect of baseline membrane potential on reTIDe depends on the relative strengths of these opposing effects, which in turn depends on network parameters. Since the first effect scales approximately linearly with connection strength while the second effect does not, reTIDe will grow with baseline membrane potential if the network is “sufficiently coupled” (**Supplementary Fig. 3**). This regime includes most networks with sparse and strong connections. For a rigorous mathematical treatment see **Appendix A1**.

Decorrelation could also be achieved by a chaotic system but such a mechanism would be of little biological use because even minimal input corruption would result in an unpredictable change in the output. TIDe and reTIDe, by contrast, are well-conditioned, i.e. the effect small input changes have on output is limited (Therorems 1.1b and 3.2 in Online Methods; Remark M4 in **Appendix A1**). The amount of imprecision in the input that can be tolerated depends on network parameters, and there is an obvious trade-off between robustness and decorrelation. This kind of robustness facilitates pattern classification because sets of moderately similar patterns are decorrelated whereas correlations between near-identical patterns that may convey the same message are largely preserved (**Supplementary Fig. 4**).

Outputs could also be compromised by fluctuations in the units and connections of a SNORE. However, the steady states of SNOREs are linearly attractive. Departure from the fixed-point will thus be corrected for, rather than amplified, by network dynamics. In principle, multiple fixed-points might exist and fluctuations during the transient phase of the response might affect which attractor the system converges to. However, Monte-Carlo simulations indicate that there is only one, globally attractive, fixed-point (see Online Methods), consistent with the theoretical prediction that identical inputs will result in an output correlation of one. TIDe and reTIDe are therefore numerically stable, implying that they can be implemented with noisy units and connections.

Since SNORE theory applies not only to inhibitory networks but also to excitatory or mixed networks, we validated theoretical predictions of SNORE theory also in this regime. Again, we found that theoretical predictions are in excellent quantitative agreement with simulation results (**Supplementary Fig. 5**).

SNORE theory indicates that the nonlinearity in neuronal input-output functions is essential for TIDe and reTIDe. Indeed, we proved that any nonzero linear map will, on average, leave the angle between two vectors unchanged (Fact M12 and Remark M13 in **Appendix A1**). In particular, a linear adaptive method can be trained to effectively decorrelate a limited set of input patterns, but will, on average, perform poorly on unexpected inputs. Hence, TIDe and reTIDe are superior to any linear mechanism when input patterns are unpredictable.

Pattern decorrelation by a model of the olfactory bulb

To explore whether reTIDe can also explain pattern decorrelation by a biologically plausible network that lacks some of the idealizations of SNOREs we examined a computational model of the olfactory bulb, the first olfactory processing center in the brain. Structurally similar odors evoke overlapping patterns of distributed activity across the input channels of the olfactory bulb, the glomeruli[24–26], that are transformed into decorrelated activity patterns across the output neurons, the mitral cells, as shown in zebrafish[16–18]. Local GABAergic interneurons mediate inhibition between mitral cells via multiple synaptic pathways, presumably in an action potential-dependent manner[27]. We therefore first characterized the functional connectivity between mitral cells and interneurons in the zebrafish olfactory bulb by “forward optical probing”. In this approach, vigorous action potential firing is evoked in an individual mitral cell (“trigger”) by whole-cell current injection while neuronal activity in the surrounding tissue is monitored by multiphoton calcium imaging to identify functionally connected “follower” neurons.

Individual mitral cells were identified by a transgenic marker[28,29] and stimulated to fire action potentials at a rate of 30–50 Hz for one second (**Fig. 5a**,**b**; 20 repetitions). This stimulus evoked calcium signals in the soma and dendrite of the trigger neuron, as well as in sparse sets of follower neurons (**Fig. 5a**). Because mitral cells make synaptic connections predominantly onto inhibitory interneurons, neurons more than one synapse downstream of the trigger mitral cell are unlikely to be excited by the stimulus. Indeed, the majority of follower neurons (260/262; *n* = 32 trigger neurons in 20 OBs) were interneurons. The remaining two followers expressed the mitral cell marker and projected dendrites to the same glomerulus as the trigger mitral cell. These follower mitral cells were therefore likely to be connected to the trigger neuron by gap junctions or intraglomerular glutamatergic connections[30,31] and excluded from further analysis. To facilitate distance measurements in a metric that relates to inter-glomerular distances, the three-dimensional coordinates of followers were radially projected onto a sphere representing the surface of the olfactory bulb. The probability of finding a follower (connection probability) was then determined as a function of surface distance from the trigger (equivalent to their angular separation; **Fig. 5c**).

Connection probability decreased with distance in a fashion that was well fit by an exponential model (**Fig. 5d**) with a length constant (~100 μm) and maximal distance (~400 μm) that were substantially larger than the diameter of a glomerulus in the recorded region (~20 μm)[24]. The amplitude of the follower response, in contrast, decreased only slightly with distance (**Supplementary Fig. 6**), implying that the distance-dependent decay of connection probability does not reflect a decrease in coupling strength. To estimate absolute connection probability, we extrapolated the mean number of follower neurons per mitral cell (68 ± 20, mean ± s.d.; see Online Methods) and estimated the total number of interneurons in the olfactory bulb (~20,000; **Supplementary Fig. 7**). Each mitral cell is thus estimated to contact ~0.34 % of interneurons. Since the olfactory bulb contains ~1,500 mitral cells[32], each interneuron is estimated to receive approximately five mitral cell inputs detectable by

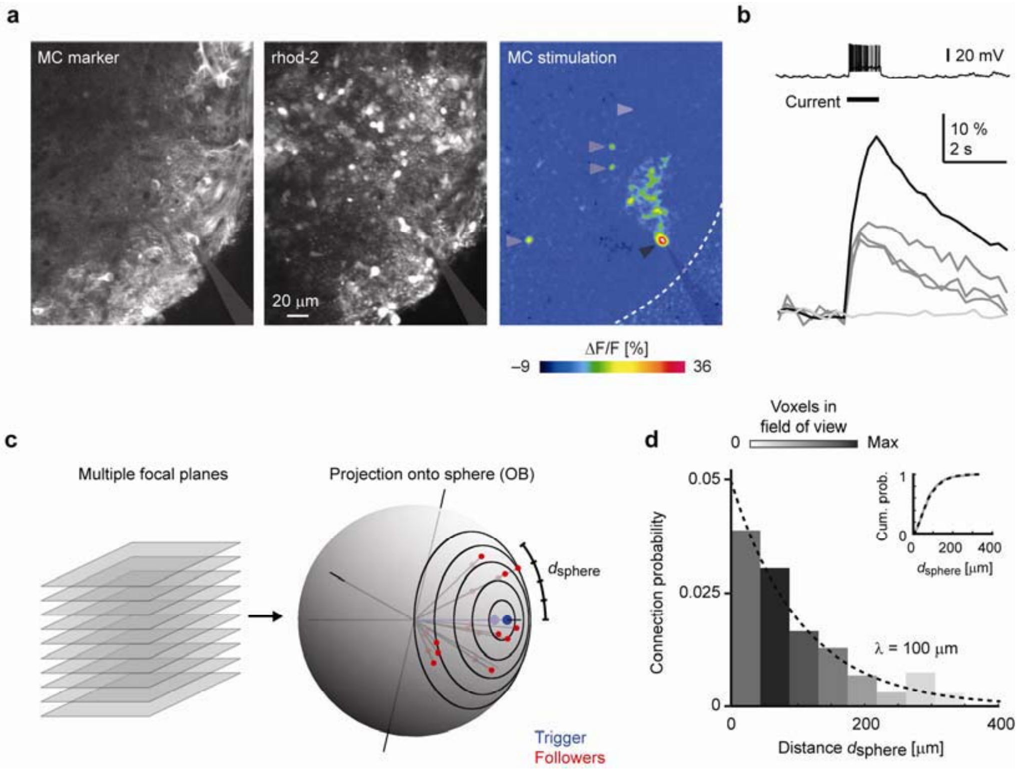

Figure 5 | Functional connectivity in the zebrafish olfactory bulb measured by forward optical probing. **a**, Left: mitral cell marker expression (HuC-YC) in an optical section through the lateral olfactory bulb. Shadow indicates patch pipette targeted onto a mitral cell (trigger neuron). Center: raw fluorescence of the calcium indicator (rhod-2) in the same view. Right: calcium signals evoked by current injection into the trigger neuron. Note strong signals in the soma and dendrites of the trigger neuron (black arrowhead) and discrete responses of three followers in the interneuron layer (medium gray arrowheads). Light gray arrowhead indicates a non-responsive region. Average over 20 repetitions. **b**, Top: example of the trigger neuron response to current injection. Bottom: time course of calcium signals in the soma of the trigger neuron (black traces), in the three followers (medium gray), and in the non-responsive region (light gray). Average over 20 repetitions. **c**, Scheme illustrating projection of follower neurons onto a sphere and measurement of the distance on the sphere (d_{sphere}). **d**, Probability of finding a follower as a function of d_{sphere}. Dashed line shows exponential fit. Data represented by darker bars are based on more voxels and weighted higher in the fit. Inset: cumulative probability distributions for measured data (solid gray line) and exponential fit (dashed black line), both corrected for limited field of view.

forward optical probing. These results indicate that strong synaptic connections between mitral cells and interneurons are sparse.

The computer model consisted of a single layer of threshold-linear analogue neurons (mitral cells) equivalent to the units in SNOREs. Mitral cells made bidirectional inhibitory synapses of uniform weight with other mitral cells, reflecting the reciprocal connectivity within the olfactory bulb (**Supplementary Fig. 8a**). Connection probability decayed exponentially with distance (**Supplementary Fig. 8b**, reference model) with a length constant of 100 μm. The model time constant was set to $\tau = 20\,\mathrm{ms}$. The model was stimulated using previously recorded glomerular afferent responses to 16 different amino acids[24] (**Supplementary Fig. 8c**; see Online Methods for details) with a stereotyped time course derived from odor responses of sensory neurons[16]. The spatial organization ("chemotopy") of measured glomerular activation patterns in the olfactory bulb was therefore directly imposed onto the model. Mitral cells were arranged in a square grid and assigned to the nearest glomerulus, or pruned if there was no detected glomerulus within a given radius. The resulting model contained a geometric arrangement of 239 mitral cells that reflected the experimentally observed pattern of glomeruli. This model differed from generic SNOREs because connections were symmetrical, because input patterns were not normally distributed, and because inputs and connections were topographically organized. Moreover, the number of mitral cells after pruning (239) was low, yet biologically realistic[16,32].

The model responded to the 16 input patterns with odor- and mitral cell-specific spatio-temporal activity patterns (**Fig. 6a**,**b**; **Supplementary Figs. 9** and **10**). We adjusted network parameters (coupling strength, connection sparseness, firing threshold, baseline membrane potential and input strength) to match the model output to experimental data at the single-neuron and population level determined previously by electrophysiology[16,17] and/or 2-photon calcium imaging[32]. The following readouts were compared quantitatively between model and experiment: mean baseline firing rate, mean odor-evoked firing rate, s.d. of odor-evoked firing rates across mitral cells, lifetime sparseness of response profiles, pattern sparseness across the mitral cell population, focality of response patterns[32], chemotopy of response patterns[32], and the mean pattern correlation evoked by the 10 most similar stimulus pairs. In addition, we qualitatively compared the response profiles of model mitral cells and their dynamics (**Supplementary Fig. 9a**) to electrophysiological data[16].

Good agreement between the model output and experimental observations was obtained with relatively strong synaptic coupling, sparse connectivity and relatively high mitral cell baseline membrane potential, consistent with experimental data from zebrafish and other vertebrates[17,33–36]. Deviations of model data from experimentally determined values were less than 25 % for all variables, and in most cases less than 10 % (**Fig. 6c**, green bars; **Supplementary Table 1**). This is not trivial considering the simplifications contained in the model and the small number of parameters. Moreover, the model reproduced many of the dynamical and topological features of odor response patterns in the zebrafish olfactory bulb[16,17,32] (**Supplementary Figs. 9–12**) and produced a gradual pattern decorrelation (**Fig. 7a**; **Supplementary Fig. 11**) similar to that observed experimentally[16–18].

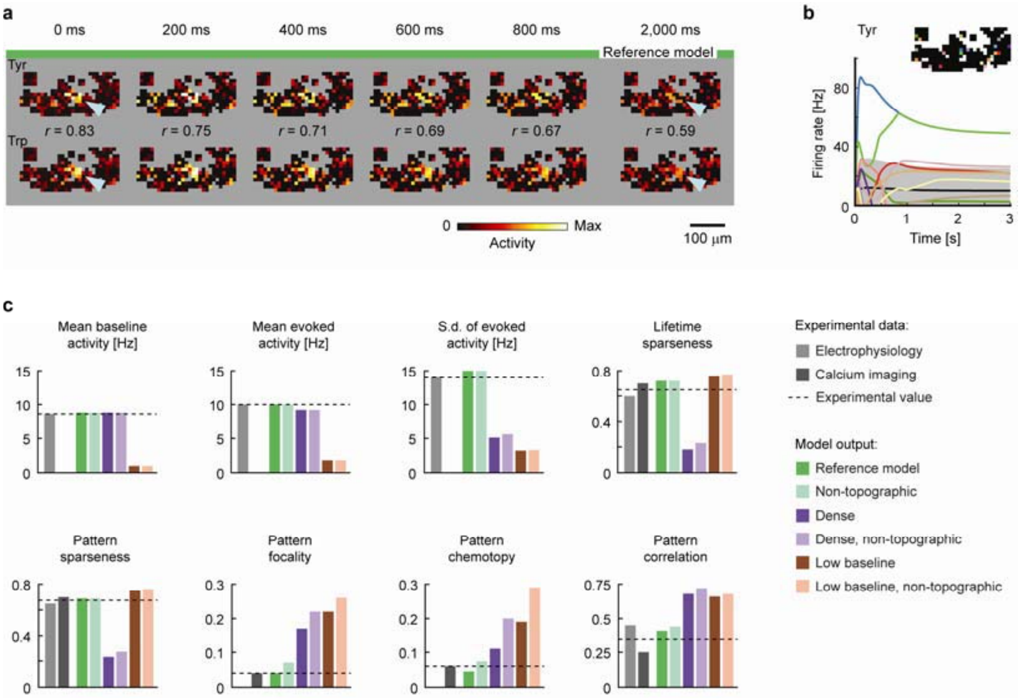

Figure 6 | Output of a computational model of the olfactory bulb. **a**, Mean output activity patterns evoked by Tyr and Trp (**Supplementary Fig. 8c**) within successive 200 ms time windows. Note that foci of active mitral cells (arrowheads) become less pronounced over time and Pearson correlation coefficients decrease. **b**, Response time courses of 20 mitral cells to stimulation with Tyr pattern. Mitral cell positions are indicated by the color code in the inset. Three mitral cells were chosen from the central cluster (arrowhead in **a**); the remaining 17 mitral cells were selected randomly. **c**, Comparison of model output to experimental data determined by electrophysiology[16,17] and/or calcium imaging[32] for eight readouts that characterize single-neuron and population activity. Dashed line shows the experimentally observed value (mean value if the same readout was measured by both methods). Model output was quantified for the reference model (green) and for models with dense connectivity (blue), low baseline membrane potential (red), and non-topographic connectivity (light colors). All values except baseline firing rate were determined in the steady state. For additional information see **Supplementary Table 1**.

In vertebrates, glomeruli responding to some molecular features are preferentially located within loosely defined regions, although not necessarily clustered[24–26]. This weakly chemotopic organization raises the possibility that decorrelation results from distance-dependent lateral inhibition between glomeruli[37], similar to edge enhancement in the retina[38]. To differentiate between such a topographic mechanism and reTIDe we tested how pattern decorrelation was affected when model parameters were modified. Pattern decorrelation, as well as other measurements, was only marginally affected when connections or glomerular positions were redistributed randomly (**Fig. 7a**, light green curve; **Fig. 6c**, light green bars; **Supplementary Figs. 9–14**). Moreover, decorrelation depended only weakly on the length constant of connection probability and was dramatically reduced by nearest-neighbor connectivity (**Fig. 7b**; **Supplementary Fig. 15**). Hence, a topographic mechanism is not required for pattern decorrelation.

Pattern decorrelation did, in contrast, strongly depend on connection sparseness and baseline membrane potential of mitral cells (**Fig. 7a**; **Supplementary Figs. 10** and **11**). Dense connectivity essentially abolished pattern decorrelation (**Fig. 7a**, purple vs. green curves; **Supplementary Figs. 10**,**11** and **13–15**). Likewise, pattern decorrelation was substantially reduced when the baseline membrane potential of mitral cells was decreased (**Fig. 7a**, brown versus green curves; **Supplementary Figs. 10**,**11** and **13–15**). These results are fully consistent with the predictions from SNORE theory and provide strong evidence that reTIDe is the primary mechanism underlying pattern decorrelation in our olfactory bulb model.

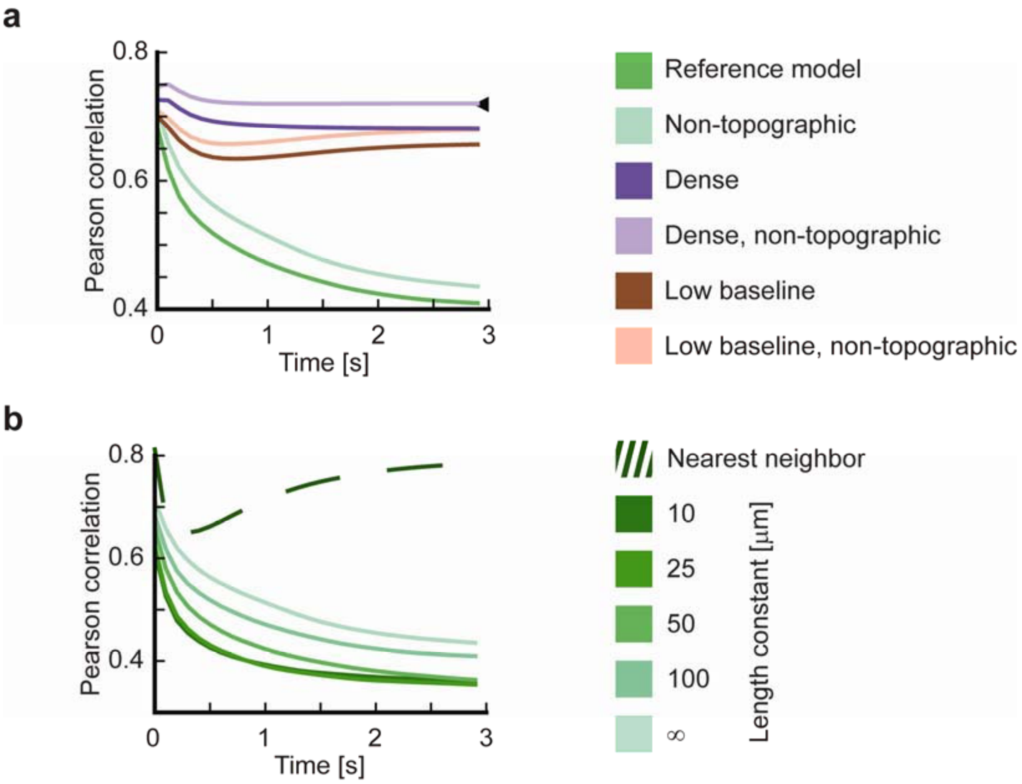

Figure 7 | Dependence of pattern decorrelation by the olfactory bulb model on topography and network parameters. **a**, Mean correlation coefficients of output activity patterns evoked by the 10 most similar stimulus pairs as a function of time for different networks. Note that pattern decorrelation by the reference model (dark green) is not substantially affected by randomizing the spatial distribution of connections (light green). However, pattern decorrelation is severely reduced when connectivity is dense (purple) or baseline membrane potential is low (red). **b**, Varying the length constant of connection probability in the sparse model showed that pattern decorrelation increased as the spatial extent of connectivity is decreased from random (infinity; light green) to narrow-range connectivity (10 µm; dark green). However, the effect was small compared to changes in connection density or baseline membrane potential (**a**). Nearest-neighbor connectivity (dashed) did not result in effective pattern decorrelation.

DISCUSSION

We describe a generic pattern decorrelation mechanism, reTIDe, that is a natural consequence of sparse and stochastic recurrent connectivity among non-linear neuronal units. Simulations indicate that reTIDe is a plausible mechanism involved in pattern decorrelation in the olfactory bulb. These results reveal basic relationships between the structure and function of neuronal circuits that are likely to be relevant for the processing of activity patterns in various brain areas.

Pattern decorrelation by reTIDe

Pattern decorrelation by reTIDe comprises two crucial steps. First, an initial decorrelation of input patterns is caused by thresholding (TIDe), which is a necessary consequence of nonlinear neuronal input-output functions. Unless the number of neurons is very high, this thresholding step alone cannot produce strong decorrelation but acts as a seed for subsequent amplification. Second, TIDe is amplified by feeding output patterns back into the network via recurrent connections (reTIDe). This amplification is particularly strong when connectivity is sparse because the variance in the feedback pattern, and therefore the contribution of the thresholded feedback pattern to the total input, is high (**Supplementary Fig. 2**). Moreover, the effectiveness of reTIDe depends on the baseline membrane potential, which is also a consequence of thresholding and subsequent amplification. ReTIDe is therefore a generic decorrelation mechanism that emerges from basic properties of recurrent circuits.

ReTIDe differs from other decorrelation strategies in at least three respects. First, while most other decorrelation mechanisms perform channel decorrelation, reTIDe performs pattern decorrelation. ReTIDe therefore reduces the overlap between neuronal population representations and facilitates the readout and storage of activity patterns.

Second, most decorrelation mechanisms must be adapted to their inputs based on prior knowledge. For example, source separation by ICA requires training of a network on representative input data[10–13], and the filter properties of auditory or visual neurons have likely been optimized for processing typical sensory input by evolution and experience[6,7,9]. Pattern decorrelation by reTIDe, in contrast, is universal and does not depend on prior adaptation of the network. As a consequence, reTIDe will decorrelate a wide range of patterns that do not need to have a specific structure. This cannot be achieved by any linear method, including adaptive strategies such as principal component-based approaches (Fact M12 and remark M13, **Appendix A1**). ReTIDe is therefore particularly useful when inputs are unpredictable, or when input patterns lack specific statistical properties.

Third, for many decorrelation mechanisms it is unclear how they may be implemented in neuronal circuits. Adaptive decorrelation strategies, for example, often rely on a global cost function that does not reflect biologically plausible learning rules. ReTIDe, in contrast, occurs in generic neuronal networks (SNOREs) and relies only on thresholding and recurrent connectivity, which are among the most basic properties of neurons and circuits in the brain. The possible biological implementation of reTIDe is therefore obvious.

Pattern decorrelation in the olfactory bulb

Forward optical probing revealed two basic features of neuronal connectivity in the zebrafish olfactory bulb. First, the weak decay of connection probability with distance implies that neuronal interactions are widespread, yet coarsely topographically organized. A field with a radius equivalent to the estimated length constant encompasses about 75 glomeruli in the lateral olfactory bulb of zebrafish, allowing for potential interactions among neurons associated with diverse sets of glomeruli. Second, connections between mitral cells and follower interneurons are sparse. This result may be biased towards strong connections because forward optical probing may fail to detect weak or silent synapses. Nevertheless, sparse connectivity in the olfactory bulb has also been inferred in rodents by transsynaptic viral tracing[34] and from the low probability of finding connected mitral-granule cell pairs[39]. Moreover, sparse functional interactions between mitral cells and glomeruli have been demonstrated in vivo[33], and sparse connectivity resulted in a good match between experimental data and our olfactory bulb model.

Our modeling results indicate that pattern decorrelation in the olfactory bulb does not depend on topographic mechanisms. Rather, efficient pattern decorrelation by our olfactory bulb model depended on sparse connectivity and high baseline membrane potential, two conserved and salient features of the olfactory bulb whose functions have been elusive. The behavior of the olfactory bulb model is therefore consistent with strong predictions of SNORE theory and the reTIDe mechanism. In principle, pattern decorrelation could also be achieved by other non-topographic mechanisms[40,41] that result in a form of histogram modification[42]. One prediction of these mechanisms is that weak mitral cell activity should be systematically suppressed whereas strong activity should be systematically preserved. Neuronal responses in the olfactory bulb and in the insect antennal lobe, however, do not generally follow this prediction[17,43]. Hence, experimental results are difficult to reconcile with these mechanisms but consistent with reTIDe. ReTIDe is therefore a plausible mechanism for pattern decorrelation in the olfactory bulb, although other mechanisms may also be involved.

Implementations and implications of TIDe and reTIDe

Classical work proposed that thresholding of convergent inputs produces a sparse and decorrelated code in the cerebellum[20], and similar mechanisms create non-overlapping and sparse odor representations in the mushroom body of insects[22,44]. These processes may represent examples of decorrelation by TIDe in circuits with large numbers of neurons. In hippocampus, pattern decorrelation occurs in the dentate gyrus[19] and its target area CA3[19,45]. Both these areas contain intra- and inter-areal recurrent connections, and connections between some neuron types are sparse[14,46]. It may therefore be interesting to explore whether pattern decorrelation in hippocampal areas involves reTIDe. In general, sparse recurrent connectivity is abundant also in neocortex[47]. Pattern decorrelation by reTIDe may thus occur not only in the olfactory bulb but also in other brain areas.

Given that reTIDe decorrelates a wide range of patterns without the need for adaptation, decorrelation by reTIDe could generally facilitate pattern discrimination and enhance the coding capacity of downstream circuits[1,3]. Moreover, reTIDe could reduce correlations among inputs to associative memory circuits in order to prevent misclassification and catastrophic interference[1,2]. These functions might, for example, be important in the olfactory bulb and dentate gyrus because their target areas –

piriform cortex and area CA3, respectively – are thought to function as associative networks for pattern storage[1,14,15].

Acknowledgements We thank Yan-Ping Zhang and Otto Fajardo for help with histological procedures, T. Oertner, B. Roska and J.M. Stix for comments on the manuscript and members of the Friedrich lab for discussions. This work was supported by the Novartis Research Foundation, the Max-Planck-Society, the Alexander-von-Humboldt Foundation, the NSF (DMS-0719944 to H.R.) the EU (IST-507610 to R.W.F.) and the DFG (SFB 488; FOR 643 to R.W.F.).

Author contributions M.T.W. performed all mathematical analyses and computational modeling and participated in writing the manuscript. B.J. performed physiological experiments and was involved in early modeling work. H.R. was involved in early stages of theoretical work and participated in writing the manuscript. R.W.F. participated in modeling, data analysis, and writing of the manuscript.

METHODS

Theoretical framework. Our theory applies to stochastic networks of rectifying elements (SNOREs) in the steady-state. Neurons are modeled as threshold-linear units, i.e. the state of cell *j* under stimulus α at time *t* is fully described by its activation $x_{j,\alpha}(t)$. We will often use the suggestive term "membrane potential" even though this term is not fully accurate in the supra-threshold regime. The instantaneous firing rate of cell *j* equals $[x_{j,\alpha}(t)-\eta_0]_+$ where η_0 and subscript "+" denote the threshold and half-wave rectification, respectively. Given the vector a_α of afferent firing rates, the vector x_α of neuronal activation and the connectivity matrix *L* the equations of motion take the form

$$(1) \qquad \tau\dot{x}_\alpha(t) = -x_\alpha(t) + a_\alpha(t) + L[x_\alpha(t)-\eta_0]_+$$

where the dot indicates the time derivative. Given a stationary stimulus α it is essential to know whether the system (1) will reach a stable steady-state

$$(2) \qquad x_\alpha = a_\alpha + L[x_\alpha - \eta_0]_+$$

For symmetrical *L* a convergence criterion based on Lyapunov functions has been given[48]. We derived a heuristic criterion (gain- and variance-limitedness) that predicts convergence to a steady-state with high accuracy for random *L* and a_α (**Appendix A1**; **Supplementary Fig. 3**).

The idea of SNORE theory is to adopt a statistical view of equation (2) and replace population vectors there with across-population distributions. We will make the simplifying assumption that each cell receives *p* recurrent contacts of strength $0 < \lambda < 1$ ($\lambda \geq 1$ leads to group-winner-take-all behavior if *L* is symmetric and inhibitory[48]) of which p_+ are excitatory and p_- inhibitory. We will also allow for global feedback of strength γ such that the total synaptic weight on each cell is $\Lambda = (p_+ - p_-)\lambda + \gamma$. In purely inhibitory networks such as the olfactory bulb, p_+ and γ vanish. If connectivity is sparse ($p^2 <<$ network size) and random, (2) leads to equations

$$\text{(3)} \qquad \mu(x_\alpha) = \mu(a_\alpha) + \Lambda\mu([x_\alpha - \eta_0]_+),$$

$$\text{(4)} \qquad \text{var}(x_\alpha) = \text{var}(a_\alpha) + P\,\text{var}([x_\alpha - \eta_0]_+) \text{ and}$$

$$\text{(5)} \qquad \text{cov}(x_\alpha, x_\beta) = \text{cov}(a_\alpha, a_\beta) + P\,\text{cov}([x_\alpha - \eta_0]_+, [x_\beta - \eta_0]_+)$$

of means, variances and covariances, respectively, each taken across the population of cells or input channels. We have abbreviated $P = p\lambda^2$. Equation (5) compares two stimuli α, β.

If the input $a = (a_\alpha, a_\beta)$ is bivariate normally distributed and $p >> 1$, then by the central limit theorem also $x = (x_\alpha, x_\beta)$ is approximately binormally distributed and thus completely determined by (3–5). Key to solving (3–5) is then to understand the effect of thresholding on the binormal distribution and its mean, variance and covariance. Using the properties of these moments, solutions to (3–5) can be tightly characterized. In particular, the dependence of pattern separation on model parameters is determined by analytical results (**Appendix A1**).

Theorems. All proofs are given in **Appendix A1**. Let ${}_{\eta,\eta}\Phi_\rho$ be the distribution obtained from the standard binormal distribution with correlation ρ by applying the threshold η to both variates.

Theorem 1 (TIDe theorem): Assume $\rho \neq \pm 1$. The Pearson correlation ${}_{\eta}r(\rho)$ of ${}_{\eta,\eta}\Phi_{\rho}$ is infinitely differentiable in ρ and η,

1. a) strictly increasing in ρ,

   b) strictly convex in ρ,

2. strictly increasing in η if $\rho < 0$ and strictly decreasing in η if $\rho > 0$ and
3. tends to zero for $\eta \to \infty$.

The most important part of this theorem is assertion 2 which states that thresholding reduces pattern overlap.

Returning to equations (3–5), let ρ_a and ρ_x be the correlation coefficients of $a = (a_\alpha, a_\beta)$ and $x = (x_\alpha, x_\beta)$, respectively, and let the stimuli α, β be of the same mean $\mu(a) = \mu(a_\alpha) = \mu(a_\beta)$ and variance $\mathrm{var}(a) = \mathrm{var}(a_\alpha) = \mathrm{var}(a_\beta)$. Then we have the following corollary of theorem 1:

Theorem 2 (reTIDe theorem): Assuming binormality of input and feedback, $0 < \rho_a < 1$ implies $\rho_x < \rho_a$.

The theorem states that without accounting for the final thresholding step $\rho_x \mapsto {}_{\eta}r(\rho_x)$ Pearson correlation is reduced. It thus isolates the gain in pattern separation of reTIDe over TIDe. This also applies to

Theorem 3: Assume $0 < \rho_a < 1$, binormality of input and feedback, and gain- and variance-limitedness (**Appendix A1**). Then

1. ρ_x is strictly decreasing in *P* and
2. strictly convex in ρ_a

If, in addition, the system is sufficiently coupled (**Appendix A1**)

3. ρ_x is strictly decreasing in $\mu(a)$.

Since parameters that are either not gain- or not variance-limited will typically not permit a steady-state (**Appendix A1**; **Supplementary Fig. 16**) the premises of theorem 3 are mild.

Making connectivity sparser while keeping Λ, γ and the excitation-inhibition ratio constant leads to larger *P*. Assertion 1 of theorem 3 therefore states that connection sparseness promotes pattern separation. In the olfactory bulb, sufficient coupling is likely to be fulfilled because connectivity is sparse and strong. Assertion 3 therefore states that higher mitral cell baseline activation promotes pattern separation in the olfactory bulb.

Forward optical probing of neuronal connectivity. Zebrafish (crosses of wild type strains Ab/Ab, Ab/TÜ or TÜ/TÜ and transgenic strain HuC:YC) were bred and kept at 26–27 °C on a 14/10 h light/dark cycle. HuC:YC transgenic fish express the fluorescent protein, yellow cameleon 2.1, in mitral cells of the adult olfactory bulb[29]. Experiments were performed in an explant preparation of the nose and brain from adult zebrafish as described[16]. All animal procedures were performed in accordance with official animal care guidelines and approved by the Federal Republic of Germany and the Veterinary Department of the Canton of Basel-Stadt (Switzerland).

Multiphoton images were acquired at 256 ms/frame (256 × 256 pixels) or 128 ms/frame (128 × 256 pixels) using a custom-built 2-photon microscope as described[28]. Whole-cell patch clamp recordings from identified mitral cells were performed using an Axoclamp 2B or Multiclamp 700B amplifier (Axon Instruments/Molecular Devices) and usually stable for 1–2 hours as assessed by changes in input resistance. All recorded trigger neurons were located in the lateral olfactory bulb, 200–300 μm dorsal from the ventral pole of the olfactory bulb. Intracellular solution contained (in mM): 130 K-gluconate, 10 Na-gluconate, 10 Na-phosphocreatine, 4 NaCl, 4 Mg-ATP, 0.3 Na-GTP, 10 HEPES (pH 7.25).

For forward optical probing, one-second current steps were injected into mitral cells at a rate of 0.1 Hz. Current amplitudes were adjusted for each mitral cell to evoke 30–50 action potentials (mean ± s.d.: 38 ± 13). At each focal plane, the stimulus was repeated 20 times. Peri-simtulus time series of 2-photon images were averaged over repetitions and images during a two second period following stimulus onset were averaged over time. The resulting image was then divided pixelwise by an image time-averaged over two seconds preceding stimulus onset to generate a 2D map of relative fluorescence changes ($\Delta F/F$).

Somata of followers were outlined manually in each focal plane. For all followers, the time course of fluorescence change was time-locked to the stimulus. A non-parametric Mann-Whitney U test was used to test that the $\Delta F/F$ values during a three second period after stimulus onset were significantly different ($P < 0.05$) from the average $\Delta F/F$ values during two seconds before stimulus onset. Potential followers that did not fulfill this criterion were excluded from the analysis.

Analysis of follower distribution. XY positions of followers were determined by the center of mass of the outlined soma. The Z position was given by the focal plane. The XYZ positions of all follower neurons were then transformed into spherical coordinates assuming a spherical olfactory bulb of 250 μm radius with its origin in the focal plane of the trigger neuron. The polar axis was defined to run through the trigger neuron. The probability of finding a follower neuron at a given polar angle was then fitted to an exponential function by minimizing the Cramer-von Mises statistic. To reduce the impact of spatial jitter, follower neurons near the center of the sphere (radius < 50 µm; <1% of all followers) were discarded. To correct for the limited field of view the following model distribution was used

$$\text{(MM1)}\ F(d) = \frac{\int_0^d e^{-\frac{x}{l}} f(x)dx}{\int_0^\pi e^{-\frac{x}{l}} f(x)dx}$$

(**Fig. 5d**; inset). Here *l* is the fit parameter, *d* is the polar angle and *f* is the relative frequency with which a voxel imaged and the trigger neuron subtended an angle of *x* at the center of the olfactory bulb. As a consequence of measurement inaccuracies we expect this procedure to overestimate the length constant. Therefore networks with smaller length constants were also simulated (**Fig. 7b**; **Supplementary Fig. 15**).

In each olfactory bulb, positive calcium signals were detected in multiple focal planes (mean ± s.d.: 5.4 ± 3.3 planes; n = 20 OBs). Two of the 262 follower neurons expressed the mitral cell marker and projected dendrites to the same glomerulus as the trigger mitral cell. These follower mitral cells were therefore likely to be connected to the trigger neuron by gap junctions or intraglomerular glutamateric connections[30,31] and excluded from further analysis.

The expected number $N_{MC} \approx 68.4$ of followers per mitral cell was calculated by the formula

$$N_{MC} = \frac{\frac{2\pi}{3} N \int_0^\pi e^{-\frac{\vartheta}{l}} \sin(\vartheta)d\vartheta}{\int_0^\pi \int_{-\pi}^\pi \int_0^1 e^{-\frac{\theta}{l}} F(r,\vartheta,\varphi) r^2 \sin(\vartheta) dr d\varphi d\vartheta}$$

where *l* is the length constant, *N* is the total number of observed followers and *F* is the number of experiments for which a given pixel (in normalised spherical coordinates r, ϑ, φ) was in the field of view. The standard deviation $SD_{MC} \approx 20.4$ was estimated by the formula

$$SD_{MC} = \sqrt{\frac{\frac{2\pi}{3}\int_0^{\pi} e^{-\frac{\vartheta}{l}}\sin(\vartheta)d\vartheta}{\int_0^{\pi}\int_{-\pi}^{\pi}\int_0^{1} e^{-\frac{\theta}{l}}F(r,\vartheta,\varphi)r^2\sin(\vartheta)dr\,d\varphi\,d\vartheta} \times \sum_i \left[N_i - \frac{N\int_0^{\pi}\int_{-\pi}^{\pi}\int_0^{1} e^{-\frac{\theta}{l}}F_i(r,\vartheta,\varphi)r^2\sin(\vartheta)dr\,d\varphi\,d\vartheta}{\int_0^{\pi}\int_{-\pi}^{\pi}\int_0^{1} e^{-\frac{\theta}{l}}F(r,\vartheta,\varphi)r^2\sin(\vartheta)dr\,d\varphi\,d\vartheta} \right]^2}$$

where summation is over trigger neurons, N_i is the number of follower neurons observed for trigger neuron *i* and F_i is the indicator function of the field of view of the corresponding experiment.

Numerical procedures and algorithms. All simulations and most analyses were run on a 3-way dual-core IBM x3755 with 16 GB RAM using custom software written in Python with time-critical subsystems implemented in C. Differential equations were solved using an adaptive step size embedded Runge-Kutta-Fehlberg (4, 5) scheme[49]. Moments of the half-wave rectified binormal distribution were obtained by adaptive numerical quadrature using a 61 point Gauss-Kronrod rule[49] on the expression

$$\begin{aligned} {}_{\eta,\kappa}M_{n,n}(\rho) &= \sum\nolimits_0^{n-1} {}_{\eta}M_{n-i}\ {}_{\kappa}M_{n-i}\frac{\rho^i}{i!} \\ &+ \int_0^{\arcsin(\rho)} e^{-\frac{1}{4}\left[\frac{(\eta+\kappa)^2}{1+\sin(\psi)}+\frac{(\eta-\kappa)^2}{1-\sin(\psi)}\right]}\frac{(\rho-\sin(\psi))^n}{2\pi n!}d\psi \end{aligned} \tag{MM2}$$

(cf. M18). Amongst other advantages this method avoids loss of significance when calculating covariances. Equations (M31, M32) were solved using the secant method.

Olfactory bulb model: connectivity matrices. Synaptic weights were uniform and contacts were drawn suppressing across-population variation of fan-in and fan-out, i.e. adjacency matrices were required to have constant row and column sums p. By the

Birkhoff-von Neumann theorem[50] any such matrix is a positive linear combination of permutation matrices M_{Π_l}. Inspecting the proof of the theorem we find that all coefficients in this linear combination can be assumed to equal one. In the case of topographic connectivity the M_{Π_l} were generated using a heuristic algorithm that strives to respect preset connection probabilities $P(j,k)$ between pairs of mitral cells x_j, x_k. The algorithm first determined a set of boundaries β_l such that the expectation $\sum_{\beta_{l-1} \le P(j,k) < \beta_l} P(j,k) - \beta_{l-1} + \sum_{P(j,k) \ge \beta_l} \beta_l - \beta_{l-1}$ was just above a half-integer multiple $\left(l - \frac{1}{2}\right)N$ of the number N of mitral cells. Starting with $l = 1$ for each "terrace" $T_l = \{(j,k) | P(j,k) \ge \beta_l\}$ an N-permutation was drawn and then shuffled into $T_l - \bigcup_{q<l} \Gamma(\Pi_q)$, i.e. random transpositions were applied until the graph $\Gamma(\Pi_l)$ of the resulting permutation Π_l was contained in $T_l - \bigcup_{q<l} \Gamma(\Pi_q)$. Here "–" indicates the relative complement which was taken to avoid collisions. To enforce convergence in acceptable time transpositions that would have increased the number of points of $\Gamma(\Pi_l)$ outside $T_l - \bigcup_{q<l} \Gamma(\Pi_q)$ were rejected. For the same reason boundaries were adjusted where necessary to ensure that terraces satisfied $\min_j \left| \{k | (j,k) \in T_l\} \right| \ge l + 2$ and $\min_k \left| \{j | (j,k) \in T_l\} \right| \ge l + 2$ with vertical bars denoting the size of a set.

To generate bidirectional synapses only even boundaries β_{2l} were considered. Permutations Π_{2l} were generated subject to the additional constraint that they have no one- or two-cycles. Π_{2l-1} was chosen to be the inverse of Π_{2l}.

Olfactory bulb model: stimulus time course. All simulations started with resting mitral cells. In most trials the stimulus was constant in time and only the mitral cell fixed point was recorded. In time resolved experiments the stimulus was modeled to evolve according to the formula

$$\text{(MM3)}\ a_j(t) = \xi + \frac{a_{j,\infty}}{1-\alpha}\left[1 - e^{-\tau_j t_+} - \alpha + \alpha e^{-\tau_d t_+}\right]$$

where ξ is a constant offset accounting for ORN/mitral cell spontaneous activity, $a_{j,\infty}$ the afferent strength after adaptation, $\alpha = 0.8$ parameterizes the degree of adaptation, τ_j and $\tau_d = \frac{1}{600}$ ms denote a rise and a decay rate, respectively. The rise rate τ_j was assumed to be proportional to $a_{j,\infty}$, consistent with electrophysiological recordings of odor responses from olfactory sensory neurons in zebrafish (RWF, unpublished observations). The proportionality factor was adjusted such that the time-to-peak ranged between 50 ms and 400 ms, as observed experimentally[16].

Artificial stimulus patterns. Multinormally distributed stimuli with the mean, variance and pairwise correlation coefficients of the 16 measured afferent patterns were obtained as follows. In a first step, half-wave rectified normal distributions approximating histograms of the 16 measured afferent patterns were determined by minimizing the Cramer-von Mises statistic. The means and variances of these distributions prior to half-wave rectification were averaged to yield $\mu(a)$ and $\sigma^2(a)$. A matrix $C(a)$ of correlation coefficients was then determined such that application of the threshold $-\frac{\mu(a)}{\sigma(a)}$ to the corresponding standard multinormal would recover the correlation coefficients between the 16 measured afferent patterns. As $C(a)$ was not positive definite, negative entries were replaced with zeroes before the Cholesky decomposition ${}^{T}UU = C(a)$ was computed. Finally, the desired pattern size N was chosen, an $N \times 16$-matrix Ξ drawn from the standard normal distribution and the columns of $\mu(a) + \sigma(a)\Xi U$ were used as artificial stimuli.

Monte Carlo simulations. Repeated simulations with different initial values were run with the 10,000 neuron network for six different parameter combinations ($p = 12,36,60; \mu(a) = 10.7,33.1; \Lambda = -4.5$). For each network the steady states reached from 128 independently drawn normally distributed (8.5 ± 100, mean ± s.d.) start vectors were computed and found to be numerically identical.

References

1. Srivastava, V., Parker, D.J. & Edwards, S.F. The nervous system might 'orthogonalize' to discriminate. *J. Theor. Biol.* **253**, 514–517 (2008).
2. French, R.M. Catastrophic forgetting in connectionist networks. *Trends Cogn. Sci.* **3**, 128–135 (1999).
3. Itskov, V. & Abbott, L.F. Pattern capacity of a perceptron for sparse discrimination. *Phys. Rev. Lett.* **101**, 018101 (2008).
4. Barlow, H.B. Possible principles underlying the transformations of sensory messages. In *Sensory communication* (ed. W.A. Rosenblith) 217–234 (MIT Press, Cambridge, MA, 1961).
5. Barlow, H. Redundancy reduction revisited. *Network* **12**, 241–253 (2001).
6. Lewicki, M.S. Efficient coding of natural sounds. *Nat. Neurosci.* **5**, 356–363 (2002).
7. Olshausen, B.A. & Field, D.J. Emergence of simple-cell receptive field properties by learning a sparse code for natural images. *Nature* **381**, 607–609 (1996).
8. Atick, J.J. & Redlich, A.N. Convergent algorithm for sensory receptive-field development. *Neural Comput.* **5**, 45–60 (1993).
9. Vinje, W.E. & Gallant, J.L. Sparse coding and decorrelation in primary visual cortex during natural vision. *Science* **287**, 1273–1276 (2000).
10. Weinstein, E., Feder, M. & Oppenheim, A.V. Multi-channel signal separation by decorrelation. *IEEE Transactions Speech Audio Proc.* **1**, 405–413 (1993).
11. Amari, S., Cichocki, A. & Yang, H.H. Recurrent neural networks for blind separation of sources. in *International symposium on nonlinear theory and its applications* 37–42 (NOLTA'95, Las Vegas, 1995).
12. Brown, G.D., Yamada, S. & Sejnowski, T.J. Independent component analysis at the neural cocktail party. *Trends Neurosci.* **24**, 54–63. (2001).
13. Parra, L.C. & Spence, C.D. Separation of non-stationary natural signals. In *Independent component analysis: principles and practice* (ed. S. Roberts & R. Everson) 135–157 (Cambridge University Press, Cambridge, MA, 2001).
14. Rolls, E.T. & Kesner, R.P. A computational theory of hippocampal function, and empirical tests of the theory. *Prog. Neurobiol.* **79**, 1–48 (2006).
15. Hasselmo, M.E., Wilson, M.A., Anderson, B.P. & Bower, J.M. Associative memory function in piriform (olfactory) cortex: computational modeling and neuropharmacology. *Cold Spring Harb. Symp. Quant. Biol.* **55**, 599–610 (1990).
16. Friedrich, R.W. & Laurent, G. Dynamic optimization of odor representations in the olfactory bulb by slow temporal patterning of mitral cell activity. *Science* **291**, 889–894 (2001).
17. Friedrich, R.W. & Laurent, G. Dynamics of olfactory bulb input and output activity during odor stimulation in zebrafish. *J. Neurophysiol.* **91**, 2658–2669 (2004).
18. Friedrich, R.W., Habermann, C.J. & Laurent, G. Multiplexing using synchrony in the zebrafish olfactory bulb. *Nat. Neurosci.* **7**, 862–871 (2004).
19. Leutgeb, J.K., Leutgeb, S., Moser, M.B. & Moser, E.I. Pattern separation in the dentate gyrus and CA3 of the hippocampus. *Science* **315**, 961–966 (2007).
20. Marr, D. A theory of cerebellar cortex. *J. Physiol.* **202**, 437–470 (1969).
21. de la Rocha, J., Doiron, B., Shea-Brown, E., Josic, K. & Reyes, A. Correlation between neural spike trains increases with firing rate. *Nature* **448**, 802–806 (2007).
22. Jortner, R.A., Farivar, S.S. & Laurent, G. A simple connectivity scheme for sparse coding in an olfactory system. *J. Neurosci.* **27**, 1659–1669 (2007).
23. Baum, R. The correlation function of Gaussian noise passed through nonlinear devices. *IEEE Transactions Inf. Theory* **15**, 448–456 (1969).
24. Friedrich, R.W. & Korsching, S.I. Combinatorial and chemotopic odorant coding in the zebrafish olfactory bulb visualized by optical imaging. *Neuron* **18**, 737–752 (1997).
25. Soucy, E.R., Albeanu, D.F., Fantana, A.L., Murthy, V.N. & Meister, M. Precision and diversity in an odor map on the olfactory bulb. *Nat. Neurosci.* **12**, 210–220 (2009).
26. Meister, M. & Bonhoeffer, T. Tuning and topography in an odor map on the rat olfactory bulb. *J. Neurosci.* **21**, 1351–1360 (2001).
27. Egger, V., Svoboda, K. & Mainen, Z.F. Dendrodendritic synaptic signals in olfactory bulb granule cells: local spine boost and global low-threshold spike. *J. Neurosci.* **25**, 3521–3530 (2005).
28. Yaksi, E. & Friedrich, R.W. Reconstruction of firing rate changes across neuronal populations by temporally deconvolved Ca^{2+} imaging. *Nat. Methods* **3**, 377–383 (2006).

29. Li, J., *et al.* Early development of functional spatial maps in the zebrafish olfactory bulb. *J. Neurosci.* **25**, 5784–5795 (2005).
30. Urban, N.N. & Sakmann, B. Reciprocal intraglomerular excitation and intra- and interglomerular lateral inhibition between mouse olfactory bulb mitral cells. *J. Physiol.* **542**, 355–367 (2002).
31. Christie, J.M., *et al.* Connexin36 mediates spike synchrony in olfactory bulb glomeruli. *Neuron* **46**, 761–772 (2005).
32. Yaksi, E., Judkewitz, B. & Friedrich, R.W. Topological reorganization of odor representations in the olfactory bulb. *PLoS Biol.* **5**, e178 (2007).
33. Fantana, A.L., Soucy, E.R. & Meister, M. Rat olfactory bulb mitral cells receive sparse glomerular inputs. *Neuron* **59**, 802–814 (2008).
34. Willhite, D.C., *et al.* Viral tracing identifies distributed columnar organization in the olfactory bulb. *Proc. Natl. Acad. Sci. USA* **103**, 12592–12597 (2006).
35. Kapoor, V. & Urban, N.N. Glomerulus-specific, long-latency activity in the olfactory bulb granule cell network. *J. Neurosci.* **26**, 11709–11719 (2006).
36. Rinberg, D., Koulakov, A. & Gelperin, A. Sparse odor coding in awake behaving mice. *J. Neurosci.* **26**, 8857–8865 (2006).
37. Yokoi, M., Mori, K. & Nakanishi, S. Refinement of odor molecule tuning by dendrodendritic synaptic inhibition in the olfactory bulb. *Proc. Natl. Acad. Sci. USA* **92**, 3371–3375 (1995).
38. Hartline, H.K. & Ratliff, F. Inhibitory interaction of receptor units in the eye of *Limulus*. *J. gen. Physiol.* **40**, 357–376 (1957).
39. Isaacson, J.S. Mechanisms governing dendritic gamma-aminobutyric acid (GABA) release in the rat olfactory bulb. *Proc. Natl. Acad. Sci. USA* **98**, 337–342 (2001).
40. Cleland, T.A. & Sethupathy, P. Non-topographical contrast enhancement in the olfactory bulb. *BMC Neurosci.* **7**, 7 (2006).
41. Arevian, A.C., Kapoor, V. & Urban, N.N. Activity-dependent gating of lateral inhibition in the mouse olfactory bulb. *Nat. Neurosci.* **11**, 80–87 (2008).
42. Hummel, R.A. Histogram modification techniques. *Comp. Graph. Image Proc.* **4**, 209–224 (1975).
43. Wilson, R.I., Turner, G.C. & Laurent, G. Transformation of olfactory representations in the Drosophila antennal lobe. *Science* **303**, 366–370 (2004).
44. Perez-Orive, J., *et al.* Oscillations and sparsening of odor representations in the mushroom body. *Science* **297**, 359–365 (2002).
45. Wills, T.J., Lever, C., Cacucci, F., Burgess, N. & O'Keefe, J. Attractor dynamics in the hippocampal representation of the local environment. *Science* **308**, 873–876 (2005).
46. Lisman, J.E. Relating hippocampal circuitry to function: recall of memory sequences by reciprocal dentate-CA3 interactions. *Neuron* **22**, 233–242 (1999).
47. Braitenberg, V. & Schüz, A. *Cortex: statistics and geometry of neuronal connectivity* (Springer, Berlin, 1998).
48. Hahnloser, R.H., Seung, H.S. & Slotine, J.J. Permitted and forbidden sets in symmetric threshold-linear networks. *Neural Comp.* **15**, 621–638 (2003).
49. Galassi, M., *et al. Gnu Scientific Library: Reference Manual* (Network Theory Ltd., 2009).
50. Bapat, R.B. & Raghavan, T.E.S. *Nonnegative Matrices and Applications* (Cambridge University Press, 1997).

Chapter 2

Consequences of reciprocal connectivity in olfactory bulb-like circuits

In chapter 1 I have used SNORE theory to link salient features of the olfactory bulb such as nonlinearity, recurrence and sparse connectivity to its presumed function as a pattern decorrelator. One prominent feature is, however, as yet absent from this list: Symmetry. Reciprocal synapses such as those occurring between mitral and granule cells in the olfactory bulb represent a stringent ordering principle with strong implications for network topology and dynamics. It is well known that symmetry can help control network dynamics and facilitate the emergence of stable steady-states[1]. Here I give numerical evidence that symmetry can also enhance pattern decorrelation and I report on first steps towards a mathematical analysis.

Let me first clarify the connection between synapse reciprocity and network symmetry. I assume that synaptic inputs sum linearly and that there are two cell types between which reciprocal synapses occur. For the sake of simplicity let us assume that reciprocity is perfect, i.e. all synapses are reciprocal with the same ratio r of weights. This means that the connectivity matrix L has the property $L = r\,{}^{T}L$. Several aspects of this kind of network have been analysed[2]. If polysynaptic connectivity can be reasonably approximated by multiplication of connectivity matrices, the disynaptic connectivity matrix L^2 which describes the same system after adiabatic elimination of one cell type is obviously symmetric. As in chapter 1 I focus on a single-layer network that is motivated by this reduced model. It should, however, be noted that the two models are not fully equivalent because I do not use Gramian connectivity matrices. As a consequence "recurrent" inhibition i.e. disynaptic self-inhibiton of mitral cells is probably underestimated.

RESULTS

Modelling

While the olfactory bulb model in chapter 1 is in fact symmetric it does not warrant a differential appraisal of the effect of symmetry because the corresponding non-symmetrical circuit does not reliably converge. Here I therefore use generic 10,000-unit SNOREs. Compared to their non-symmetric counterparts, symmetric SNOREs markedly enhance pattern decorrelation in the most favourable parameter regime of strong sparse connectivity and high baseline activation (Fig. 1).

Gross analysis

Trying to understand why symmetric connectivity systematically enhances decorrelation two major differences to the non-symmetrical model are apparent:

1. Channel correlations can no longer be neglected (Figs. 2, 3).

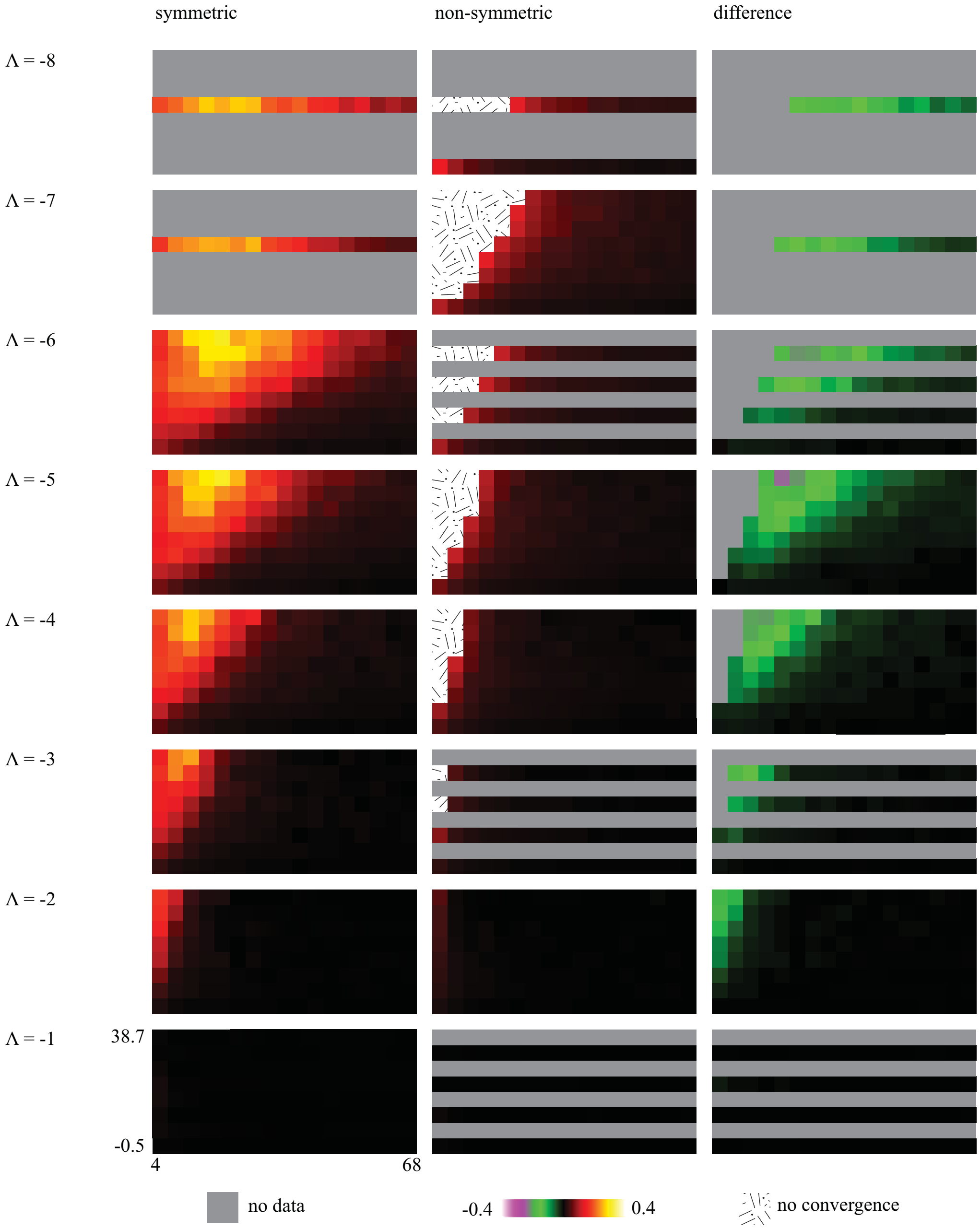

Figure 1. Gain in pattern decorrelation by symmetric connectivity in the 10,000 neurone SNORE model.

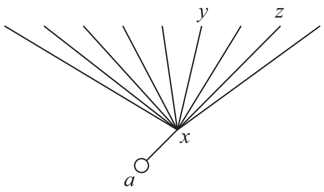

Figure 2. Presynaptic partners of a given MC *x* are not independent if connectivity is symmetric. E.g. *y* and *z* share the common input *x* and are therefore correlated.

2. The normal distribution is not a good approximation to the distribution of membrane potentials anymore. Indeed, due to the thresholded and thus nonlinear feedback each cell exerts on its presynaptic partners the central limit theorem is no longer applicable.

Normal theory—model I

I first tested whether neglecting non-normality and only accounting for channel correlations would lead to an acceptable approximation of model behaviour.

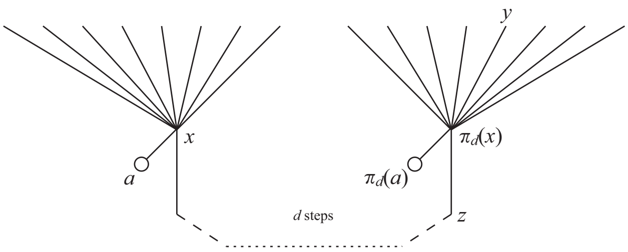

Figure 3. Channel correlation structure. MC $\pi_d(x)$ has one presynaptic partner *z* on the connecting path with *x*,*a* and $p-1$ presynaptic partners, e.g. *y*, outside the connecting path. This is true for positive path length *d*; the case $d=0$ needs to be treated specially.

If connectivity is bidirectional network mediated correlations between (poly-) synaptically connected channels must be accounted for. I will assume that the network is sparse by which I mean that the effect of (graph-theoretical) cycles can be neglected. Denote by $C_d(\rho_a)=r(x_\alpha,\pi_d(x)_\beta)$ the correlation coefficient between response patterns to ρ_a-correlated stimuli α and β of MCs shifted by *d* synapses. Here π_d is a permutation that takes each MC to an MC *d* synapses away. More precisely, let $\{\Pi_l\}_{l\in\{1,\dots,p\}}$ be the permutations described in section "Olfactory bulb model: connectivity matrices" in chapter 1, methods, such that $L=\lambda\sum_{l=1}^{p}M_{\Pi_l}$. π_d can be any product without cancellations[*] of *d* factors from $\{\Pi_l\}_{l\in\{1,\dots,p\}}$. Similarly, let $B_d(\rho_a)=r(a_\alpha,\pi_d(x)_\beta)$ be the correlation coefficient between input pattern and output pattern. Note that this concept of "channel correlation" differs from the standard one in that the average is not taken over response profiles, but over the population of channels in two copies one of which is shifted by *d* synapses.

Expressing the second argument in $\operatorname{cov}(a_\alpha,\pi_d(x)_\beta)$ and $\operatorname{cov}(x_\alpha,\pi_d(x)_\beta)$ as a sum $\pi_d(x)=\pi_d(a)+\lambda\sum_{l=1}^{p}[\Pi_l\circ\pi_d(x)]_+$ over its inputs leads to (Fig. 3)

$$B_0(\rho_a)=\sigma\rho_a+p\lambda\,{}_{\eta_x}M_{1,1}(B_1(\rho_a))=\sigma\rho_a+p\lambda\,{}_{\eta_x}M_0B_1(\rho_a) \tag{1}$$

$$\begin{aligned}B_n(\rho_a)&=\lambda\,{}_{\eta_x}M_{1,1}(B_{n-1}(\rho_a))+(p-1)\lambda\,{}_{\eta_x}M_{1,1}(B_{n+1}(\rho_a))\\&=\lambda\,{}_{\eta_x}M_0[B_{n-1}(\rho_a)+(p-1)B_{n+1}(\rho_a)]\end{aligned} \tag{2}$$

$$C_0(\rho_a)=\sigma B_0(\rho_a)+p\lambda\,{}_{\eta_x}M_{1,1}(C_1(\rho_a))=\sigma B_0(\rho_a)+p\lambda\,{}_{\eta_x}M_0C_1(\rho_a) \tag{3}$$

$$\begin{aligned}C_n(\rho_a)&=\sigma B_n(\rho_a)+\lambda\,{}_{\eta_x}M_{1,1}(C_{n-1}(\rho_a))+(p-1)\lambda\,{}_{\eta_x}M_{1,1}(C_{n+1}(\rho_a))\\&=\sigma B_n(\rho_a)+\lambda\,{}_{\eta_x}M_0[C_{n-1}(\rho_a)+(p-1)C_{n+1}(\rho_a)]\end{aligned} \tag{4}$$

---

[*] Recall that in the case of symmetric connectivity $\{\Pi_l\}_{l\in\{1,\dots,p\}}$ is closed under taking inverses.

Here I have explicitly used the assumption of binormality and the notation ${}_{\eta}M_{m,n}(\rho)$ for the premoments of the univariately thresholded binormal ${}_{\eta}\Phi$ (Appendix A3).

This system is easily seen to be underdetermined. I therefore add the heuristic constraint

$$\{B_n(\rho_a)\}_n \text{ and } \{C_n(\rho_a)\}_n \text{ decay as fast as possible} \tag{5}$$

which is plausible given that both are generated by increasingly distant relations and is further justified in Appendix A3.

More significantly, however, if η_x and thus σ—which being univariate variables do not depend on input correlation—are fixed, the system (1—4) is also linear in ρ_a. Once the constraint

$$C_0(1) = 1 \tag{6}$$

is taken into account this model therefore predicts no decorrelation at all and will have to be modified to be of any use.

Still, solutions to (1—5) will be required below. The general solution to (1,2) is

$$B_n(\rho_a) = \sigma\rho_a\left[\alpha_+ B_+^n + \alpha_- B_-^n\right] \tag{7}$$

with

$$B_\pm = \frac{1 \pm \sqrt{1-(p-1)\left[2\lambda\ {}_{\eta_x}M_0\right]^2}}{2(p-1)\lambda\ {}_{\eta_x}M_0} = \frac{2\lambda\ {}_{\eta_x}M_0}{1 \mp \sqrt{1-(p-1)\left[2\lambda\ {}_{\eta_x}M_0\right]^2}}\ . \tag{8}$$

If $B_\pm$ are real as was the case for all parameter combinations we encountered α_+ must vanish by (5) such that

$$\alpha_- = \frac{1}{1 - p\lambda\ {}_{\eta_x}M_0 B_-} \tag{9}$$

by (1).

The general solution to (3,4) is

$$C_n(\rho_a)=\sigma^2\rho_a\left\{n\left[\gamma_-B_-^n+\gamma_+B_+^n\right]+\beta_-B_-^n+\beta_+B_+^n\right\} \tag{10}$$

with

$$\gamma_\pm=\frac{\alpha_\pm}{(p-1)\lambda\ {}_{\eta_x}M_0\left[B_\mp-B_\pm\right]}. \tag{11}$$

Again, (5) implies that β_+ must vanish such that by (3)

$$\beta_-=\frac{1+\dfrac{p\lambda\ {}_{\eta_x}M_0B_-}{(p-1)\lambda\ {}_{\eta_x}M_0\left[B_+-B_-\right]}}{1-p\lambda\ {}_{\eta_x}M_0B_-}\alpha_-. \tag{12}$$

Before drawing conclusions from the failure of this model to predict any decorrelation let us refine it.

Normal theory—model II

The system (1—4) is linear because of the property

$${}_\eta M_{1,1}(\rho)={}_\eta M_0\rho \tag{13}$$

of the univariately thresholded binormal which follows from (A3.3,A3.7). Expanding not only the second argument of $\operatorname{cov}\left(x_\alpha,\pi_d(x)_\beta\right)$ but both gives rise to a variant of model I where (3,4) are replaced by

$$C_0(\rho_a)=2\sigma B_0(\rho_a)-\sigma^2\rho_a+p\lambda^2\ {}_{\eta_x,\eta_x}\overline{M}_{1,1}\left(C_0(\rho_a)\right)+(p-1)p\lambda^2\ {}_{\eta_x,\eta_x}\overline{M}_{1,1}\left(C_2(\rho_a)\right) \tag{14}$$

$$\begin{aligned}C_{2n}(\rho_a)=&\,2\sigma B_{2n}(\rho_a)+\lambda^2\ {}_{\eta_x,\eta_x}\overline{M}_{1,1}\left(C_{2n-2}(\rho_a)\right)\\&+2(p-1)\lambda^2\ {}_{\eta_x,\eta_x}\overline{M}_{1,1}\left(C_{2n}(\rho_a)\right)+(p-1)^2\lambda^2\ {}_{\eta_x,\eta_x}\overline{M}_{1,1}\left(C_{2n+2}(\rho_a)\right)\end{aligned} \tag{15}$$

(3,4) in effect linearise (14,15), indeed, if using Mehler's formula the ${}_{\eta,\eta}M_{1,1}$ are truncated at first order in ρ_a, (14,15) are equivalent to (3,4).

To see whether this subtle difference can explain the failure of model I, I solved the modified system (1,2,14,15,5,6), see Appendix A3 for details.

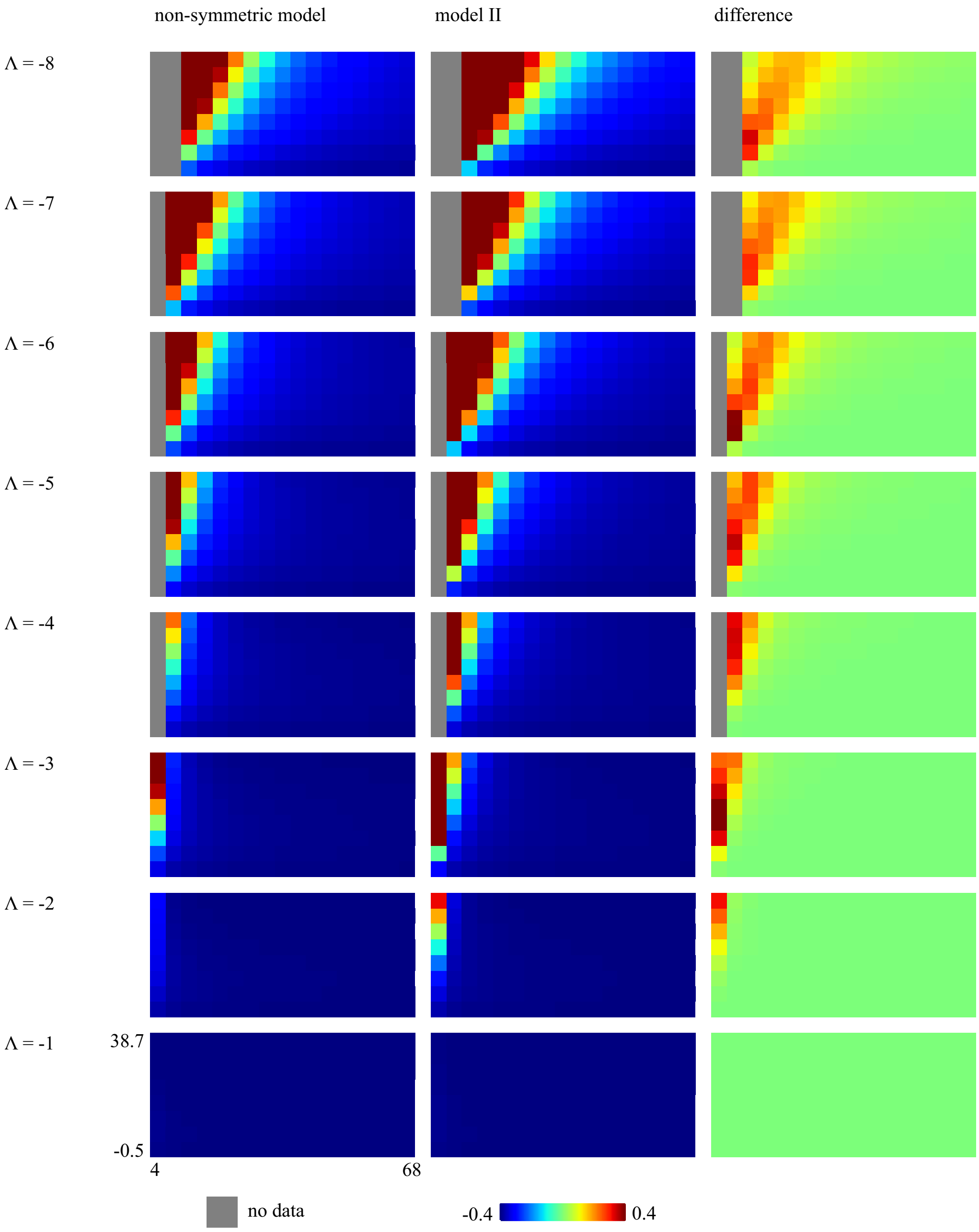

Figure 4. Symmetric vs. non-symmetric theory. Model II correctly predicts systematically improved decorrelation relative to the non-symmetric network.

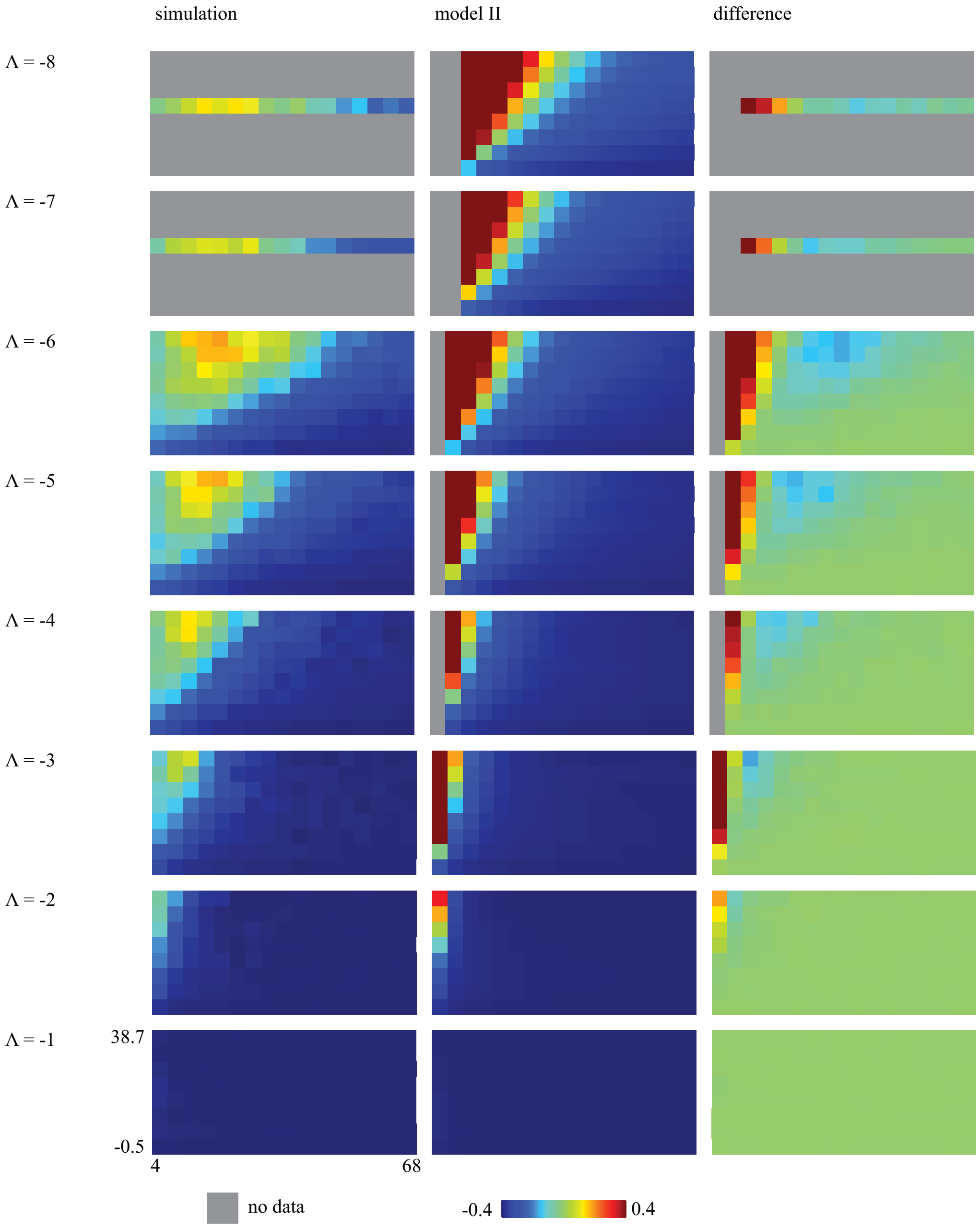

Figure 5. Prediction of decorrelation by non-normal model is poor. In the very sparse regime decorrelation is systematically overestimated. While this error is large it is also expected. More worryingly the model systematically underestimates decorrelation in the moderately sparse regime.

While model II improves on model I by correctly predicting a systematic gain in decorrelation over the non-symmetric network (Fig. 4) the quantitative match to simulation data is still poor (Fig. 5).

Non-normality

To assess how and how strongly the steady-state distribution of membrane potentials across mitral cells deviates from normality I resorted to computer simulations and prepared histograms. For some parameters the distribution is highly non-normal (Figs. 6,7). A pronounced discontinuity at the threshold is apparent. Left and right of this discontinuity a normal approximation may be good enough.

To estimate how strongly departure from normality affects correlation I compared the correlation of firing rates between different channels and stimuli to the correlation of hypothetical firing rates that results from replacing the observed bivariate membrane potential distribution by a binormal one with matching mean, variance and correlation (Figs. 8,9). The difference is considerable in the parameter range where accuracy of decorrelation predicted by model II is poor.

DISCUSSION

Before I discuss the results I outline how a better model might be obtained.

Towards a non-normal model

As a first step one should strive to well understand the observed non-normal distribution of membrane potentials. A direct ansatz would be to express it as the marginal of a high-dimensional distribution which is multinormal in each η-shifted orthant. Using the Kibble-Slepian formula[3] it might be possible to confirm that this marginal should indeed be well approximated by two Gaussians. That way one could hope to gain enough constrains governing the parameters of these Gaussians to be able to formulate and solve a self-consistent set of equations similar to (1,2,14,15).

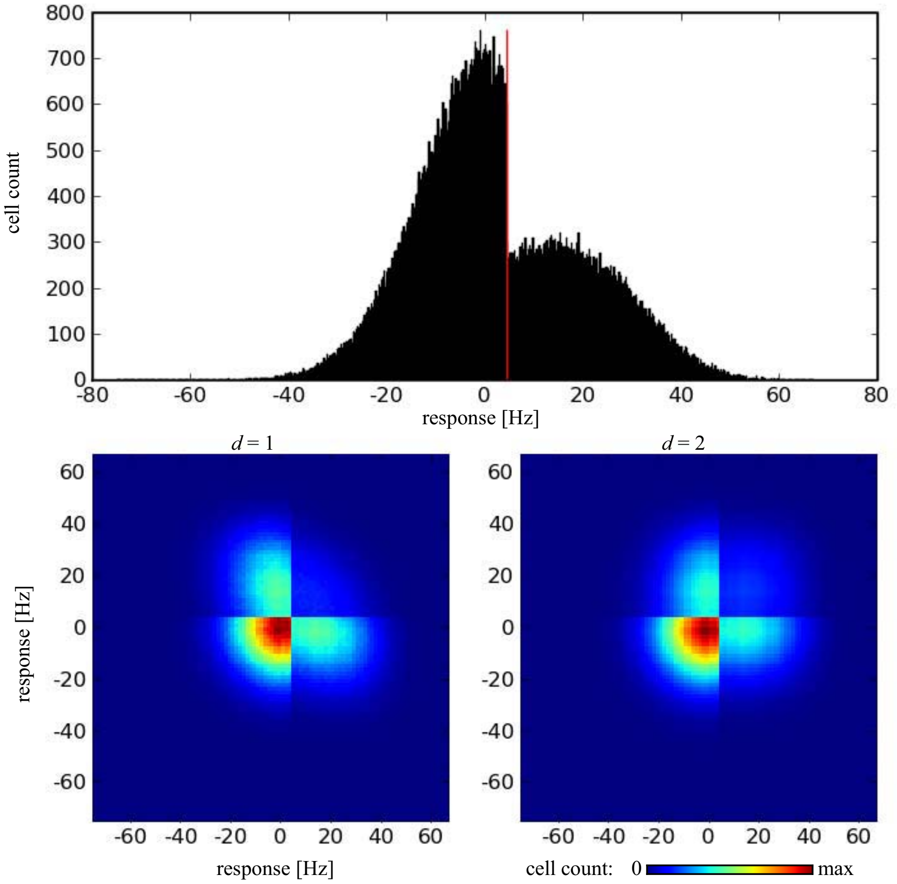

Figure 6. Distribution of steady-state membrane potentials across mitral cells. Data from computer simulation of the 10,000-neurone symmetric network pooled over the 16 amino acid stimuli; parameters: $\mu(a) = 21.9\,\text{Hz}, p = 28, \Lambda = -4$. Pronounced deviation from normality is apparent. Top panel: univariate distribution, red line indicates threshold. Bottom panel, left: bivariate distribution, same stimulus, neighbouring channels $(X, \pi_1(X))$. Bottom panel, right: bivariate distribution, same stimulus, channels two synapses apart $(X, \pi_2(X))$.

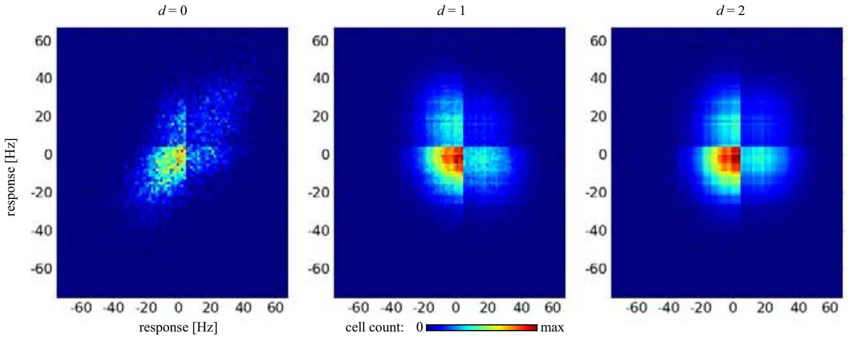

Figure 7. Distribution of steady-state membrane potentials across mitral cells. Data from computer simulation of the 10,000-neurone symmetric network; parameters as in Fig. 6. Left panel: bivariate distribution, different stimuli (Tyr, Trp), same channel. Centre panel: bivariate distribution, different stimuli, neighbouring channels $\left(X_\alpha, \pi_1\left(X_\beta\right)\right)$. Right panel: bivariate distribution, different stimuli, channels two synapses apart $\left(X_\alpha, \pi_2\left(X_\beta\right)\right)$.

Channel and pattern correlation

The match between model II and simulation results is unsatisfactory. Still, model II may be considered useful because it suggests that part of the gain in pattern correlation afforded by symmetric connectivity is explained by channel correlations, while the rest is presumably an effect of non-normality.

Bimodal distribution of membrane potentials

It is well known that the statistics of activity in a circuit can be informative about network topology [4]. In a simple sense this also holds for this model. Normally distributed membrane potentials indicate non-symmetric connections, whereas non-normally distributed membrane potentials indicate symmetric connections.

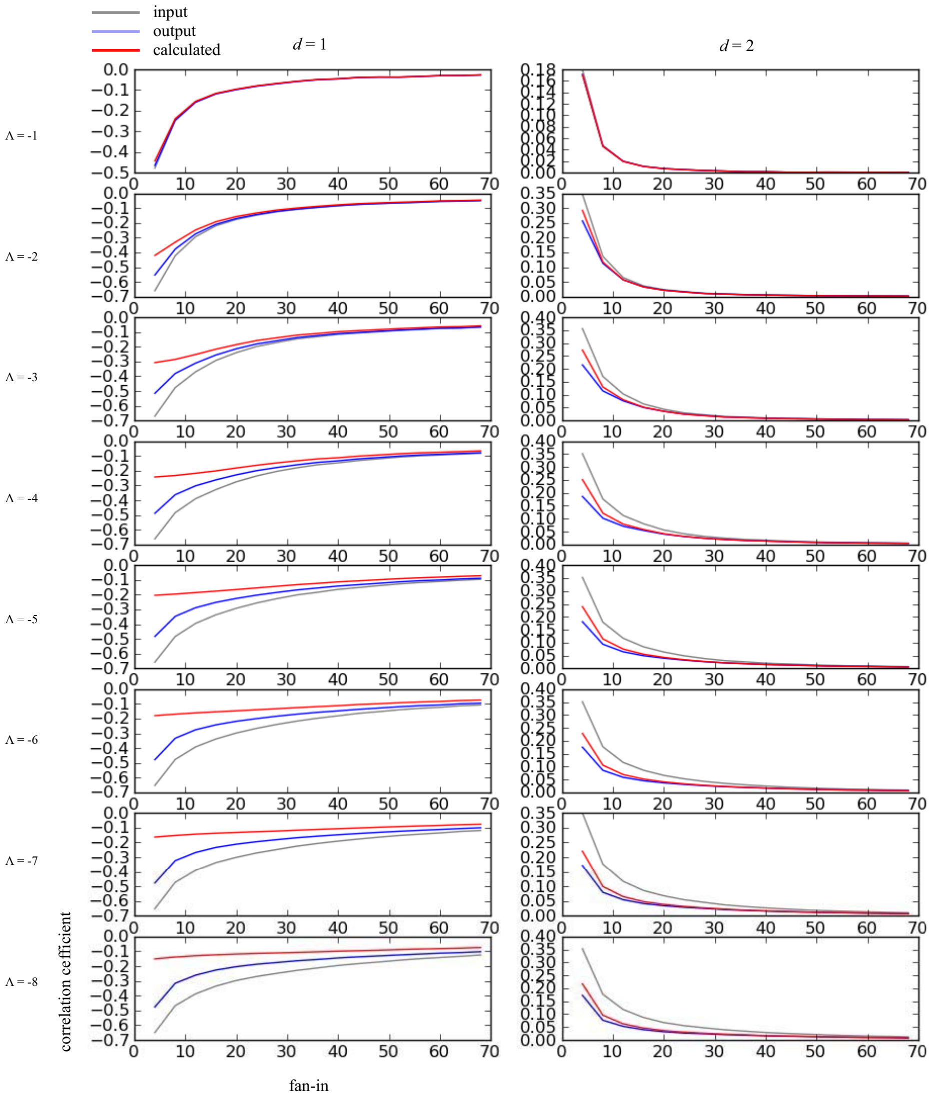

Figure 8. Channel correlation coefficient of membrane potential distributions (grey), observed distribution of firing rates (blue) and distribution of firing rates if membrane potentials were normally distributed (red). *x*-axis indicates fan-in. Connection strength ranges from 1 (top) to 8 (bottom). Channels are either neighbours (left column) or two synapses apart (right column).

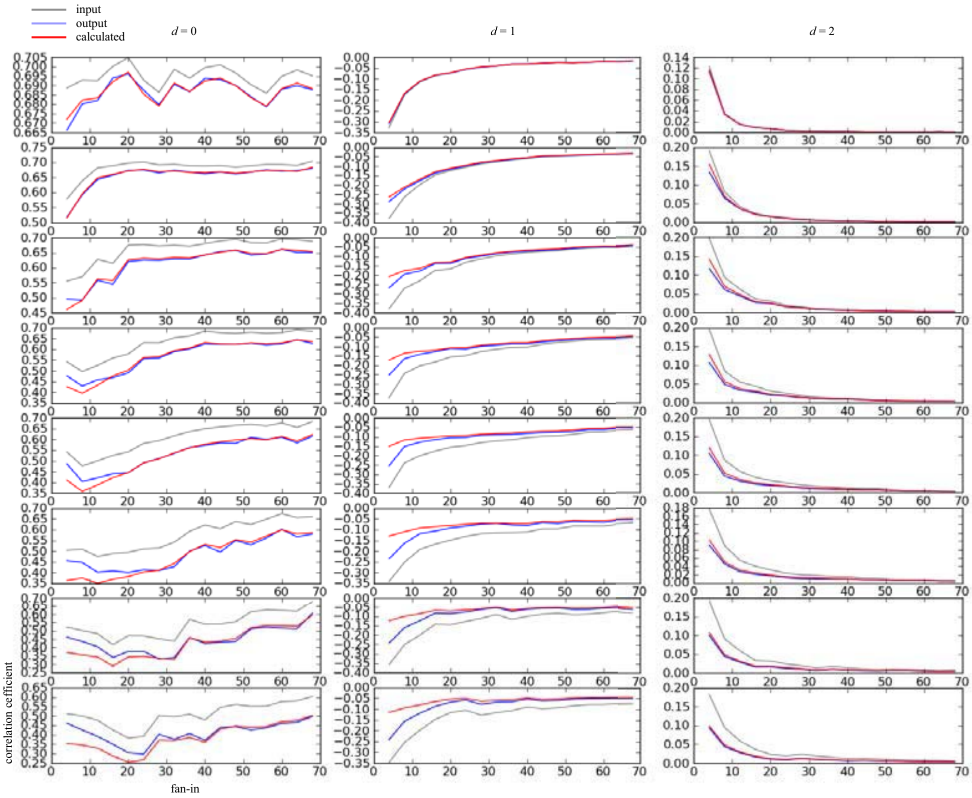

Figure 9. Correlation coefficient of membrane potential distributions (grey), observed distribution of firing rates (blue) and distribution of firing rates if membrane potentials were normally distributed (red). *x*-axis indicates fan-in. Connection strength ranges from 1 (top) to 8 (bottom). Left column: different stimuli (Tyr, Trp), same channel. Centre column: different stimuli, neighbouring channels. Right column: different stimuli, channels two synapses apart (right column).

Also, the symmetric model constitutes a simple mechanism to transform a unimodal input distribution into a pronouncedly bimodal output distribution (Fig. 10). A bimodal distribution of membrane potentials has been observed in many brain areas[5-7]. While I have no reason to believe that the symmetric model is a realistic mechanism underlying the membrane potential distribution in these areas, it is potentially useful to know that such a bimodal distribution can arise independent of intrinsic neuronal properties such as bistability.

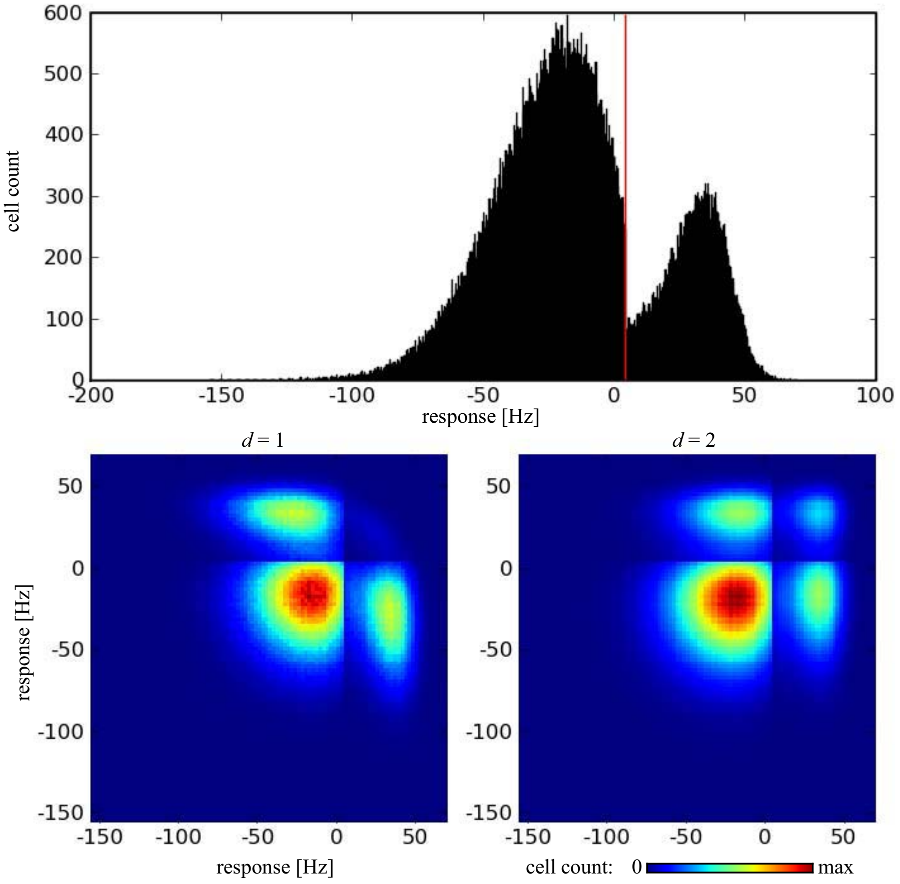

Figure 10. Bimodal output distribution. Same organisation as in Fig. 6; but parameters: $\mu(a) = 33.1\,\mathrm{Hz}, p = 16, \Lambda = -4$.

References

1. Hahnloser, R.H.R., Sarpeshkar, R., Mahowald, M.A., Douglas, R.J. & Seung, H.S. Digital selection and analogue amplification coexist in a cortex-inspired silicon circuit. *Nature* **405**, 947-951 (2000).
2. Seung, H.S., Richardson, T.J., Lagarias, J.C. & Hopfield, J.J. Minimax and Hamiltonian dynamics of excitatory-inhibitory networks. *Advances in neural information processing systems 10: proceedings of the 1997 conference* 329 (1998).
3. Slepian, D. On the Symmetrized Kronecker Power of a Matrix and Extensions of Mehler's Formula for Hermite Polynomials. *SIAM J. Math. Anal.* **3**, 606-616 (1972).
4. Kriener, B., Helias, M., Aertsen, A. & Rotter, S. Correlations in spiking neuronal networks with distance dependent connections. *Journal of Computational Neuroscience* **27**, 177-200 (2009).
5. Loewenstein, Y. u. a. Bistability of cerebellar Purkinje cells modulated by sensory stimulation. *Nat Neurosci* **8**, 202-211 (2005).
6. Anderson, J., Lampl, I., Reichova, I., Carandini, M. & Ferster, D. Stimulus dependence of two-state fluctuations of membrane potential in cat visual cortex. *Nat Neurosci* **3**, 617-621 (2000).
7. Cunningham, M.O. u. a. Neuronal metabolism governs cortical network response state. *Proc Natl Acad Sci U S A* **103**, 5597-5601 (2006).

Chapter 3

A note on olfactory bulb responses to mixtures with varying analyte ratio

A set of recent experiments has observed step-like transitions in the mitral cell population response to series of binary mixtures with gradually varying analyte ratio[1] ("morphing" series). These step-like transitions were inferred from an approximate block structure along the diagonal of the matrix of pairwise distances between response patterns to different ratios. Individual blocks correspond to ratio clusters or "categories" of odours. In this short note I demonstrate that sigmoidal ratio tuning of individual afferent channels[2] is sufficient for such a block structure to arise at the level of afferent patterns. This provides a simple possible mechanism of odour categorisation.

Introduction

The tuning of olfactory receptor neurones to different concentrations of a given odour is sigmoidal, relatively narrow and well described by the Hill equation when recorded electrically[2-4]. When measured by afferent imaging from glomerular modules dynamic ranges are larger, but saturation still occurs[5,6]. As data from high resolution calcium imaging argue against convergence of afferents with complementary sensitivity ranges in a given glomerulus[7], there is no obvious explanation for this difference.

Assuming "syntopic interaction" (no interaction beyond competition for receptors) of analytes which explained half the data in ref[2] this sigmoidal concentration tuning entails sigmoidal ratio tuning. I therefore examined the implications of sigmoidal single channel tuning for the population code. This was done in a minimal, mathematically tractable model and in a more naturalistic model with qualitatively the same results.

Results

In pioneering trials either model frequently generated correlation matrices with apparent block structure qualitatively similar to that observed experimentally. This remained true if Euclidean distance was used instead of Pearson correlation.

Blockiness index. To quantify this observation I introduced the following blockiness index B which detects block edges along the diagonal of the distance matrix D. For each grid point on the diagonal the longest two horizontal (or vertical) lines starting from this point were determined such that the pixels directly above (or left of) and directly below (or right of) the line could be separated by a threshold (Fig. 1). E.g. the n^{th} rightbound line would have length

$$l_{n,\mathrm{right}} = \max\left\{ m \middle| D_{n,n+i} \,{}^{\le}\!\!/\!{}_{\ge}\, D_{n+1,n+j} \forall i,j \in \{1,\ldots,m\} \right\} \tag{1}$$

where in the correlation and Euclidean metrics one would use the less-or-equal and greater-or-equal signs, respectively. The lengths of these "boundary lines" were then decreased by two grid units and all resulting positive numbers added and normalised by number of all boundary lines. Applied to measured data[1] the blockiness indices of an afferent arginine/histidine series were 0.25 or 0.3125 in the correlation and

Euclidean metrics, respectively, that for phenylalanine/tryptophan were 0.3125 or 0.25 in the correlation and Euclidean metrics, respectively.

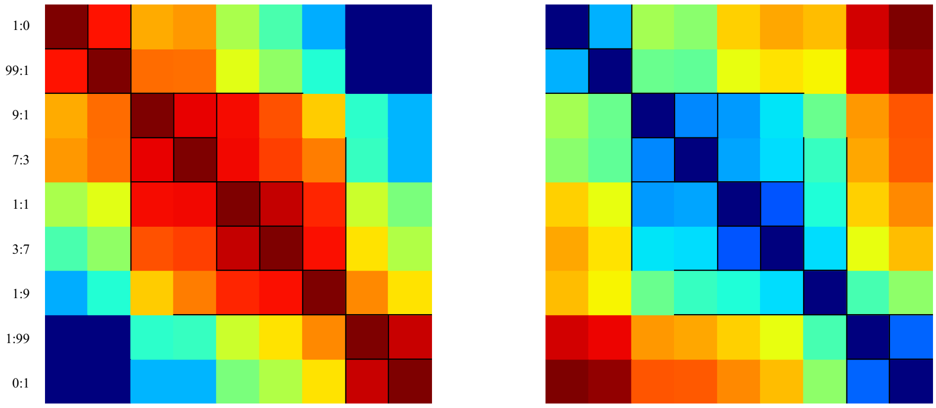

Figure 1. Blockiness of pooled arginine/histidine afferent response. Correlation (left) and Euclidean (right) metrics. Data by Jörn Niessing.

Note that in the Euclidean metric it is obvious that linear mixing leads to blockiness 0, because all binary mixtures lie on the line connecting the pure components.

It may be worthwhile to make this index more robust by relaxing the separation criterion with a tolerance parameter.

Minimal model. In the minimal model each glomerulus has a ratio x_g at which it switches from its response to one of the analytes to the response to the other.

$$F(x) = F_1 + \Theta(x - x_g)[F_2 - F_1] \tag{2}$$

Responses are assumed to be normally distributed; the switching points of different glomeruli are assumed to be equidistant along the ratio axis, such that in an evenly spaced ratio series the same number s of glomeruli will switch in each step.

In the Euclidean metric the expected blockiness index can be calculated, because the distribution of individual values in the distance matrix is quite simple. Because the blockiness index only depends on rank order instead of the Euclidean metric its square can be used. Then the *i,j*th matrix element is χ_k^2-distributed where *k* is the number of glomeruli switching between ratio *i* and ratio *j*.

Because starting from the diagonal distances monotonically increase in horizontal and vertical direction one can test whether a given boundary line has length > *l* by comparing the innermost off-diagomal element on the outward row to the *l*th off-diagonal element on the inward row. Using (A&S6.5.5, A&S6.5.21; ref[8]) and the fact that the two elements are independent the probability can thus be calculated

$$P_\Theta(l,s)=\int_0^\infty P\left(\frac{ls}{2},\frac{t}{2}\right)\chi_s^2(t)dt=\begin{cases}1-\sum_{k=0}^{\frac{ls}{2}-1}2^{-\frac{s}{2}-k}\binom{\frac{2}{s}+k-1}{k} & ls\text{ even}\\ \frac{1}{2}-\sum_{k=\frac{s}{2}}^{\frac{ls}{2}-1}2^{-\frac{s}{2}-k}\binom{\frac{2}{s}+k-1}{k} & ls\text{ odd}\end{cases}\tag{3}$$

if successive mixtures differ by precisely *s* glomeruli. Here *P* is the regularised gamma function and

$$\binom{x}{y}=\frac{\Gamma(x+1)}{\Gamma(y+1)\Gamma(x-y+1)}\tag{4}$$

is the binomial coefficient with non-integer arguments allowed for. (3) can be rephrased in terms of the Gaussian hypergeometric function ${}_2F_1$ (A&S15.1.1)

$$P_\Theta(l,s)=\sum_{k=\frac{ls}{2}}^{\infty}2^{-\frac{s}{2}-k}\binom{\frac{s}{2}+k-1}{k}=\frac{2^{-\frac{(l+1)s}{2}}\Gamma\left(\frac{(l+1)s}{2}\right)}{\Gamma\left(\frac{s}{2}\right)\Gamma\left(\frac{ls}{2}+1\right)}{}_2F_1\left(\frac{(l+1)s}{2},1;\frac{ls}{2}+1;\frac{1}{2}\right).\tag{5}$$

The expected Euclidean blockiness index of an *n*-step mixture series of patterns comprising *sn* glomeruli (Fig. 2) is

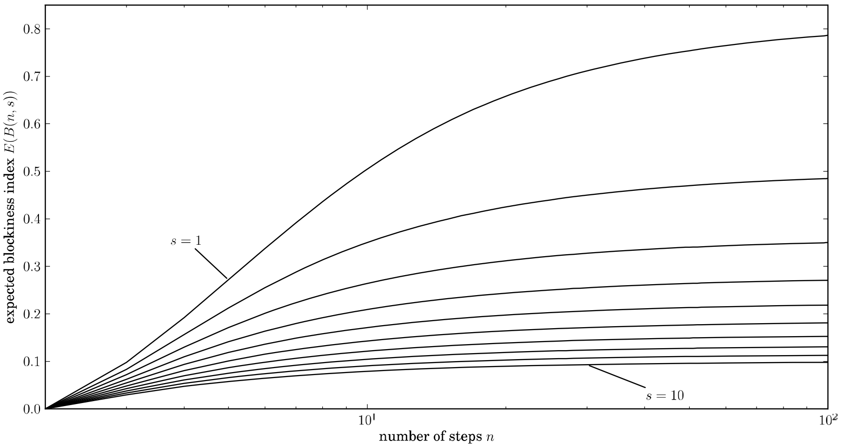

Figure 2. Expected blockiness index *E*(*B*(*n*,*s*)).

$$E(B(n,s)) = \sum_{l=2}^{n-1} \frac{n-l}{n} P_\Theta(l,s) \tag{6}$$

which tends to

$$B_s = \sum_{l=2}^{\infty} P_\Theta(l,s) = \begin{cases} \displaystyle\sum_{\mathrm{k=s}}^{\infty} \left\lfloor \frac{2k}{s} - 1 \right\rfloor 2^{-\frac{s}{2}-k} \binom{\frac{s}{2}+k-1}{k} & s \text{ even} \\ \displaystyle\sum_{\mathrm{k}=\frac{3}{2}\mathrm{s}}^{\infty} \left\lfloor \frac{k}{s} - \frac{1}{2} \right\rfloor 2^{-\frac{s}{2}-k} \binom{\frac{s}{2}+k-1}{k} + \sum_{\mathrm{k=s}}^{\infty} \left\lfloor \frac{k}{s} \right\rfloor 2^{-\frac{s}{2}-k} \binom{\frac{s}{2}+k-1}{k} & s \text{ odd} \end{cases} \tag{7}$$

when *n* is large. For *s* = 1,2 this simplifies to

$$\begin{aligned} B_1 &= \frac{1}{4\Gamma\left(\frac{1}{2}\right)} \sum_{k=0}^{\infty} \frac{\Gamma(2+k)\Gamma(2+k)}{\Gamma\left(\frac{5}{2}+k\right)} \frac{\left(\frac{1}{2}\right)^k}{k!} + \frac{1}{2^{\frac{3}{2}}\Gamma\left(\frac{1}{2}\right)} \sum_{k=0}^{\infty} \Gamma\left(\frac{3}{2}+k\right) \frac{\left(\frac{1}{2}\right)^k}{k!} \\ &= \frac{\Gamma(2)\Gamma(2)}{4\Gamma\left(\frac{1}{2}\right)\Gamma\left(\frac{5}{2}\right)} {}_2F_1\left(2,2;\frac{5}{2};\frac{1}{2}\right) + \frac{\Gamma\left(\frac{3}{2}\right)}{2^{\frac{3}{2}}\Gamma\left(\frac{1}{2}\right)} \left(\frac{1}{2}\right)^{-\frac{3}{2}} = \frac{1}{4\Gamma\left(\frac{3}{2}\right)^2} + \frac{1}{2} = \frac{1}{\pi} + \frac{1}{2} \end{aligned} \tag{8}$$

and

$$B_2 = \frac{1}{8}\sum_{k=0}^{\infty}\Gamma(2+k)\frac{\left(\frac{1}{2}\right)^k}{k!} = \frac{1}{2} \tag{9}$$

where I have used (A&S15.1.8, A&S15.1.24).

Higher B_s can be calculated similarly using

Fact 1. *Let*

$$f(x) = \sum_{i=0}^{\infty} f_i \frac{x^i}{i!} \qquad \textit{and} \qquad f^{[k]}(x) = \sum_{i=0}^{\infty}\left\lfloor \frac{i}{k} \right\rfloor f_i \frac{x^i}{i!} \tag{10}$$

converge absolutely where k is a positive integer. Then

$$f^{[k]}(x) = \frac{1}{k}x\frac{d}{dx}f(x) - \frac{1}{k^2}\sum_{j=0}^{k-1}\sum_{i=0}^{k-1} j\omega^{-ij} f\left(\omega^i x\right) \tag{11}$$

with ω a primitive k^{th} root of unity.

This can be applied to (7) in the form

$$B_s = \begin{cases} \dfrac{\Gamma(s)}{2^s\Gamma\left(\frac{s}{2}\right)\Gamma\left(\frac{s}{2}+1\right)}\,{}_2F_1^{\left[\frac{s}{2}\right]}\left(s,1;\frac{s}{2}+1;\frac{1}{2}\right) & s \text{ even} \\ \dfrac{\Gamma(s)}{2^s\Gamma\left(\frac{s}{2}\right)\Gamma\left(\frac{s}{2}+1\right)}\,{}_2F_1^{[s]}\left(s,1;\frac{s}{2}+1;\frac{1}{2}\right) + \dfrac{1}{2^{\frac{s}{2}}}\,{}_1F_0^{[s]}\left(\frac{s}{2};\frac{1}{2}\right) & s \text{ odd} \end{cases} \tag{12}$$

where

$${}_1F_0(a;z) = (1-z)^{-a}. \tag{13}$$

Syntopic model. The equations for syntopic interaction given in ref[2] which yield the response F of a single channel to a mixture $\sum c_o o$ can be rewritten

$$F\left(\sum c_o o\right) = \frac{\sum\left(\frac{c_o}{K_o}\right)^n F_{\max,o}}{1+\sum\left(\frac{c_o}{K_o}\right)^n} \tag{14}$$

with c_o, K_o, $F_{\max,o}$ the concentration, half saturation concentration and maximum response for analyte o, respectively and all sums running over analytes $\{o\}$ which are considered to span a vector space of mixtures.

Binary mixtures with the same total concentration $c_{\text{tot}} = c_1 + c_2$ are conveniently parametrised in terms of

$$\begin{aligned} c_1(x) &= c_{\text{tot}} \frac{e^x}{e^x + e^{-x}} = c_{\text{tot}} \frac{1+\tanh x}{2} \\ c_2(x) &= c_{\text{tot}} \frac{e^{-x}}{e^x + e^{-x}} = c_{\text{tot}} \frac{1-\tanh x}{2} \\ F(x) &= \frac{\frac{c_1(x)^n}{K_1^n} F_{\max,1} + \frac{c_2(x)^n}{K_2^n} F_{\max,2}}{1 + \frac{c_1(x)^n}{K_1^n} + \frac{c_2(x)^n}{K_2^n}} \end{aligned} \tag{15}$$

The distributions of parameters entering into these equations have not been reported in zebrafish. I therefore used data from rat[2] and systematically scaled the distribution of Hill coefficients and the total concentration c_{tot} . The number of glomeruli and the values of $F_{\max}$ were chosen such that the pure analytes at concentration c_{tot} reproduced response patterns to phenylalanine and tryptophan in zebrafish[9]. The blockiness index was then averaged over 2,000 realisations of the ratio series used in ref[1] (Fig. 3). The average blockiness index strongly varied and reached high values for some parameter combinations.

In summary, both a minimal mathematically tractable and a more realistic model based on measured single channel afferent characteristics predict that sigmoidal ratio tuning can translate into ratio clustering at population level.

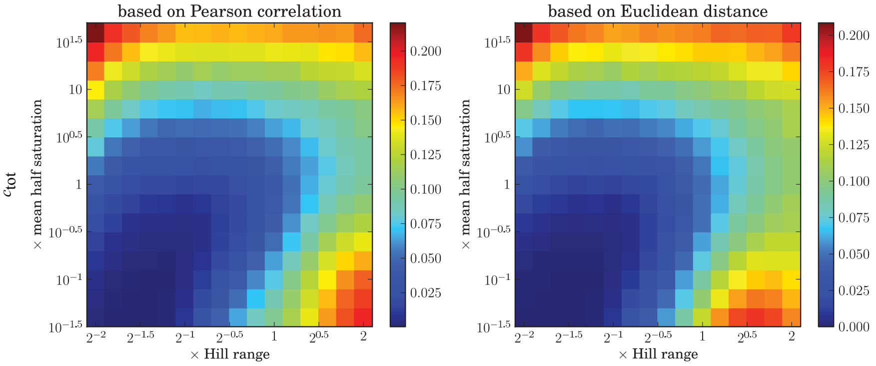

Figure 3. Average blockiness index of phenylalanine/tryptophan series using Rospars' model.

Discussion

I have demonstrated that ratio clusters emerge naturally from minimal assumptions. My treatment formalises the following intuitive argument: Glomeruli for which response amplitudes between the two analytes differ strongly are rare. Because these glomeruli contribute strongly to pattern differences their switching ratios delineate ratio clusters.

It is also intuitive that the phenomenon is diluted if the number of glomeruli becomes large, because in a given ratio series many glomeruli will switch in each step (parameter s in the minimal model), levelling the distribution of per step distances.

References

1. Niessing, J. & Friedrich, R.W. Olfactory pattern classification by discrete neuronal network states. *Nature* **465**, 47-52 (2010).
2. Rospars, J., Lansky, P., Chaput, M. & Duchamp-Viret, P. Competitive and Noncompetitive Odorant Interactions in the Early Neural Coding of Odorant Mixtures. *J. Neurosci.* **28**, 2659-2666 (2008).
3. Firestein, S., Picco, C. & Menini, A. The relation between stimulus and response in olfactory receptor cells of the tiger salamander. *J. Physiol. (Lond.)* **468**, 1-10 (1993).
4. Ito, I., Bazhenov, M., Ong, R.C., Raman, B. & Stopfer, M. Frequency Transitions in Odor-Evoked Neural Oscillations. *Neuron* **64**, 692-706 (2009).
5. Meister, M. & Bonhoeffer, T. Tuning and Topography in an Odor Map on the Rat Olfactory Bulb. *J. Neurosci.* **21**, 1351-1360 (2001).
6. Wachowiak, M. & Cohen, L.B. Representation of Odorants by Receptor Neuron Input to the Mouse Olfactory Bulb. *Neuron* **32**, 723-735 (2001).
7. Wachowiak, M., Denk, W. & Friedrich, R.W. Functional organization of sensory input to the olfactory bulb glomerulus analyzed by two-photon calcium imaging. *Proceedings of the National Academy of Sciences of the United States of America* **101**, 9097 -9102 (2004).

8. Abramowitz, M. & Stegun, I.A. *Handbook of mathematical functions with formulas, graphs, and mathematical tables*. (Dover publications: 1964).
9. Friedrich, R.W. & Korsching, S.I. Combinatorial and Chemotopic Odorant Coding in the Zebrafish Olfactory Bulb Visualized by Optical Imaging. *Neuron* **18**, 737-752 (1997).

Acknowledgements

The author would like to thank friends and family for continued support, members of the Friedrich group for stimulating discussions, sharing data and creating a pleasant atmosphere, Botond Roska for reviewing this thesis and last not least Rainer Friedrich for the patience and trust to see a project through that at times was teetering on the brink of failure.

Appendix A1

Theory supplementing chapter 1

Prerequisites

For convenience and to unify notation we collate a couple of well-known facts about the univariate η-rectified standard normal distribution ${}_{\eta}\Phi$ with density

$$\text{(M1)} \quad {}_{\eta}\varphi(x) = \Theta(x)\varphi(x+\eta) + \delta(x)\int_{-\infty}^{0} \varphi(s+\eta)ds$$

which results from applying a threshold η to the standard normal distribution Φ with density $\varphi(x) = \frac{1}{\sqrt{2\pi}} e^{-\frac{x^2}{2}}$. Θ and δ refer to the Heaviside step function and the Dirac delta distribution, respectively. The premoments of ${}_{\eta}\Phi$ elsewhere called "repeated integrals of the normal probability integral" (Ref 1: 26.2.41-45, beware of misprints in 26.2.43, 45) are given by

$$\text{(M2)} \quad {}_{\eta}M_m = \begin{cases} H_{-m-1}(\eta)\varphi(\eta) & m < 0 \\ \int_0^{\infty} \frac{s^m}{m!}\varphi(s+\eta)ds & m \geq 0 \end{cases}$$

with $H_m(\eta) = (-1)^m \dfrac{\dfrac{d^m}{d\eta^m}\varphi(\eta)}{\varphi(\eta)}$ the *m*-th Hermite polynomial (Ref 1: 22.3.11, 26.2.31). If *m* is positive $m!\,{}_\eta M_m$ equals the *m*-th raw moment of ${}_\eta\Phi$. The ${}_\eta M_m$ satisfy (M3) $\dfrac{d}{d\eta}\,{}_\eta M_m = -{}_\eta M_{m-1}$

(M4) $${}_\eta M_{m-1} = (m+1)\,{}_\eta M_{m+1} + \eta\,{}_\eta M_m$$

and by Ref 1: 7.1.13:

(M5) $$\begin{array}{ll} \eta\,{}_\eta M_0 < {}_\eta M_{-1} < \left(\eta + \dfrac{1}{\eta}\right){}_\eta M_0 & \eta > 0 \\ \eta\left({}_\eta M_0 - 1\right) < {}_\eta M_{-1} < \left(\eta + \dfrac{1}{\eta}\right)\left({}_\eta M_0 - 1\right) & \eta < 0 \end{array}$$

(M6) $${}_\eta M_1 > -\eta$$

We will now formulate a bivariate version of the above. Applying thresholds η, κ to the ρ-correlated standard binormal distribution Φ_ρ with density

(M7) $$\varphi_\rho(x,y) = \begin{cases} \dfrac{1}{2\pi\sqrt{1-\rho^2}}\, e^{-\frac{x^2+y^2-2\rho xy}{2(1-\rho^2)}} & -1 < \rho < 1 \\ \delta(x \mp y)\varphi(x) & \rho = \pm 1 \end{cases}$$

gives rise to the η, κ-rectified ρ-correlated standard binormal distribution ${}_{\eta,\kappa}\Phi_\rho$ with density

(M8)
$$\begin{aligned} {}_{\eta,\kappa}\varphi_\rho(x,y) &= \Theta(x)\Theta(y)\varphi_\rho(x+\eta,y+\kappa) \\ &+ \Theta(x)\delta(y)\int_{-\infty}^{0}\varphi_\rho(x+\eta,t+\kappa)dt \\ &+ \delta(x)\Theta(y)\int_{-\infty}^{0}\varphi_\rho(s+\eta,y+\kappa)ds \\ &+ \delta(x)\delta(y)\int_{-\infty}^{0}\int_{-\infty}^{0}\varphi_\rho(s+\eta,t+\kappa)dsdt \end{aligned}$$

The bivariate Hermite polynomials and the premoments of ${}_{\eta,\kappa}\Phi_\rho$ are

(M9)
$$ {}^{\rho}H_{m,n}(\eta,\kappa) = (-1)^{m+n}\frac{\dfrac{\partial^{m+n}}{\partial\eta^m\partial\kappa^n}\varphi_\rho(\eta,\kappa)}{\varphi_\rho(\eta,\kappa)} \qquad m,n\ge 0;\rho\ne\pm 1$$

(M10)
$$ {}_{\eta,\kappa}M_{m,n}(\rho) = \begin{cases} {}^{\rho}H_{-m-1,-n-1}(\eta,\kappa)\varphi_\rho(\eta,\kappa) & m,n<0;\rho\ne\pm 1 \\ \displaystyle\int_0^\infty\int_0^\infty \frac{s^m t^n}{m!n!}\varphi_\rho(s+\eta,t+\kappa)dsdt & m,n\ge 0 \end{cases}$$

Definition (M10) extends to arbitrary integer *m,n* by (M11, M12) below. If *m*,*n* are positive $m!n!\,{}_{\eta,\kappa}M_{m,n}(\rho)$ equals the *m,n*-th raw moment of ${}_{\eta,\kappa}\Phi_\rho$. Elementary calculations (cf. Ref. 2) yield

(M11)
$$ {}_{\eta,\kappa}M_{m,n}(\rho) = {}_{\kappa,\eta}M_{n,m}(\rho)$$

(M12)
$$ \frac{\partial}{\partial\eta}\,{}_{\eta,\kappa}M_{m,n}(\rho) = -\,{}_{\eta,\kappa}M_{m-1,n}(\rho)$$

(M13)
$$ \frac{\partial}{\partial\rho}\,{}_{\eta,\kappa}M_{m,n}(\rho) = {}_{\eta,\kappa}M_{m-1,n-1}(\rho)$$

(M14)
$$ {}_{\eta,\kappa}M_{m-1,n}(\rho) + \rho\,{}_{\eta,\kappa}M_{m,n-1}(\rho) = (m+1)\,{}_{\eta,\kappa}M_{m+1,n}(\rho) + \eta\,{}_{\eta,\kappa}M_{m,n}(\rho)$$

(M15)
$$\begin{aligned} &(1-\rho^2)\,{}_{\eta,\kappa}M_{m-1,n}(\rho) + \rho(n+1)\,{}_{\eta,\kappa}M_{m,n+1}(\rho) \\ &= (m+1)\,{}_{\eta,\kappa}M_{m+1,n}(\rho) + (\eta-\rho\kappa)\,{}_{\eta,\kappa}M_{m,n}(\rho) \end{aligned}$$

(M16) ${}_{\eta,\kappa}M_{m,n}(0) = {}_{\eta}M_{m}\;{}_{\kappa}M_{n}$

(M17) $m!n!\;{}_{\eta,\eta}M_{m,n}(1) = (m+n)!\;{}_{\eta}M_{m+n} \quad m,n \geq 0$

(M13) follows from Price's theorem. From (M13) and (M16) Mehler's formula (Ref 1: 26.3.29)

(M18) ${}_{\eta,\kappa}M_{m,n}(\rho) = \sum_{0}^{\infty} {}_{\eta}M_{m-i}\;{}_{\kappa}M_{n-i}\,\frac{\rho^{i}}{i!}$

can be recovered. We will abbreviate

(M19) ${}_{\eta,\kappa}\overline{M}_{m,n}(\rho) = {}_{\eta,\kappa}M_{m,n}(\rho) - {}_{\eta,\kappa}M_{m,n}(0)$

Remark M1: From definition (M10) and the easily verified expression ${}_{\eta,\kappa}M_{-1,n}(\rho) = \varphi(\eta)\sqrt{1-\rho^{2}}^{\,n}\;{}_{\frac{\kappa-\rho\eta}{\sqrt{1-\rho^{2}}}}M_{n}$ we derive the simple but very useful fact

(M20) ${}_{\eta,\kappa}M_{m,n}(\rho) > 0 \quad m,n \geq -1; \rho \neq \pm 1$

Via (M12, M13) this implies for nonnegative *m,n* that ${}_{\eta,\kappa}M_{m,n}(\rho)$ strictly increases in ρ and strictly decreases in η,κ. Similarly, ${}_{\eta,\kappa}M_{m,n}(\rho)$ is strictly convex in ρ and strictly concave in η,κ if *m,n* are positive, and so forth. One consequence is that the covariance ${}_{\eta,\eta}\overline{M}_{1,1}(\rho)$ of the thresholded binormal has the same sign as ρ. We will freely use these and similar facts.

Proof of TIDe theorem

Proof of theorem 1: Assertion 1 is essentially contained in remark M1. To prove assertion 3 choose $\varepsilon > 0$ and N_ε such that $|\rho|^{N_\varepsilon} < \varepsilon$. By the Mehler formula (M18) we have ${}_\eta r(\rho) = \dfrac{{}_\eta M_0^2 \rho + \varphi^2(\eta)\sum_0^\infty H_i^2(\eta)\dfrac{\rho^{i+2}}{(i+2)!}}{{}_\eta M_0^2 + \varphi^2(\eta)\sum_0^\infty H_i^2(\eta)\dfrac{1}{(i+2)!}}$. It will clearly suffice to show

$$\frac{{}_\eta M_0^2 \rho + \varphi^2(\eta)\sum_0^{N_\varepsilon} H_i^2(\eta)\dfrac{\rho^{i+2}}{(i+2)!}}{{}_\eta M_0^2 + \varphi^2(\eta)\sum_0^{N_\varepsilon} H_i^2(\eta)\dfrac{1}{(i+2)!}} \to \rho^{N_\varepsilon+2} \tag{M21}$$

for large η. By (M5) we have $0 < {}_\eta M_0 < \varphi(\eta)$ if $\eta \ge 1$. Since the H_i are polynomials of degree *i* with leading coefficient 1 the numerator of the l.h.s. of (M21) is easily seen to tend to $\varphi^2(\eta)\eta^{2N_\varepsilon}\dfrac{\rho^{N_\varepsilon+2}}{(N_\varepsilon+2)!}$ for large η. Similarly, the denominator tends to $\varphi^2(\eta)\eta^{2N_\varepsilon}\dfrac{1}{(N_\varepsilon+2)!}$ which proves (M21) and assertion 3.

Assertion 2 follows from the following two lemmata.

Lemma M2: Let $a \le b < c$ be real numbers and Ω a nonempty connected open subset of the real numbers. Let the function $g(\xi,\alpha)$ be defined on the set $\Omega \times [a,c]$. Let *g* be differentiable in ξ and strictly increasing in α. Let $g^{-1}(\xi,\beta)$ be the inverse of *g* with respect to the second argument. Assume that the composite function $u(\xi,\beta) = \left[\dfrac{\partial}{\partial\xi} g\right]\left(\xi, g^{-1}(\xi,\beta)\right)$ is strictly convex (or strictly concave) in β. Then the function $q(\xi,\alpha) = \dfrac{g(\xi,\alpha) - g(\xi,b)}{g(\xi,c) - g(\xi,b)}$ is

1. strictly decreasing (or strictly increasing) in ξ if $\alpha > b$
2. strictly increasing (or strictly decreasing) in ξ if $\alpha < b$

Proof: Abbreviating $\chi_\alpha = g(\xi,\alpha)$ we can write

$$\text{(M22)}\quad \frac{\partial}{\partial\xi} q(\xi,\alpha) = q(\xi,\alpha)\left[\frac{u(\xi,\chi_\alpha)-u(\xi,\chi_b)}{\chi_\alpha-\chi_b} - \frac{u(\xi,\chi_c)-u(\xi,\chi_b)}{\chi_c-\chi_b}\right].$$

If $\alpha > b$ we have $\chi_\alpha > \chi_b$ and thus by definition of convexity

$$\text{(M23)}\quad u(\xi,\chi_\alpha) < \frac{\chi_c-\chi_\alpha}{\chi_c-\chi_b} u(\xi,\chi_b) + \frac{\chi_\alpha-\chi_b}{\chi_c-\chi_b} u(\xi,\chi_c)$$

such that (M22) must be negative. The other cases are proven similarly.

Lemma M3: For any η the composite function $u_0(\chi) = -2\ {}_{\eta,\eta}M_{1,0}\left({}_{\eta,\eta}M_{1,1}^{-1}(\chi)\right)$ is strictly convex.

Proof: A direct computation setting $\rho = {}_{\eta,\eta}M_{1,1}^{-1}(\chi)$ and using (M13, M14) yields

$$\begin{aligned}
\frac{d^2}{d\chi^2} u_0(\chi) &= \frac{-2\ {}_{\eta,\eta}M_{-1,-1}(\rho)}{{}_{\eta,\eta}M_{0,0}^2(\rho)}\left[\frac{{}_{\eta,\eta}M_{-1,-2}(\rho)}{{}_{\eta,\eta}M_{-1,-1}(\rho)} - \frac{{}_{\eta,\eta}M_{0,-1}(\rho)}{{}_{\eta,\eta}M_{0,0}(\rho)}\right] \\
\text{(M24)}\qquad &= \frac{-2\ {}_{\eta,\eta}M_{-1,-1}(\rho)}{{}_{\eta,\eta}M_{0,0}^2(\rho)}\left[\frac{\eta}{1+\rho} - \frac{{}_{\eta,\eta}M_{1,0}(\rho) + \eta\ {}_{\eta,\eta}M_{0,0}(\rho)}{(1+\rho)\ {}_{\eta,\eta}M_{0,0}(\rho)}\right] \\
&= \frac{2\ {}_{\eta,\eta}M_{-1,-1}(\rho)\ {}_{\eta,\eta}M_{1,0}(\rho)}{(1+\rho)\ {}_{\eta,\eta}M_{0,0}^3(\rho)}
\end{aligned}$$

which is clearly positive.

Remark M4: As a consequence of $\rho = \lim_{\eta\to-\infty} {}_\eta r(\rho)$ and assertion 2 we have $\rho > {}_\eta r(\rho)$ for $0 < \rho < 1$, i.e. TIDe. From assertion 1b) one derives the lower bound

${}_{\eta}r(1-\varepsilon) > 1 - \frac{{}_{\eta,\eta}M_{0,0}(1)}{{}_{\eta,\eta}\overline{M}_{1,1}(1)} \cdot \varepsilon$ which limits the amount by which near-identical stimuli are decorrelated and thus guarantees noise-tolerance.

Remark M5: Violation of either the assumption of equal thresholds for both variates or the assumption of binormality permits counterexamples to theorem 1 (Supplementary Fig. 1a-c).

Recurrent circuit

Let us abbreviate

(M25) $\eta_v = \frac{\eta_0 - \mu(v)}{\sigma(v)}$

(M26) $f(\eta, \rho, P) = \rho - P\ {}_{\eta,\eta}\overline{M}_{1,1}(\rho)$

(M27) $f_1(\eta, \eta_a, P) = -\eta - \Lambda\ {}_{\eta}M_1 + \eta_a \sqrt{f(\eta, 1, P)}$

(M28) $Q(\eta, \rho, P) = \frac{f(\eta, \rho, P)}{f(\eta, 1, P)}$

(M29) $f_2(\eta, \rho, P) = \rho_a - Q(\eta, \rho, P)$

where $\sigma(v)$ stands for the standard deviation of a variate *v*. With these substitutions and under assumptions of binormality equations (3-5) become

(M30) $f_1(\eta_x, \eta_a, P) = 0$

(M31) $f_2(\eta_x, \rho_x, P) = 0$

Recall that *P* cannot be negative because it stands for $p\lambda^2$.

Remark M6: Strictly speaking the phrasing of theorems 2 and 3 is nonsensical because the premise of binormality of input and feedback can only be approximately satisfied. What is actually meant is, of course, that these theorems refer to the idealised system (M30, M31).

Proof of theorem 2: $\rho_x \geq \rho_a$ would by (M31) and theorem 1 imply

$$\text{(M32)}\quad \rho_a \leq \rho_x < \frac{\rho_x - P\ {}_{\eta_x} r(\rho_x)\ {}_{\eta_x,\eta_x}\overline{M}_{1,1}(1)}{f(\eta_x,1,P)} = \frac{\rho_x - P\ {}_{\eta_x,\eta_x}\overline{M}_{1,1}(\rho_x)}{f(\eta_x,1,P)} = \rho_a$$

which is a contradiction.

Uniqueness of solutions

Definition M7: The system (M30, M31) or its parameters are called gain-limited if $\Lambda \leq 1$. A solution η_x to (M30) is called variance-limited if

$$\text{(M33)}\quad P\ {}_{\eta_x}M_0 < 1;$$

the system or its parameters are called variance-limited if they permit a variance-limited solution.

Note that variance-limitedness is slightly stronger than the constraint

$$\text{(M34)}\quad f(\eta_x,1,P) > 0$$

implicit in (M30, M31). We will see below that gain- and in particular variance-limitedness are good predictors of convergence of the system (1).

Theorem M8: Let (M30, M31) be gain- and variance-limited. Then

1. variance-limited solutions η_x are unique.
2. for any $-1 \leq \rho_a \leq 1$ there is a unique solution ρ_x to (M31) extending the variance-limited solution η_x.

Proof: To prove assertion 1 we will demonstrate that to the right of a solution f_1 decreases in η_x. Observe that $0 \geq f_1(\eta_x, \eta_a, P)$ implies

$$\text{(M35)}\quad \frac{\partial}{\partial \eta_x} f_1(\eta_x, \eta_a, P) \leq -1 + \Lambda\, {}_{\eta_x}M_0 + \left(\eta_x + \Lambda\, {}_{\eta_x}M_1\right) \frac{\frac{\partial}{\partial \eta_x} f(\eta_x, 1, P)}{2 f(\eta_x, 1, P)}$$

with equality if η_x is actually a solution. By (M4, M17) we have

$$\text{(M36)}\quad \begin{aligned} &\left(-1 + \Lambda\, {}_{\eta_x}M_0\right) f(\eta_x, 1, P) + \left(\eta_x + \Lambda\, {}_{\eta_x}M_1\right) P\, {}_{\eta_x,\eta_x}\overline{M}_{1,0}(1) \\ &= \left(-1 + \Lambda\, {}_{\eta_x}M_0\right)\left(1 - P\, {}_{\eta_x}M_0 + P\, {}_{\eta_x}M_1\left[\eta_x + {}_{\eta_x}M_1\right]\right) \\ &\quad + \left(\eta_x + \Lambda\, {}_{\eta_x}M_1\right) P\, {}_{\eta_x}M_1\left(1 - {}_{\eta_x}M_0\right) \\ &= \left(-1 + \Lambda\, {}_{\eta_x}M_0\right)\left(1 - P\, {}_{\eta_x}M_0\right) + P\, {}_{\eta_x}M_1\left(\eta_x\, {}_{\eta_x}M_0 + {}_{\eta_x}M_1\right)(-1 + \Lambda) \\ &= \left(-1 + \Lambda\, {}_{\eta_x}M_0\right)\left(1 - P\, {}_{\eta_x}M_0\right) + P\, {}_{\eta_x}M_1\, {}_{\eta_x}M_{-1}(-1 + \Lambda) \end{aligned}$$

Together (M34-M36) imply

$$\text{(M37)}\quad \frac{\partial}{\partial \eta_x} f_1(\eta_x, \eta_a, P) < 0.$$

Assertion 2: By (M33)

$$\text{(M38)}\quad \frac{\partial}{\partial \rho_x} f_2(\eta_x,\rho_x,P) = -\frac{\partial}{\partial \rho_x} Q(\eta_x,\rho_x,P) = -\frac{1-P_{\eta_x,\eta_x} M_{0,0}(\rho_x)}{f(\eta_x,1,P)} < 0$$

which implies uniqueness. Since Q is concave in ρ_x and $Q(\eta_x,0,P)=0$ and $Q(\eta_x,1,P)=1$ we have $Q(\eta_x,-1,P)\leq -1$. Existence now follows from the intermediate value theorem.

Remark M9: If the requirement of variance-limitedness is omitted from theorem 7 uniqueness can be lost (Supplementary Fig. 1d).

Proof of theorem 3

Definition M10: The system (M30, M31) is called sufficiently coupled if

$$\text{(M39)}\quad \eta_x + P_{\eta_x,\eta_x} M_{1,0}(0) \geq 0$$

holds for a variance-limited solution.

Lemma M11: Under the assumptions of theorem 3, $Q(\eta_x,\rho_x,P)$

1. strictly increases in *P*,
2. strictly decreases in η_x if (M30, M31) is sufficiently coupled and
3. strictly increases along

$$\text{(M40)}\quad v_1 = e_P - \frac{\frac{\partial}{\partial P} f_1(\eta_x,\eta_a,P)}{\frac{\partial}{\partial \eta_x} f_1(\eta_x,\eta_a,P)} e_{\eta_x}$$

where e_P, e_{η_x} are unit vectors defined by P, η_x.

Proof: Write ${}_{\eta_x}F_P(\vartheta) = \vartheta - P\ {}_{\eta_x,\eta_x}M_{11}(\vartheta)$. By remark M1, (M17) and variance-limitedness

$$\text{(M41)} \quad \frac{\partial}{\partial \vartheta}\ {}_{\eta_x}F_P(\vartheta) = 1 - P\ {}_{\eta_x,\eta_x}M_{0,0}(\vartheta) > 0$$

such that lemma M2 can be used. We will abbreviate $\chi = {}_{\eta_x}F_P(\vartheta)$.

Assertion 1: It must be shown that $u_1(\chi) = \left[\frac{\partial}{\partial P}\ {}_{\eta_x}F_P\right]\left({}_{\eta_x}F_P^{-1}(\chi)\right)$ is strictly concave on the interval $\left[0, {}_{\eta}F(1)\right]$. Directly calculating the curvature yields

$$\text{(M42)} \quad \begin{aligned} &\frac{d^2}{d\chi^2}u_1(\chi) \\ &= \frac{P\ {}_{\eta_x,\eta_x}M_{-1,-1}(\vartheta)}{\left(1 - P\ {}_{\eta_x,\eta_x}M_{0,0}(\vartheta)\right)^2}\left[\frac{-{}_{\eta_x,\eta_x}M_{0,0}(\vartheta)}{1 - P\ {}_{\eta_x,\eta_x}M_{0,0}(\vartheta)} + \frac{-{}_{\eta_x,\eta_x}M_{-1,-1}(\vartheta)}{P\ {}_{\eta_x,\eta_x}M_{-1,-1}(\vartheta)}\right] \\ &= \frac{P\ {}_{\eta_x,\eta_x}M_{-1,-1}(\vartheta)}{\left(1 - P\ {}_{\eta_x,\eta_x}M_{0,0}(\vartheta)\right)^3} \cdot \left(-\frac{1}{P}\right) \end{aligned}$$

which is indeed negative.

Assertion 2: Assuming sufficient coupling, it must be shown that $u_2(\chi) = \left[\frac{\partial}{\partial \eta_x}\ {}_{\eta_x}F_P\right]\left({}_{\eta_x}F_P^{-1}(\chi)\right)$ is strictly convex on the interval $\left[0, {}_{\eta}F(1)\right]$. Directly calculating the curvature yields

$$
\begin{aligned}
&\frac{d^2}{d\chi^2}u_2(\chi)\\
&=\frac{P\,{}_{\eta_x,\eta_x}M_{-1,-1}(\vartheta)}{\left(1-P\,{}_{\eta_x,\eta_x}M_{0,0}(\vartheta)\right)^2}\left[\frac{2P\,{}_{\eta_x,\eta_x}M_{0,-1}(\vartheta)}{1-P\,{}_{\eta_x,\eta_x}M_{0,0}(\vartheta)}+\frac{2\,{}_{\eta_x,\eta_x}M_{-1,-2}(\vartheta)}{{}_{\eta_x,\eta_x}M_{-1,-1}(\vartheta)}\right]\\
\text{(M43)}\quad&=\frac{P\,{}_{\eta_x,\eta_x}M_{-1,-1}(\vartheta)}{\left(1-P\,{}_{\eta_x,\eta_x}M_{0,0}(\vartheta)\right)^2}\left[\frac{2P\left[\eta_x\,{}_{\eta_x,\eta_x}M_{0,0}(\vartheta)+{}_{\eta_x,\eta_x}M_{1,0}(\vartheta)\right]}{(1+\vartheta)\left[1-P\,{}_{\eta_x,\eta_x}M_{0,0}(\vartheta)\right]}+\frac{2\eta_x}{1+\vartheta}\right]\\
&=\frac{P\,{}_{\eta_x,\eta_x}M_{-1,-1}(\vartheta)}{\left(1-P\,{}_{\eta_x,\eta_x}M_{0,0}(\vartheta)\right)^3}\cdot\frac{2\left[\eta_x+P\,{}_{\eta_x,\eta_x}M_{1,0}(\vartheta)\right]}{1+\vartheta}
\end{aligned}
$$

which has the same sign as $\eta_x + P\,{}_{\eta_x,\eta_x}M_{1,0}(\vartheta)$.

Assertion 3: We distinguish two cases.

Case 1: $\eta_a \geq 0$. Lemma M2 can be used as above. It must be shown that $u_3(\chi)=\left[D_{v_1}\,{}_{\eta_x}F_P\right]\left({}_{\eta_x}F_P^{-1}(\chi)\right)$ is strictly concave on the interval $\left[0,\ {}_{\eta}F(1)\right]$. Here D_{v_1} indicates the directional derivative along the vector v_1. Combining (M42, M43) yields the curvature

$$
\text{(M44)}\quad
\begin{aligned}
&\frac{d^2}{d\chi^2}u_3(\chi)=\frac{P\,{}_{\eta_x,\eta_x}M_{-1,-1}(\vartheta)}{\left(1-P\,{}_{\eta_x,\eta_x}M_{0,0}(\vartheta)\right)^3}\\
&\cdot\left[-\frac{1}{P}-\frac{\frac{\partial}{\partial P}f_1(\eta_x,\eta_a,P)}{\frac{\partial}{\partial \eta_x}f_1(\eta_x,\eta_a,P)}\cdot\frac{2\left[\eta_x+P\,{}_{\eta_x,\eta_x}M_{1,0}(\vartheta)\right]}{(1+\vartheta)}\right]
\end{aligned}
$$

Because η_a is nonnegative $\frac{\partial}{\partial P}f_1(\eta_x,\eta_a,P)$ is non-positive and $\eta_x+\Lambda\,{}_{\eta_x}M_1$ is nonnegative such that by (M35-M37)

$$
\begin{aligned}
0 &\leq \frac{\frac{\partial}{\partial P} f_1(\eta_x, \eta_a, P)}{\frac{\partial}{\partial \eta_x} f_1(\eta_x, \eta_a, P)} \\
&= \frac{-\frac{1}{2}\left(\eta_x + \Lambda\ {}_{\eta_x}M_1\right)\ {}_{\eta_x,\eta_x}\overline{M}_{1,1}(1)}{\left(-1+\Lambda\ {}_{\eta_x}M_0\right)\left(1-P\ {}_{\eta_x}M_0\right)+P\ {}_{\eta_x}M_1\ {}_{\eta_x}M_{-1}(-1+\Lambda)} \qquad \text{(M45)} \\
&\leq \frac{\frac{1}{2}\left(\eta_x + \Lambda\ {}_{\eta_x}M_1\right)\ {}_{\eta_x,\eta_x}\overline{M}_{1,1}(1)}{\left(1-\Lambda\ {}_{\eta_x}M_0\right)\left(1-P\ {}_{\eta_x}M_0\right)}
\end{aligned}
$$

It is now obvious that (M44) is negative if (M30, M31) is sufficiently coupled. We therefore assume otherwise, in particular $\eta_x < 0$. Then by (M4, M5)

$$
\begin{aligned}
0 &\leq \frac{\eta_x + \Lambda\ {}_{\eta_x}M_1}{1-\Lambda\ {}_{\eta_x}M_0} = \frac{\eta_x\left(1-\Lambda\ {}_{\eta_x}M_0\right)+\Lambda\ {}_{\eta_x}M_{-1}}{1-\Lambda\ {}_{\eta_x}M_0} \qquad \text{(M46)} \\
&< \eta_x + \frac{\Lambda\left({}_{\eta_x}M_0 - 1\right)}{1-\Lambda\ {}_{\eta_x}M_0}\left(\eta_x + \frac{1}{\eta_x}\right) < -\frac{1}{\eta_x}
\end{aligned}
$$

and, similarly, using remark M1 and (M17, M6)

$$
\text{(M47)} \quad 0 > \frac{\eta_x + P\ {}_{\eta_x,\eta_x}M_{1,0}(\vartheta)}{1-P\ {}_{\eta_x}M_0} > \eta_x + \frac{P\ {}_{\eta_x}M_0\left(\eta_x + {}_{\eta_x}M_1\right)}{1-P\ {}_{\eta_x}M_0} > \eta_x
$$

Finally, by the mean value theorem, remark M1 and (M17)

$$
\text{(M48)} \quad 0 < {}_{\eta_x,\eta_x}\overline{M}_{1,1}(1) < {}_{\eta_x,\eta_x}M_{0,0}(1) < \frac{1}{P}
$$

Together (M45-M48) prove that (M44) is negative.

Case II: $\eta_a < 0$. Write

$$\text{(M49)}\quad v = e_P - \frac{\frac{\partial}{\partial P} f(\eta_x,1,P)}{\frac{\partial}{\partial \eta_x} f(\eta_x,1,P)} e_{\eta_x}$$

and

$$\text{(M50)}\quad F = \frac{\frac{\partial}{\partial P} f_1(\eta_x,\eta_a,P)\frac{\partial}{\partial \eta_x} f(\eta_x,1,P)}{\frac{\partial}{\partial \eta_x} f_1(\eta_x,\eta_a,P)\frac{\partial}{\partial P} f(\eta_x,1,P)} = \frac{1}{1 - \frac{2\sqrt{f(\eta_x,1,P)}\left(1-\Lambda\,{}_{\eta_x}M_0\right)}{\eta_a \frac{\partial}{\partial \eta_x} f(\eta_x,1,P)}}$$

Using the rightmost expression in (M50) it is obvious that

$$\text{(M51)}\quad 0 < F < 1$$

such that

$$\text{(M52)}\quad v_1 = (1-F)e_P + Fv$$

is a convex combination. Finally, a direct computation yields

$$\text{(M53)}\quad \begin{aligned} &D_v Q(\eta_x,\rho_x,P) \\ &= \frac{\frac{\partial}{\partial \eta_x} f(\eta_x,\rho_x,P)}{f(\eta_x,1,P)}\left[\frac{\frac{\partial}{\partial P} f(\eta_x,\rho_x,P)}{\frac{\partial}{\partial \eta_x} f(\eta_x,\rho_x,P)} - \frac{\frac{\partial}{\partial P} f(\eta_x,1,P)}{\frac{\partial}{\partial \eta_x} f(\eta_x,1,P)}\right] \\ &= \frac{\frac{\partial}{\partial \eta_x} f(\eta_x,\rho_x,P)}{2Pf(\eta_x,1,P)}\left[\frac{{}_{\eta_x,\eta_x}\overline{M}_{1,1}(1)}{{}_{\eta_x,\eta_x}\overline{M}_{1,0}(1)} - \frac{{}_{\eta_x,\eta_x}\overline{M}_{1,1}(\rho_x)}{{}_{\eta_x,\eta_x}\overline{M}_{1,0}(\rho_x)}\right] \\ &= -\frac{\frac{\partial}{\partial \eta_x} f(\eta_x,\rho_x,P)}{2Pf(\eta_x,1,P)} \cdot \frac{{}_{\eta_x,\eta_x}\overline{M}_{1,1}(1)\;{}_{\eta_x,\eta_x}\overline{M}_{1,1}(\rho_x)}{{}_{\eta_x,\eta_x}\overline{M}_{1,0}(1)\;{}_{\eta_x,\eta_x}\overline{M}_{1,0}(\rho_x)} \cdot \frac{\frac{\partial}{\partial \eta_x}\,{}_{\eta_x}r(\rho_x)}{2\,{}_{\eta_x}r(\rho_x)} \end{aligned}$$

which is seen to be positive by theorem 1.2. Together, assertion 1 and (M51-M53) prove that $D_{v_1} Q(\eta_x, \rho_x, P)$ is positive.

Proof of theorem 3: The theorem implicitly states that the association between a point $(\Lambda, P, \eta_a, \rho_a)$ in parameter space and a stable solution (η_x, ρ_x) extends to a well-defined map taking a neighbourhood of $(\Lambda, P, \eta_a, \rho_a)$ to a neighbourhood of (η_x, ρ_x). This is guaranteed by (M37, M38) via the implicit function theorem (IFT) applied to (M30, M31).

Demonstrating assertion 3 is now straightforward:

$$\text{(M54)} \quad \frac{\partial}{\partial \rho_x} Q(\eta_x, \rho_x, P) > 0,$$

cf. (M41). Together with lemma M11.2 this implies that ρ_x strictly increases in η_x by the IFT applied to (M31); η_x in turn strictly increases in η_a by the IFT and (M30, M37).

Similarly, by the IFT and (M30) an infinitesimal change in *P* will entail an infinitesimal change in η_x such that the combination of these infinitesimal changes is proportional to v_1. Since by (M54), lemma M11.3 and the IFT applied to (M31) ρ_x strictly decreases along v_1, this proves assertion 1.

As for assertion 2, since $Q(\eta_x, \rho_x, P)$ strictly increasing and strictly concave in ρ_x, its inverse is strictly convex.

Convergence criterion

We conclude our treatment by deriving a heuristic criterion for convergence of the system (1) to a steady-state. The argument is based on the so-called circular law for random matrices which states that in the limit of large *N* the eigenvalues of a well-behaved $N \times N$ random matrix with entries of variance $\frac{1}{N}$ are distributed uniformly in the complex unit disc. This has been proven for various concepts of well-behavedness [3-7]. It is conjectured that the circular law holds in many more circumstances.

Assume that equation (M30) admits a solution η_x that corresponds to a fixed point of (1). For this fixed point to be stable the eigenvalues of the Jacobian of the r.h.s. of (1) must have negative real part. This will be the case precisely if the eigenvalues of the reduced connectivity matrix $\widetilde{L}$ have real part less than one. $\widetilde{L}$ is obtained from *L* by leaving out the rows and columns corresponding to cells not active in the fixed point. Since connectivity is assumed to be sparse and random these cells form a random subset. If the number of all cells is *N*, the expected number of active cells is ${}_{\eta_x}M_0 N$ and $\widetilde{L}$ is an ${}_{\eta_x}M_0 N \times {}_{\eta_x}M_0 N$ random matrix with approximately independent entries of variance $\frac{P}{N} - \left[\frac{(p_+ - p_-)\lambda}{N}\right]^2$. Numerical evidence suggests that a variant of the circular law applies in this situation (Supplementary Fig. 14). Assuming it does, the eigenvalues of $\widetilde{L}$ other than the Perron-Frobenius eigenvalue

(M55) $l_{\max} \approx \Lambda \, {}_{\eta_x}M_0$

are distributed uniformly in the disc with centre at the origin of the complex plane and radius $R = \sqrt{P \, {}_{\eta_x}M_0 - \frac{(p_+ - p_-)^2 \lambda^2 \, {}_{\eta_x}M_0}{N}}$. We predict convergence precisely if

$\Lambda_{\eta_x} M_0$ and R are both less than one. The criterion correctly predicted convergence and non-convergence of the 10,000 neurone circuit for all parameter combinations tested (Supplementary Fig. 3). The criterion also motivates definition M7.

Fully linear transformations

Fact M12: Let $f \neq 0$ be a linear map between Euclidean spaces V, W and let X_α be the set of all pairs (u,v) of unit vectors in V subtending a given angle $\angle(u,v) = \alpha$. Then the transformed angle has expected value $E(\angle(fu, fv)) = \alpha$ where the average is taken over X_α.

Proof: Since the conclusion is trivial for degenerate angles we assume $\alpha \neq k\pi$ is not an integer multiple of π. Then X_α can be identified with the Stiefel manifold $St(2,V) = O(V)/O(T^\perp)$ of orthonormal 2-frames in V. For clarity we have chosen a base point $(u_0, v_0) \in X_\alpha$ together with its linear span T and orthogonal complement $T^\perp$ in V. As $X_\alpha = St(2,V)$ is a homogeneous space of the orthogonal group $O(V)$ there is precisely one invariant regular Borel measure μ on X_α which is also a probability measure[8]. $St(2,V)$ is via the obvious projection p a principal bundle over the Grassmannian $Gr(2,V) = O(V)/(O(T) \times O(T^\perp))$ of planes in V. It clearly suffices to prove the statement for integer fractions $\alpha = \frac{2\pi}{k}$. Let $o_\alpha \in O(T)$ be rotation by α. The right action of o_α on an element $(ou_0, ov_0) \in p^{-1}(oT)$ is given by $(ou_0, ov_0)^{o_\alpha} = (oo_\alpha u_0, oo_\alpha v_0)$. Since the winding number of a linear map $\in GL(2,\mathbf{R})$ equals ± 1 (e.g. by the singular value decomposition) we have almost everywhere

$$\begin{aligned}(\text{M56})\quad \sum_{n=1}^{k} \angle f\left(\left(ou_0, ov_0\right)^{o_\alpha^n}\right) &= \sum_{n=1}^{k} \angle\left(foo_\alpha^{n-1}v_0, foo_\alpha^{n}v_0\right) \\ &= \angle\left(foo_\alpha^{0}v_0, foo_\alpha^{n}v_0\right) = 2\pi\end{aligned}.$$

Because $O(V)$ is compact the measure μ is invariant under right action of $O(T)$. Thus

$$\begin{aligned}(\text{M57})\quad kE(\angle(fu, fv)) &= k\int_{X_\alpha} \angle f(u,v)d\mu(u,v) \\ &= \sum_{n=1}^{k} \int_{X_\alpha} \angle f\left((u,v)^{o_\alpha^n}\right)d\mu(u,v) = 2\pi\end{aligned}.$$

Remark 13: What does Fact M12 mean for Pearson correlation? Put differently, what are the effects of mean subtraction c_V, c_W and taking cosines?

1. Denote by $\mathbf{1}_V$ and M_V the kernel and image of mean subtraction c_V in *V*, respectively. We need a geometry on the set $St(M_V)\times\mathbf{1}_V\times\mathbf{1}_V$ of pairs (*u*,*v*) of vectors of unit variance. Concerning $St(M_V)$ the only plausible measure is the unique invariant probability measure μ_M as above. The probability measure μ_1 can be freely chosen. The only way mean subtraction can circumvent fact M12 is if $c_W \circ f\big|_{1_V}$ is large. The average image angle then strongly depends on the distribution μ_1 of the mean in *V*. Output correlation thus strongly depends on something that is invisible to input correlation. Therefore in this situation Pearson correlation cannot be used to form a meaningful measure of pattern separation.

2. Assume now that $c_W \circ f$ factors through c_V. The cosine, being nonlinear, will not in general preserve averages; in fact, using Jensen's inequality it is easy to

construct examples where a fixed input correlation on average (but not uniformly) slightly increases or decreases. However, this is an effect of the nonlinearity of the measure itself, not of the transformation, and does therefore not represent a relevant change.

References

1. Abramowitz, M. & Stegun, I.A. *Handbook of mathematical functions : with formulas, graphs, and mathematical tables* (Dover Publications, 1970).
2. Gupta, A.K. & Tracy, D.S. Recurrence relations for the moments of truncated multinormal distribution. *Communications in Statistics - Theory and Methods* **5**, 855-865 (1976).
3. Bai, Z.D. Circular law. *Ann. Probab.* **25**, 494-529 (1997).
4. Girko, V.L. Circular law. *Theory Probab. Appl.*, 694-706 (1984).
5. Ginibre, J. Statistical ensembles of complex, quaternion, and real matrices. *Journal of Mathematical Physics* **6**, 440-449 (1965).
6. Mehta, M.L. *Random Matrices and the Statistical Theory of Energy Levels* (Academic Press, New York, 1967).
7. Tao, T. & Vu, V. Random matrices: The circular law. *Commun. Contemp. Math.* **10**, 261-307 (2008).
8. Abbaspour, H. & Moskowitz, M. *Basic Lie theory* (World Scientific Publishing, New Jersey, 2007).

Appendix A2

Supplementary Figures and Table for chapter 1

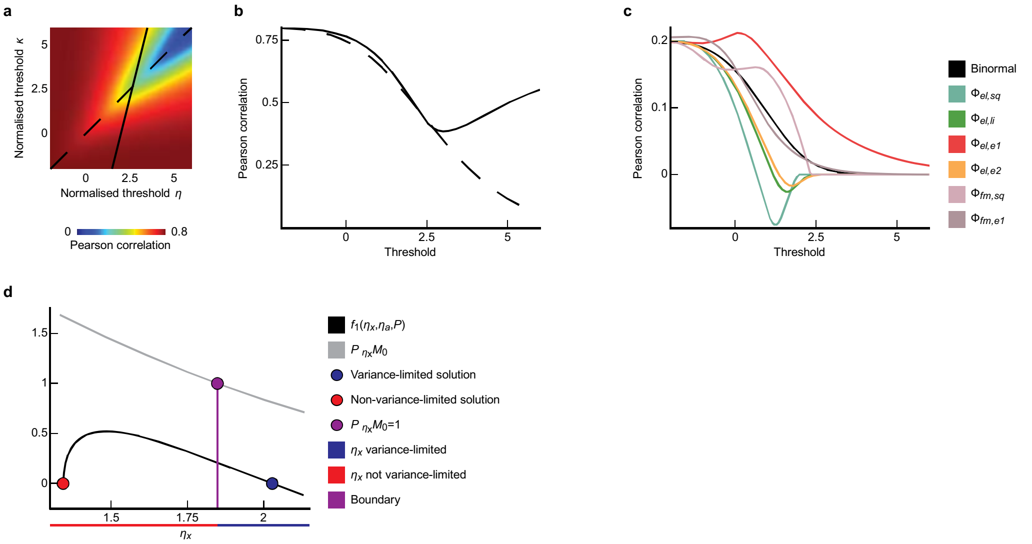

Supplementary Figure 1 | Counterexamples demonstrating that assumptions of theorems 1 and M8 cannot be omitted. **a**, Pearson correlation of the thresholded binormal ${}_{\eta,\kappa}\Phi_{\rho}$ at $\rho = 0.8$ as a function of the normalized thresholds η and κ. If $\mu(a) = \mu(a_\alpha) = \mu(a_\beta)$ and $\mathrm{var}(a) = \mathrm{var}(a_\alpha) = \mathrm{var}(a_\beta)$ as assumed in the model, η will equal κ (dashed line). The solid line indicates the relation between η and κ if $\mathrm{var}(a_\alpha) = 16\,\mathrm{var}(a_\beta)$ and $\mu(a_\alpha) = \mu(a_\beta) - 8\sqrt{\mathrm{var}(a_\beta)}$. **b**, Pearson correlation along the two lines indicated in a, parameterized by κ. If the two stimuli have different means and variances (solid line) monotonicity is lost. **c**, Effect of thresholding on the Pearson correlation of various bivariate distributions other than the binormal. The distributions are derived from $\tilde{\phi}_{el,sq}(x,y) = \Theta(1 - f_{el}(x,y))$, $\tilde{\phi}_{el,li}(x,y) = [1 - f_{el}(x,y)]_+$,

$$\tilde{\phi}_{el,e1}(x,y) = e^{-f_{el}(x,y)},\ \tilde{\phi}_{el,e2}(x,y) = \left[e^{-\frac{f_{el}^2(x,y)}{2}} - 0.1 \right]_+ ,$$

$$\tilde{\phi}_{fm,sq}(x,y) = \int_{-\infty}^{\infty} \Theta\left(1 - \frac{|t|}{\sqrt{0.2}}\right) \Theta\left(1 - \frac{|x-t|}{\sqrt{0.8}}\right) \Theta\left(1 - \frac{|y-t|}{\sqrt{0.8}}\right) dt$$ and

$$\tilde{\phi}_{fm,e1}(x,y) = \int_{-\infty}^{\infty} e^{-\frac{|t|}{\sqrt{0.2}} - \frac{|x-t|}{\sqrt{0.8}} - \frac{|y-t|}{\sqrt{0.8}}} dt$$ by normalizing integral and variance to one. Here

$$f_{el}(x,y) = \sqrt{\frac{x^2 + y^2 - 0.4xy}{0.96}}$$. In all cases monotonicity is lost. However, all preserve the general behavior of the binormal, consistent with its universal character. **d**, If variance-limitedness is not enforced, solutions to (M31) are not necessarily unique. Parameters in this particular counterexample are $\Lambda = -31.5$, $\eta_a = 1.946559$, $P = 31.0078125$. For details see Supplementary Equations and Mathematical Analyses.

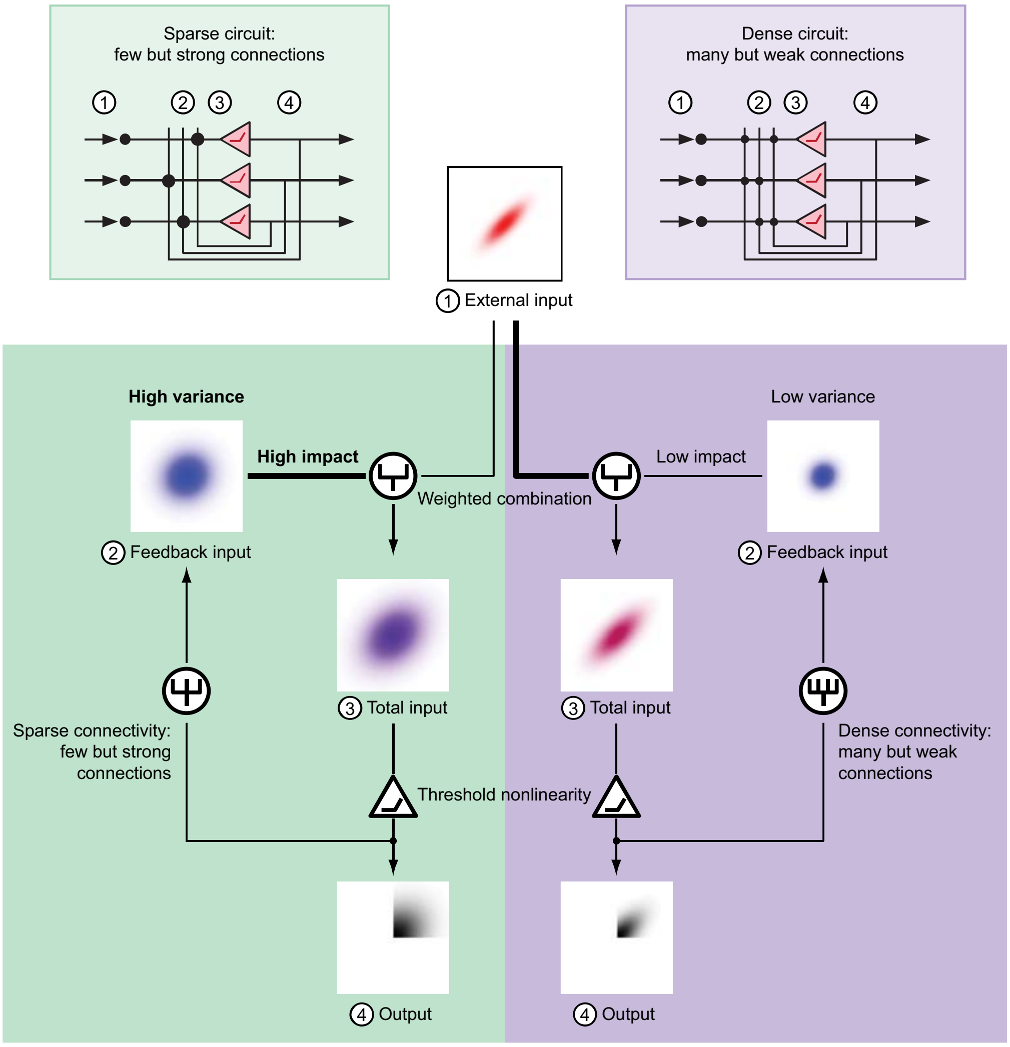

Supplementary Figure 2 | Illustration of the reTIDe mechanism. “External input” (1) shows a binormal distribution representing a pair of correlated input patterns. The external input is combined with the feedback input (2) from the network, yielding the total input (3). The total input is thresholded to generate the output (4), which is also fed back into the network. Because thresholding reduces pattern correlation (TIDe), the correlation between thresholded feedback patterns (2) and total input patterns (3) is lower than the correlation between external input patterns (1). Feedback of the output pattern therefore seeds a regenerative loop that progressively amplifies the decorrelation produced by TIDe alone. The strength of this amplification depends on the relative contributions of the external input (1) and the feedback input (2) to the total input (3). In dense networks (right) the input to each neuron is an average over many other neurons; therefore the feedback has low variance and contributes little to the total input. In sparse networks (left), the feedback pattern has higher variance and contributes more to the total input. As a consequence, sparse connectivity enhances the amplification of TIDe in recurrent networks (reTIDe).

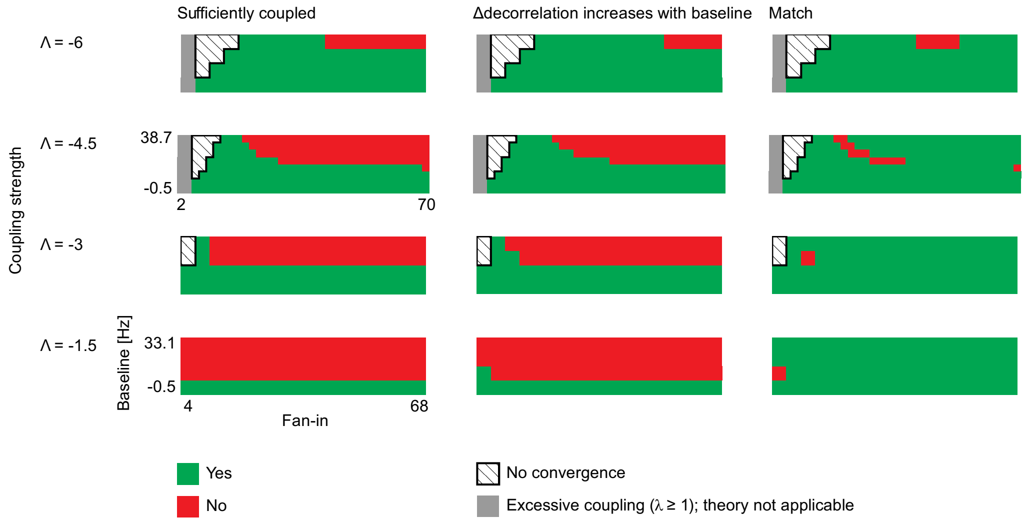

Supplementary Figure 3 | ”Sufficient coupling” is a good criterion to predict the effect of baseline activation on pattern decorrelation (Supplementary Equations and Mathematical Analyses). Green color depicts regions in parameter space where the gain in decorrelation increases with baseline activation in theoretical predictions (left) and simulations (center). Right: match between prediction and simulation. As expected (theorem 3.3) there are no false positives. Furthermore, false negatives are rare, making sufficient coupling a strong predictor. Gray areas depict parameter combinations for which the theory is not applicable because coupling is too strong ($\lambda \geq 1$). Hatched areas depict parameter regimes where convergence to a steady-state does not occur in theoretical predictions or simulations. Note that the match between predicted and observed convergence is perfect.

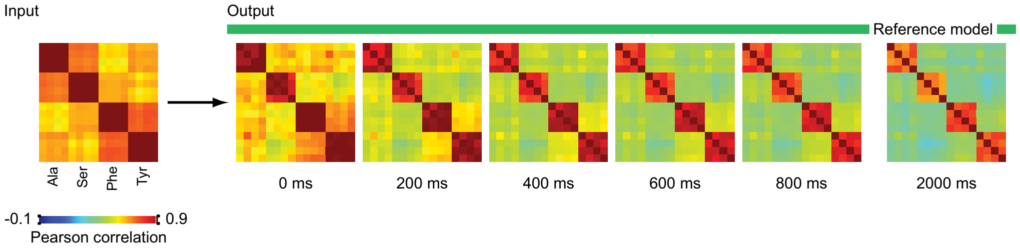

Supplementary Figure 4 | Tolerance of reTIDe against small variations in the input. Gaussian noise with approximately 3% of the average variance was added to four input patterns with relatively high Pearson correlation (Ala, Ser, Phe, Tyr). Negative values in the resulting patterns were set to zero. Four variants of each stimulus were created and processed with 100 realizations of the reference network. Response patterns were pooled and correlation matrices calculated. Similarity between noisy versions of the same input patterns (blocks along the diagonal) were clearly preserved in the output. Over time, the difference between within-block and across-block correlation increased. ReTIDe therefore facilitates pattern classification.

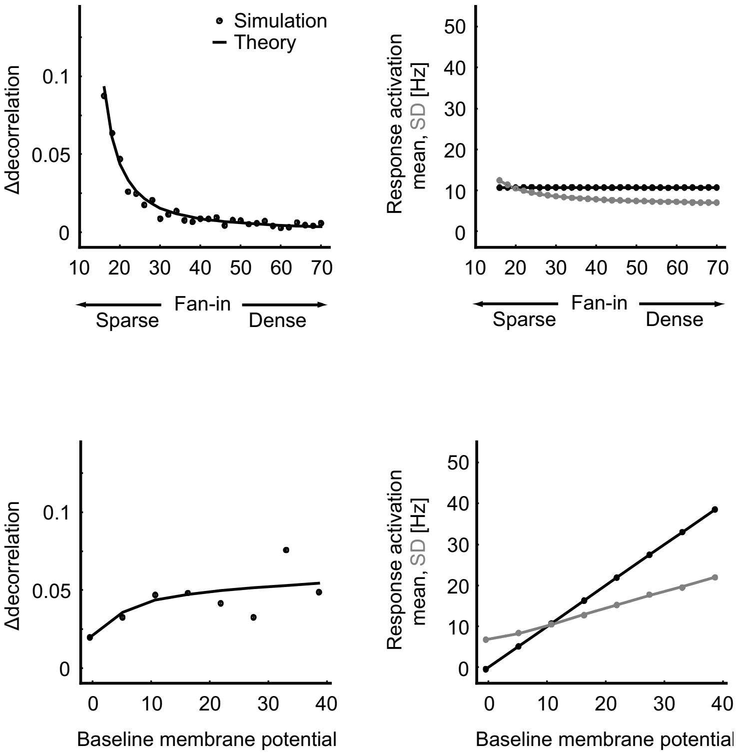

Supplementary Figure 5 | Validation of SNORE theory for mixed excitatory-inhibitory networks. Top: $\mu(a)$ = 10.7 Hz. Bottom: fan-in $p = 20$. Other conventions as in Fig. 4a–d.

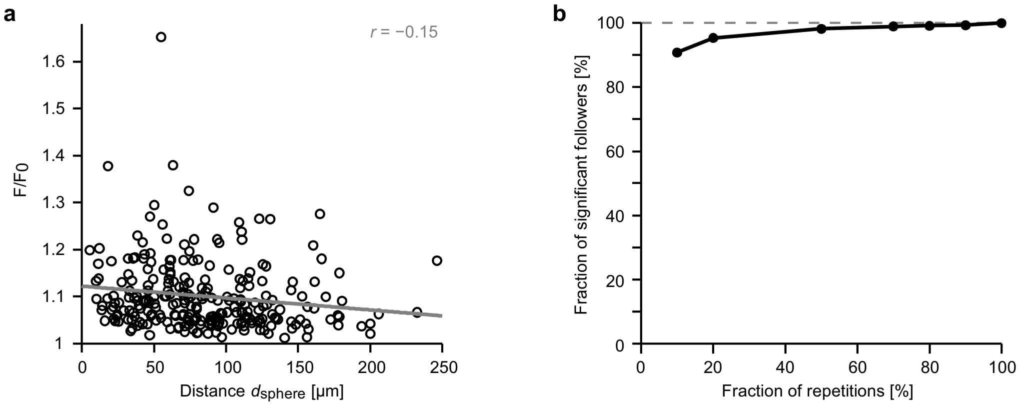

Supplementary Figure 6 | Forward optical probing. **a**, Distance-dependence of signal amplitude. Response intensity of follower neurons is plotted as a function of distance d_{sphere} (Fig. 5c) from the trigger neuron. Line: linear fit; correlation: $r = -0.15$. Response amplitude decreases only slightly with the distance of the follower neuron, consistent with the assumption that the evoked action potentials propagate actively within the dendritic tree of the mitral cells. Hence, the approximately exponential decay of follower probability with distance (Fig. 5d) cannot be explained by a distance-dependent decrease in the response intensity of follower neurons. **b**, Fraction of followers with statistically significant responses as a function of the fraction of repetitions included in the analysis. The total number of repetitions for each follower was 20. For each fraction of repetitions, a subset of trials was drawn randomly and significance of the response was determined by a Mann-Whitney U test ($P < 0.05$, Methods). This analysis was repeated 100 times for each data point. The fraction of significant followers does not decrease steeply with the fraction of repetitions, indicating that identification of followers was robust.

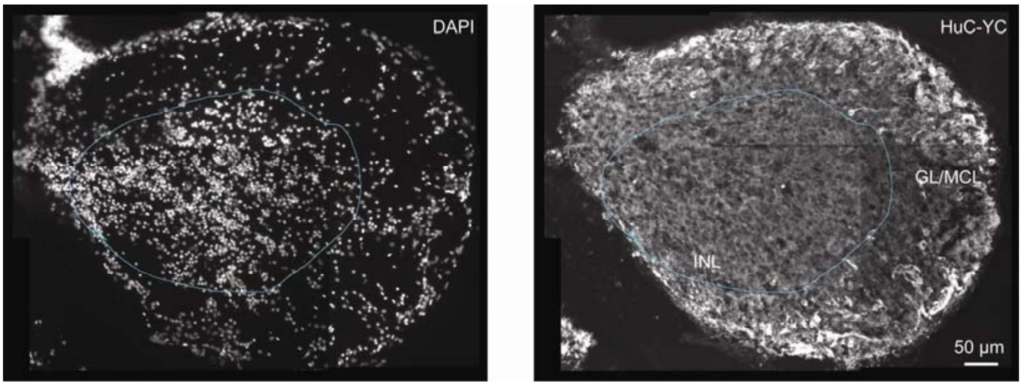

Supplementary Figure 7 | Cell counts in the OB. To estimate the total number of potential follower neurons of mitral cells in the OB, we assume that follower neurons are exclusively interneurons. We counted nuclei in the deep (interneuron) layers in a series of 14 µm sections through the whole OB (30 sections) stained with DAPI (left). The boundary of the deep layer (INL; blue outline) was drawn based on HuC-YC fluorescence in the same section, which marks sensory afferents and mitral cells in the glomerular/mitral cell layer (GL/MCL; right). Somata in the INL of all sections were then counted using automated procedures in Imaris (Bitplane). Four sections were lost during the histological procedure and soma numbers were interpolated. The total number of somata detected in all sections was 24,822. Assuming that the OB contains approximately 25 % non-neuronal cells, the total number of interneurons in the deep layers is estimated to be ~20,000. This number is assumed to be a conservative (low) estimate of the total number of potential mitral cell followers because the real fraction of non-neuronal cells may be smaller than 25 %, and because interneurons in the GL/MCL were not included in the count.

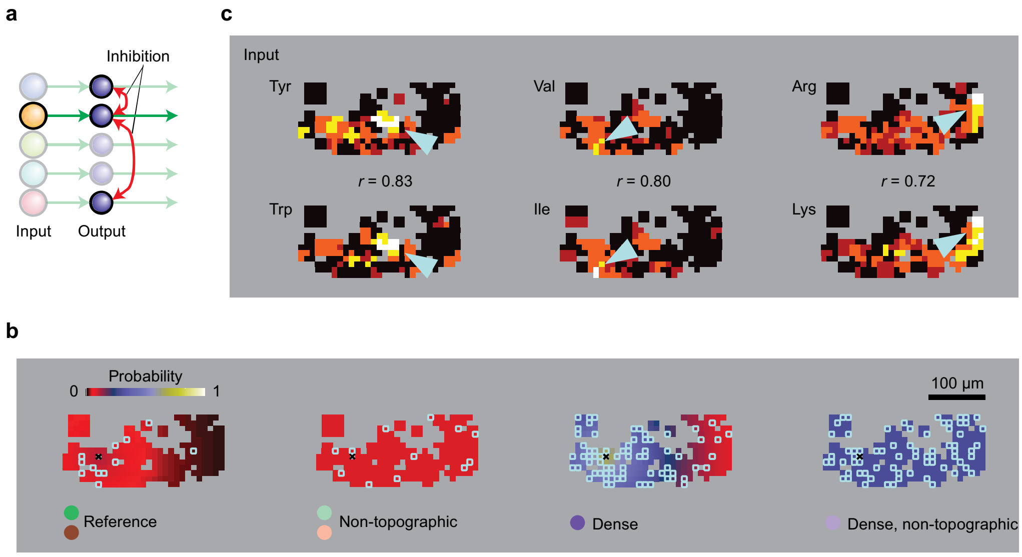

Supplementary Figure 8 | Computer model of the olfactory bulb. **a**, Model architecture. Mitral cells receive spatially patterned excitatory inputs and make reciprocal inhibitory connections to stochastic subsets of other mitral cells. **b**, Connectivity patterns. Each square depicts one mitral cell. Connection probability and connectivity are illustrated for the mitral cell marked by the cross. Color map shows the distribution of connection probability. Open squares show mitral cells that were connected to the neuron marked by the cross by random selection of connections based on the underlying probability distribution. Left: sparse connectivity with exponentially decaying (topographic) connection probability, representing the reference model derived from experimental data. Right: non-topographic and/or dense connectivity patterns. **c**, Examples of rasterized odor-evoked glomerular activation patterns in zebrafish[1]. Patterns evoked by structurally similar pairs of odors (Tyr/Trp, Val/Ile, Arg/Lys) are highly correlated (*r*, Pearson correlation coefficient); overlap is particularly high within foci of active mitral cells (arrowheads).

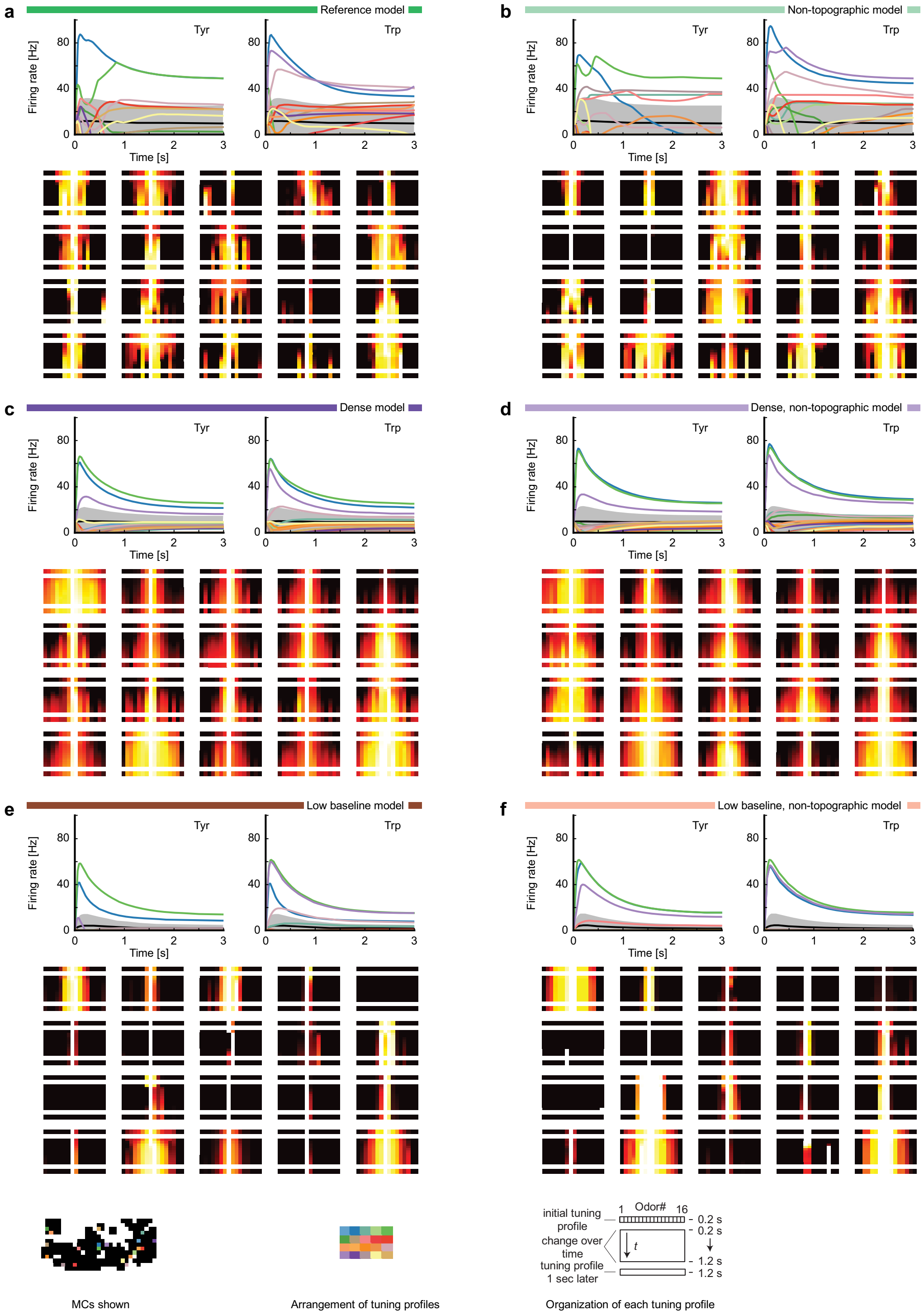

Supplementary Figure 9 | Dynamics of responses produced by different OB models. Line plots show responses of 20 mitral cells to two similar inputs (Tyr and Trp) as a function of time. Three mitral cells were chosen from the central cluster of high afferent activity shared by Tyr and Trp (Supplementary Fig. 8b, arrowhead[1]); the remaining 17 mitral cells were selected randomly. Positions of mitral cells are indicated by the color code at the bottom. Color plots show the tuning profiles of the same neurons to all 16 amino acid stimuli as a function of time (see bottom right). The first separated line in each plot shows the tuning profile at response onset (200 – 300 ms). Odors were arranged such that the evoked firing rates decrease from the center outwards. The central field shows the tuning profile in successive time bins as the odor response evolves. The order of odors is preserved for each mitral cell. The last separated line shows the tuning profile 1200 ms after the initial tuning profile. These plots can be directly compared to experimental data from zebrafish mitral cells[2]. **a**, reference model. **b–f**, models with dense connectivity, low baseline membrane potential and no topography. Note that in models with sparse connectivity and high baseline membrane potential (reference model and non-topographic model; top), a subset of mitral cells show pronounced firing rate modulations during the initial phase of the odor response and a dynamic change in their tuning profiles, similar to experimental observations in zebrafish[2-4]. Other models, in contrast, produced more stereotyped mitral cell responses and tuning profiles that were stable or broadened over time.

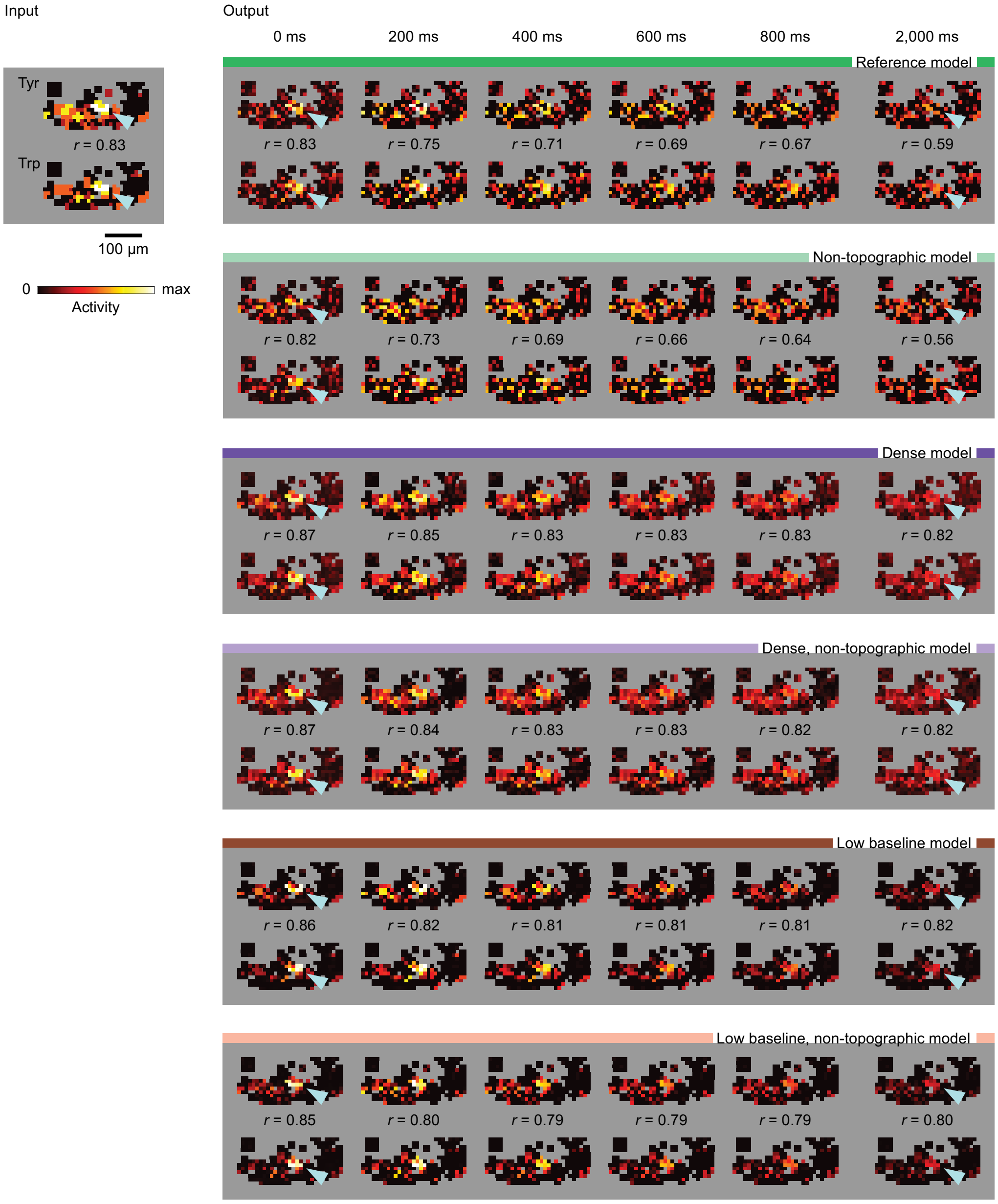

Supplementary Figure 10 | Output patterns produced by different OB models. Left: two input patterns evoked by structurally similar odors (Tyr and Trp)[1]. Right: Time series of corresponding output patterns produced by OB models. *r*: Pearson correlation coefficient. Top (reference model) is identical to Fig. 6a. Substantial pattern decorrelation and disappearance of the central focus (arrowhead) observed in experimental data[2,4,5] occurred only in models with sparse connectivity and high baseline membrane potential (green).

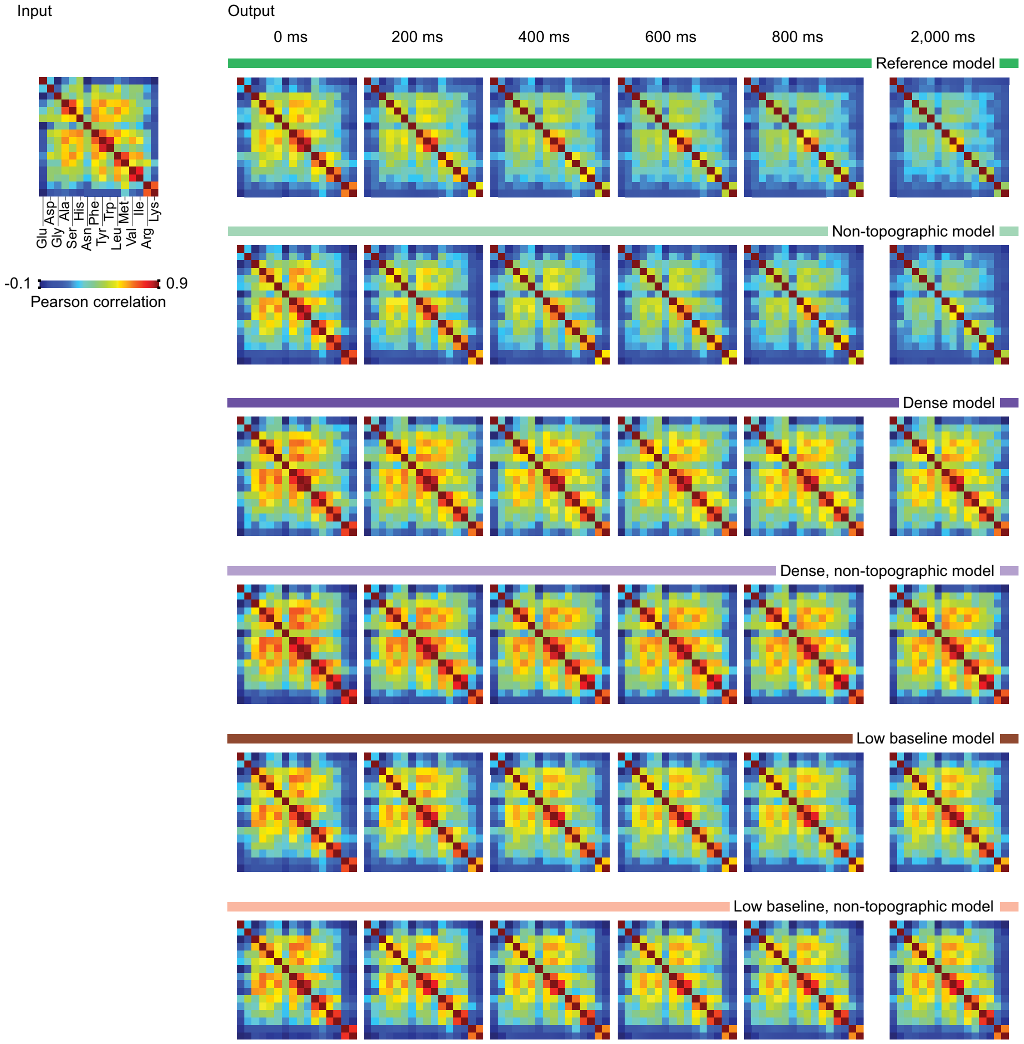

Supplementary Figure 11 | Correlations between output patterns produced by different OB models. Left: color-coded correlation matrix showing correlations between all 16 input patterns. Right: time series of correlations between the corresponding output patterns produced by different OB models. Decorrelation comparable to that observed experimentally[2-4,6] occurred only in models with sparse connectivity and high baseline membrane potential (green).

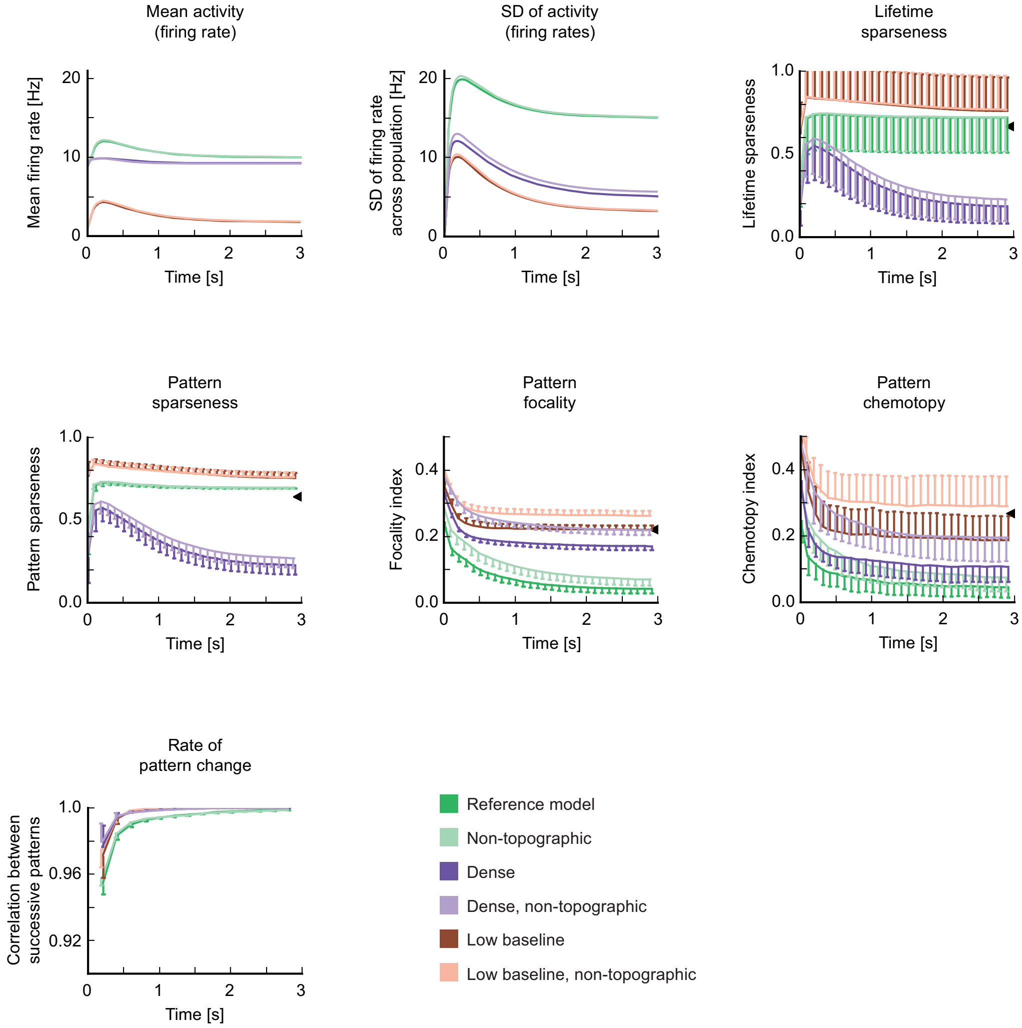

Supplementary Figure 12 | Outputs of different OB models as a function of time. Time courses and absolute values obtained with the reference model and the non-topographic model correspond well to experimental data for all measures: Mean activity (firing rate)[2], standard deviation (SD) of population activity[2], lifetime sparseness[2,4,5], pattern sparseness[2,4,5], pattern focality[5], pattern chemotopy[5], and rate of pattern change[4]. Outputs of other models are clearly different. Focality and chemotopy indices were calculated as described previously[5].

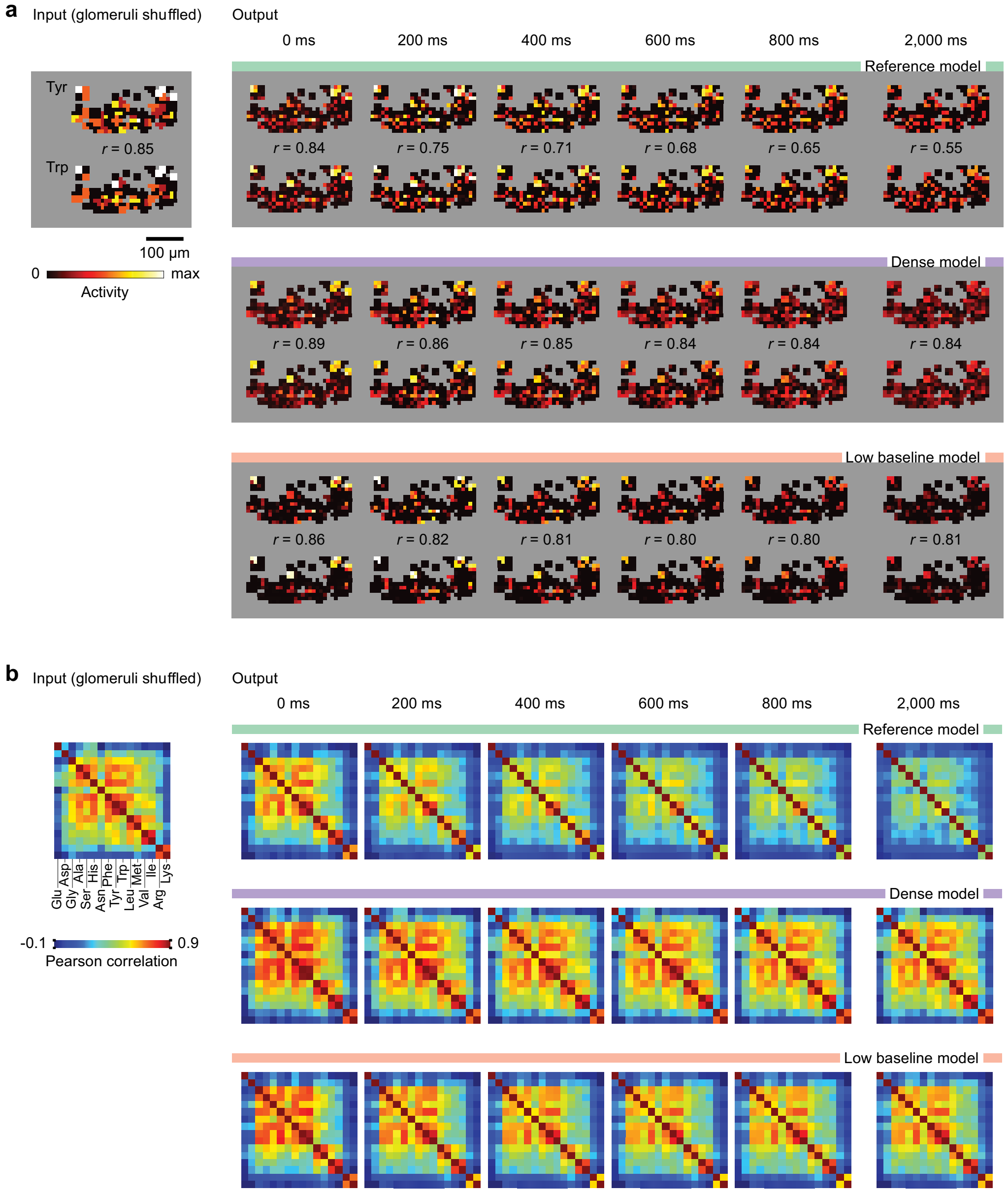

Supplementary Figure 13 | Output patterns and correlations in response to non-chemotopic input patterns, generated by random shuffling of glomerular positions. **a**, Left: two input patterns evoked by structurally similar odors (Tyr and Trp)[1] after shuffling of glomerular positions. Right: Time series of corresponding output patterns produced by OB models. *r*: Pearson correlation coefficient. **b**, Left: color-coded correlation matrix showing correlations between all 16 input patterns. Right: time series of correlations between the corresponding output patterns produced by different OB models. Decorrelation obtained with the reference model was comparable to that obtained with chemotopic inputs (Fig. 7; Supplementary Figs. 11, 12).

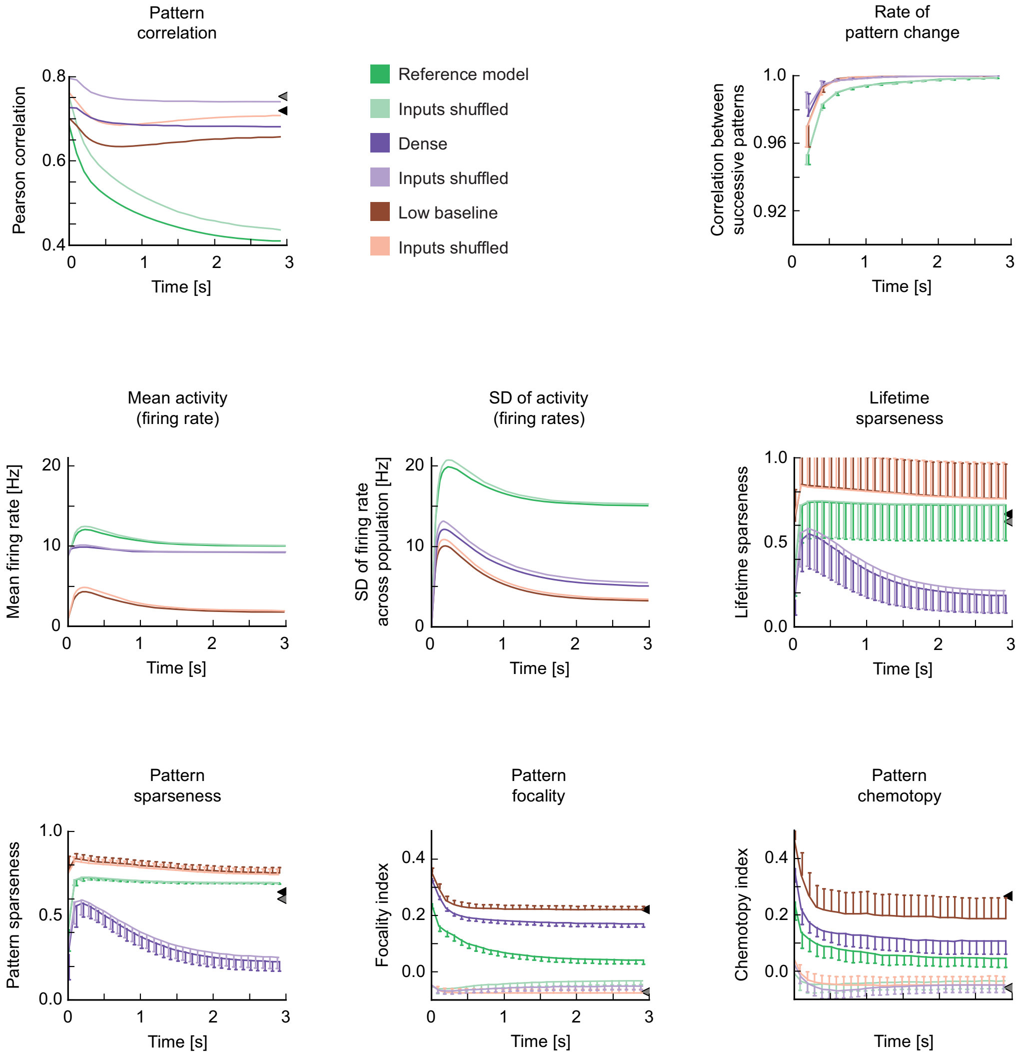

Supplementary Figure 14 | Outputs of different OB models as a function of time for original (chemotopic) and non-chemotopic input patterns. In non-chemotopic input patterns, positions of glomeruli were randomly shuffled in the same manner for all odors. Top left graph shows pattern correlation as a function of time (10 most similar pairs of patterns). Note that eliminating chemotopy had only a minor effect on pattern decorrelation by the reference model (dark green vs. light green lines). For all other measures except those quantifying topological pattern properties (focality and chemotopy), shuffling of glomerular positions also had only minimal effects on model output. Conventions as in Supplementary Fig. 12.

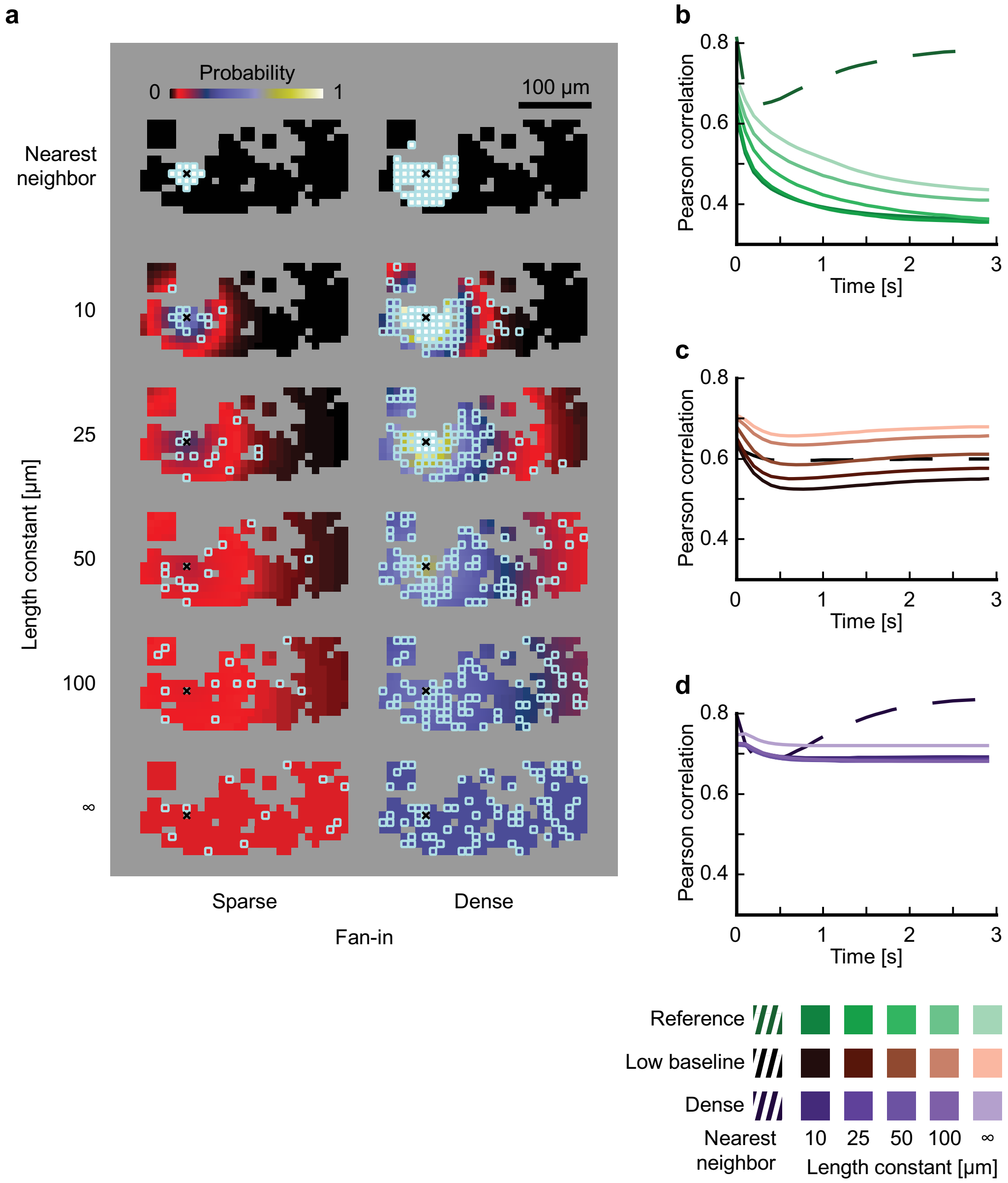

Supplementary Figure 15 | Dependence of pattern decorrelation on length constant in models with distance-dependent connectivity. **a**, Connectivity patterns for different length constants and nearest neighbor connectivities (top row). Conventions as in Supplementary Fig. 8c. **b-d**, Corresponding decorrelation for the reference, low baseline and dense models, respectively. Pooled data from 100 realizations for each parameter combination except nearest neighbor models, which are non-random.

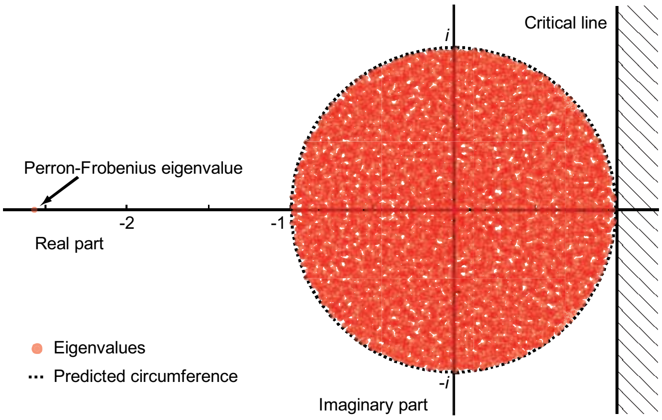

Supplementary Figure 16 | Numerical evidence for the circular law used to derive the convergence criterion (Supplementary Equations and Mathematical Analyses). Shown are the 6127 eigenvalues of the reduced connectivity matrix $\tilde{L}$ of the steady-state of a single simulation at the reference parameter set $\Lambda = -4.5, \eta_a = -4.85, P = 1.6875$. All eigenvalues have a real part less than one, indicating stability. The distribution of eigenvalues is well predicted by the circular law (dotted circle).

	Ephys	Img.	Expt	Ref.	Non-topo	Dense	D., n-t.	Low b.	L.b., n-t.
Baseline activity [Hz]	8.8		8.8	8.8	8.8	8.8	8.8	0.98	0.98
Evoked activity [Hz]	10		10	10	10	9.2	9.2	1.8	1.8
SD of activity [Hz]	14		14	15	15	5.1	5.6	3.2	3.3
Lifetime sparseness	0.6	0.7	0.65	0.72	0.72	0.18	0.23	0.76	0.77
Pattern sparseness	0.65	0.7	0.675	0.69	0.69	0.23	0.27	0.75	0.76
Chemotopy		0.06	0.06	0.045	0.074	0.11	0.2	0.19	0.29
Focality		0.04	0.04	0.041	0.07	0.17	0.22	0.22	0.26
Pattern correlation	0.45	0.25	0.35	0.41	0.44	0.68	0.72	0.66	0.68

Supplementary Table 1 | Quantitative comparison between experimental data and model output. Experimental data were measured by electrophysiology (“Ephys”)[2,4] and/or temporally deconvolved 2-photon calcium imaging (“Img.”)[5]. Column “Expt” gives the mean value of experimental measurements when readouts were measured by both methods or the individual values otherwise. Remaining columns show corresponding outputs of different OB models: “Ref”., reference model; “Non-topo”, non-topographic model; “Dense”, model with dense connectivity; “D., n-t.”, model with dense and non-topographic connectivity; “Low b.”, model with low baseline membrane potential; “L.b., n-t.”, model with low baseline membrane potential and non-topographic connectivity. Colors correspond to plots.

References

1. Friedrich, R.W. & Korsching, S.I. Combinatorial and chemotopic odorant coding in the zebrafish olfactory bulb visualized by optical imaging. *Neuron* **18**, 737-752 (1997).
2. Friedrich, R.W. & Laurent, G. Dynamic optimization of odor representations in the olfactory bulb by slow temporal patterning of mitral cell activity. *Science* **291**, 889-894 (2001).
3. Friedrich, R.W., Habermann, C.J. & Laurent, G. Multiplexing using synchrony in the zebrafish olfactory bulb. *Nat. Neurosci.* **7**, 862-871 (2004).
4. Friedrich, R.W. & Laurent, G. Dynamics of olfactory bulb input and output activity during odor stimulation in zebrafish. *J. Neurophysiol.* **91**, 2658-2669 (2004).
5. Yaksi, E., Judkewitz, B. & Friedrich, R.W. Topological reorganization of odor representations in the olfactory bulb. *PLoS Biol.* **5**, e178 (2007).
6. Yaksi, E. & Friedrich, R.W. Reconstruction of firing rate changes across neuronal populations by temporally deconvolved Ca^{2+} imaging. *Nat. Methods* **3**, 377-383 (2006).

Appendix A3

Theory supplementing chapter 2

Univariately thresholded binormal

Consider the standard η-rectified ρ-correlated binormal distribution ${}_\eta\Phi_\rho$ with density

$$ {}_\eta\varphi_\rho(x,y) = \Theta(x)\varphi_\rho(x+\eta,y) + \delta(x)\int_{-\infty}^{0}\varphi_\rho(s+\eta,y)ds \tag{A3.1} $$

which emerges if a threshold η is applied to only one variate of Φ_ρ. Its premoments

$$ {}_\eta M_{m,n}(\rho) = \begin{cases} 0 & n<0 \\ \displaystyle\int_{-\infty}^{\infty}\int_{0}^{\infty}\frac{s^m t^n}{m!n!}\varphi_\rho(s+\eta,t)dsdt & m,n\geq 0 \end{cases} \tag{A3.2} $$

satisfy

$$ {}_\eta M_{m,0}(\rho) = {}_\eta M_m \tag{A3.3} $$

$$ \frac{d}{d\eta}{}_\eta M_{m,n}(\rho) = -{}_\eta M_{m-1,n}(\rho) \tag{A3.4} $$

$$ \frac{d}{d\rho}{}_\eta M_{m,n}(\rho) = {}_\eta M_{m-1,n-1}(\rho) \tag{A3.5} $$

$$ {}_\eta M_{m-1,n}(\rho) + \rho\,{}_\eta M_{m,n-1}(\rho) = (m+1)\,{}_\eta M_{m+1,n}(\rho) + \eta\,{}_\eta M_{m,n}(\rho) \tag{A3.6} $$

$$ {}_\eta M_{m,n-1}(\rho) + \rho\,{}_\eta M_{m-1,n}(\rho) = (n+1)\,{}_\eta M_{m,n+1}(\rho) \tag{A3.7} $$

$$\begin{aligned}(1-\rho^2)\,{}_\eta M_{m-1,n}(\rho)+\rho(n+1)\,{}_\eta M_{m,n+1}(\rho)\\ =\rho^2(m+1)\,{}_\eta M_{m+1,n}(\rho)+\eta\,{}_\eta M_{m,n}(\rho)\end{aligned} \qquad (A3.8)$$

$$\begin{aligned}(1-\rho^2)\,{}_\eta M_{m,n-1}(\rho)+\rho(m+1)\,{}_\eta M_{m+1,n}(\rho)\\ =(n+1)\,{}_\eta M_{m,n+1}(\rho)-\rho\eta\,{}_\eta M_{m,n}(\rho)\end{aligned} \qquad (A3.9)$$

Definition (A3.2) extends to arbitrary *m,n* via (A3.4). For *m,n* positive the premoment ${}_\eta M_{m,n}(\rho)$ equals the *m,n*th moment of ${}_\eta\Phi_\rho$ divided by $m!n!$.

Numerical solution of model II

The presence of a dominant solution precluded a forward iteration through (2.15) because it would have been numerically unsound. I therefore resorted to a backward scheme built around a function `backward`$(\beta_-, n_\infty, p, \lambda, \eta_x, \eta_a, \rho_a)$. Assuming $C_{2n_\infty-2}, C_{2n_\infty}$ are small such that (2.8—2.11) apply this function first calculated C_{2n_∞} and $C_{2n_\infty-2}$ using (2.5,2.8—2.11) and then backward iterated through (2.15). The iteration step involved inversion of the function $\vartheta \mapsto {}_{\eta_x,\eta_x}\overline{M}_{1,1}(\vartheta)$ and was therefore susceptible to domain errors. If, however, no such error was encountered the function finally returned C_0 and if requested C_2. After temporarily setting ρ_a to unity η_x was determined in two hierarchical root finding steps. Keeping $n_\infty, p, \lambda, \eta_a, \rho_a$ fixed (2.5,2.6,2.8—2.11,2.15) define a map `beta_inf`$: \eta_x \mapsto \beta_-$ which was implemented using the secant method on `backward`. After combining `backward` and `beta_inf` to a map $\eta_x \mapsto C_2$, finally using (2.14) allowed pinning down η_x, again by the secant method. This procedure was repeated for successively incremented values of n_∞ until the relative difference between subsequent results fell within a preset tolerance. With η_x known, β_- (which depends on ρ_a) could be calculated from ρ_a using `backward` and another application of the secant method to the deviation from (2.14). From β_- $\rho_x = C_0(\rho_a)$ was gained using `backward`.

Normal theory—direct approach

To get around the somewhat arbitrary constraint (2.5) I tried to more directly calculate $\{B_n(\rho_a)\}_n$ and $\{C_n(\rho_a)\}_n$ by inverting $I - \tilde{L}$ and ${}^T(I - \tilde{L})(I - \tilde{L})$ where $\tilde{L}$ is a matrix derived from L to account for thresholding.

For this I will need some combinatorial tools which I now derive. I will write $\mathbf{N} = \{1,2,3,\ldots\}$ and $\mathbf{N}_0 = \mathbf{N} \cup \{0\}$ for the positive and nonnegative integers, respectively. I will also use the Pochhammer symbol

$$x^{(n)} = \frac{\Gamma(x+n)}{\Gamma(x)}. \tag{A3.10}$$

Regarding the elements of $\mathbf{N}$ as the vertices of a graph with edges between successive numbers define the path count

$$\begin{Bmatrix} n \\ m \end{Bmatrix} = \left|P_{\mathbf{N}}^{n,m}\right| \quad m \in \mathbf{N}_0, n \in \mathbf{N} \tag{A3.11}$$

where

$$P_{\mathbf{N}}^{n,m} = \{\text{paths in } \mathbf{N} \text{ of length } n + 2m - 1 \text{ from } n \text{ to } 1\} \quad m \in \mathbf{N}_0, n \in \mathbf{N} \tag{A3.12}$$

and, similarly, the conditional path count

$$\begin{Bmatrix} n \\ m \;\; i \end{Bmatrix} = \left|P_{\mathbf{N}}^{n,m,i}\right| \quad m, i \in \mathbf{N}_0, n \in \mathbf{N} \tag{A3.13}$$

where

$$P_{\mathbf{N}}^{n,m,i} = \{\text{paths} \in P_{\mathbf{N}}^{n,m} \text{ that hit } 1 \text{ precisely } i+1 \text{ times}\} \quad m, i \in \mathbf{N}_0, n \in \mathbf{N}. \tag{A3.14}$$

I now derive basic properties of and explicit expressions for (A3.11,A3.13). Trivially

$$\left\{ \begin{matrix} n \\ 0 \end{matrix} \right\} = 1 \qquad \text{(A3.15)}$$

and

$$\left\{ \begin{matrix} 1 \\ m \end{matrix} \right\} = \left\{ \begin{matrix} 2 \\ m-1 \end{matrix} \right\} \qquad m \in \mathbf{N}. \qquad \text{(A3.16)}$$

If $m > 0, n > 1$ the second vertex in paths counted by $\left\{ \begin{matrix} n \\ m \end{matrix} \right\}$ is either $n-1$ or $n+1$. This defines two complementary subsets and leads to the identity

$$\left\{ \begin{matrix} n \\ m \end{matrix} \right\} = \left\{ \begin{matrix} n-1 \\ m \end{matrix} \right\} + \left\{ \begin{matrix} n+1 \\ m-1 \end{matrix} \right\} \qquad m > 0, n > 1. \qquad \text{(A3.17)}$$

using which the identity

$$\left\{ \begin{matrix} n \\ m \end{matrix} \right\} = \frac{n(n+m+1)^{(m-1)}}{m!} = \frac{\left(\frac{n}{2}\right)^{(m)} \left(\frac{n+1}{2}\right)^{(m)}}{(n+1)^{(m)}} \frac{4^m}{m!} \qquad \text{(A3.18)}$$

is easily verified. The rightmost expression is useful because it helps compute certain sums of path counts in terms of the Gaussian hypergeomtric series.

As for $\left\{ \begin{matrix} n \\ m \;\; i \end{matrix} \right\}$, trivially

$$\left\{ \begin{matrix} n \\ m \;\; i \end{matrix} \right\} = 0 \qquad i > m. \qquad \text{(A3.19)}$$

Further observe

$$\left\{ \begin{matrix} n \\ m \;\; 0 \end{matrix} \right\} = \left\{ \begin{matrix} n-1 \\ m \end{matrix} \right\} \qquad n > 1 \qquad \text{(A3.20)}$$

because corresponding paths are in bijection via

$$\begin{matrix} (v_1 = n, & v_2, & \ldots, & v_{n+2m-1} = 2, & v_{n+2m} = 1) \\ & & \updownarrow & & \\ (v'_1 = v_1 - 1, & v'_2 = v_2 - 1, & \ldots, & v'_{n+2m} = 1) & \end{matrix} \qquad \text{(A3.21)}$$

Similarly,

$$\begin{Bmatrix} n \\ m \quad i \end{Bmatrix} = \begin{Bmatrix} n-1 \\ m+1 \quad i+1 \end{Bmatrix} \qquad n > 1 \tag{A3.22}$$

via the bijection

$$\begin{array}{cccccc} (v_1 = n, & v_2, & \ldots, & v_h = 2, & & v_{h+1}, \quad \ldots) \\ & & & \updownarrow & & \\ (v'_1 = v_1 - 1, & v'_2 = v_2 - 1, & \ldots, & v'_h = 1, & v'_{h+1} = 2, & v'_{h+2} = v_{h+1}, \quad \ldots) \end{array} \tag{A3.23}$$

where *h* is the smallest index such that $v_h = 2$ or $v'_h = 1$, respectively.

Thus

$$\begin{aligned} \begin{Bmatrix} n \\ m \quad i \end{Bmatrix} = \begin{Bmatrix} n+i-1 \\ m-i \end{Bmatrix} &= \frac{(n+i-1)(n+m)^{(m-i-1)}}{(m-i)!} \\ &= \frac{\left(\frac{n+i-1}{2}\right)^{(m-i)} \left(\frac{n+i}{2}\right)^{(m-i)}}{(n+i)^{(m-i)}} \frac{4^{m-i}}{(m-i)!} \end{aligned} \tag{A3.24}$$

I assume $\left\| \widetilde{L} \right\|_{\mathrm{op}} < 1$ such that

$$\left(I - \widetilde{L}\right)^{-1} = \sum_{k=0}^{\infty} \widetilde{L}^k . \tag{A3.25}$$

Because cycles were assumed to be negligible

$$\widetilde{L}_d^k = \widetilde{L}_{j,\pi_d(j)}^k \tag{A3.26}$$

does neither depend on *j* nor on the choice of π_d. To calculate $\widetilde{L}_d^k$ I count paths of length *k* from *j* to $\pi_d(j)$ or—equivalently—formal products

$$\pi_d = \prod_{l=1}^{k} \Pi_{b_l} \qquad b_l \in \{1, \ldots, p\}. \tag{A3.27}$$

Denote by $P_p^{d+1,\frac{k-d}{2}}$ the set of all such paths/products. Similarly, denote by $P_p^{d+1,\frac{k-d}{2},i}$ the set of products that end in precisely *i* blocks $(\ ) \subset Bl_1 \subset \ldots \subset Bl_i$ of terms that cancel or—equivalently—the set of paths that hit $\pi_d(j)$ precisely $i+1$ times. Assigning to each vertex in a path $\in P_p^{d+1,\frac{k-d}{2}}$ one plus its graph-theoretical distance from $\pi_d(j)$ defines a map $P_p^{d+1,\frac{k-d}{2}} \to P_{\mathbf{N}}^{d+1,\frac{k-d}{2}}$ that restricts to maps $P_p^{d+1,\frac{k-d}{2},i} \to P_{\mathbf{N}}^{d+1,\frac{k-d}{2},i}$. It is easily verified that the preimage of a path $\in P_{\mathbf{N}}^{d+1,\frac{k-d}{2},i}$ has precisely $p^i(p-1)^{\frac{k-d}{2}-i}$ elements. Indeed, while steps towards $\pi_d(j)$ are unique each step away from $\pi_d(j)$ has $p-1$ potential targets unless it starts at $\pi_d(j)$ in which case there are p targets. Therefore

$$\widetilde{L}_d^k = \begin{cases} \left(\lambda\,{}_{\eta_x}M_0\right)^k \displaystyle\sum_{i=0}^{\frac{k-d}{2}} \begin{Bmatrix} d+1 \\ \frac{k-d}{2} \quad i \end{Bmatrix} p^i (p-1)^{\frac{k-d}{2}-i} & 2 \mid k-d \\ 0 & \text{else} \end{cases} \tag{A3.28}$$

where for the moment ${}_{\eta_x}M_0$ approximates the effect of thresholding. Other models might be better. Using (A&S15.1.13; ref[1]) and abbreviating

$$z = 4(p-1)\left(\lambda\,{}_{\eta_x}M_0\right)^2 \tag{A3.29}$$

this leads to

$$\begin{aligned}
\left(I-\widetilde{L}\right)_d^{-1} &= \sum_{k=0}^{\infty} \left(\lambda\,{}_{\eta_x}M_0\right)^{d+2k} \sum_{i=0}^{k} \begin{Bmatrix} d+1 \\ k \quad i \end{Bmatrix} p^i (p-1)^{k-i} \\
&= \left(\lambda\,{}_{\eta_x}M_0\right)^d \sum_{i=0}^{\infty} \left(\lambda\,{}_{\eta_x}M_0\right)^{2i} p^i \sum_{k=0}^{\infty} \begin{Bmatrix} d+i \\ k \end{Bmatrix} (p-1)^k \left(\lambda\,{}_{\eta_x}M_0\right)^{2k} \\
&= \left(\lambda\,{}_{\eta_x}M_0\right)^d \sum_{i=0}^{\infty} \left(\lambda\,{}_{\eta_x}M_0\right)^{2i} p^i\, {}_2F_1\!\left(\frac{d+i}{2}, \frac{d+i+1}{2}; d+i+1; z\right) \\
&= \left(\lambda\,{}_{\eta_x}M_0\right)^d \sum_{i=0}^{\infty} \left(\lambda\,{}_{\eta_x}M_0\right)^{2i} p^i \left(\frac{2}{1+\sqrt{1-z}}\right)^{d+i} = \frac{\left(\dfrac{2\lambda\,{}_{\eta_x}M_0}{1+\sqrt{1-z}}\right)^d}{1-\dfrac{2p\left(\lambda\,{}_{\eta_x}M_0\right)^2}{1+\sqrt{1-z}}} = \alpha\_B_{-}^{d}
\end{aligned} \tag{A3.30}$$

Here subscript *d* indicates any element $j, \pi_d(j)$. Note that the last expression confirms half of the heuristic constraint (2.5). Also note that comparing (A3.30) and (2.7) recovers (2.1,2.2) in the form

$$\left(I-\widetilde{L}\right)_0^{-1} = 1 + \lambda\,{}_{\eta_x}M_0 p\left(I-\widetilde{L}\right)_1^{-1} \tag{A3.31}$$

$$\left(I-\widetilde{L}\right)_d^{-1} = \lambda\,{}_{\eta_x}M_0\left[\left(I-\widetilde{L}\right)_{d-1}^{-1} + (p-1)\left(I-\widetilde{L}\right)_{d+1}^{-1}\right] \quad d > 0\,. \tag{A3.32}$$

Similarly, using

$$\frac{d}{dz}\left[\left(\frac{2}{1+\sqrt{1-z}}\right)^a\right] = \frac{a}{4\sqrt{1-z}}\left(\frac{2}{1+\sqrt{1-z}}\right)^{a+1} \tag{A3.33}$$

I calculate

$$\begin{aligned}
\left[{}^T\left(I-\widetilde{L}\right)^{-1}\left(I-\widetilde{L}\right)^{-1}\right]_d &= \sum_{k=0}^{\infty}(d+2k+1)\left(\lambda\,{}_{\eta_x}M_0\right)^{d+2k}\sum_{i=0}^{k}\left\{\begin{matrix} d+1 \\ k \quad i \end{matrix}\right\}p^i(p-1)^{k-i} \\
&= \left(\lambda\,{}_{\eta_x}M_0\right)^d\sum_{i=0}^{\infty}\left(\lambda\,{}_{\eta_x}M_0\right)^{2i}p^i\sum_{k=0}^{\infty}(d+2i+2k+1)\left\{\begin{matrix} d+i \\ k \end{matrix}\right\}(p-1)^k\left(\lambda\,{}_{\eta_x}M_0\right)^{2k} \\
&= \left(\lambda\,{}_{\eta_x}M_0\right)^d\sum_{i=0}^{\infty}\left(\lambda\,{}_{\eta_x}M_0\right)^{2i}p^i\left[(d+2i+1)\left(\frac{2}{1+\sqrt{1-z}}\right)^{d+i} + \frac{(d+i)z}{2\sqrt{1-z}}\left(\frac{2}{1+\sqrt{1-z}}\right)^{d+i+1}\right] \\
&= B_+^d\sum_{i=0}^{\infty}\left[1+\frac{d}{\sqrt{1-z}}+\left(1+\frac{1}{\sqrt{1-z}}\right)i\right]\left(\lambda\,{}_{\eta_x}M_0\right)^{2i}p^i\left(\frac{2}{1+\sqrt{1-z}}\right)^i \\
&= \left(1+\frac{d}{\sqrt{1-z}}\right)\alpha_-B_-^d + \left(1+\frac{1}{\sqrt{1-z}}\right)p\lambda\,{}_{\eta_x}M_0\alpha_-^2B_-^{d+1} = d\gamma_-B_-^d + \beta_-B_-^d
\end{aligned} \tag{A3.34}$$

This confirms the other half of constraint (2.5).

References

1. Abramowitz, M. & Stegun, I.A. *Handbook of mathematical functions with formulas, graphs, and mathematical tables*. (Dover publications: 1964).

Appendix A4

`ed.sniff` implementation notes

Contents

`ed.sniff` simulates pulse-coupled networks of linear leaky integrate-and-fire point-neurones. A limited set of quasi-asynchronous synaptic mechanisms is also implemented. `ed.sniff` is entirely event-driven and can therefore calculate spike times with high precision at moderate computational cost.

A4.0.1 Status

`ed.sniff` is as of now quite stable and generally useful. What is missing is more testing and more parameter sanity checks. Currently it is too easy for the user to self-harm without getting a meaningful error message. Also a couple of odd normalisations should be ironed out either by changing them or by providing a high-level Python wrapper.

`ed.sniff` was written in a clean but terse style adequate to the small set of features originally envisaged. It has since then mushroomed to put considerable strain on its ad hoc design and has become only just maintainable. Before pondering any further extensions `ed.sniff` should be refactored and modularised to make the complexity it has acquired more manageable.

A4.0.2 Prerequisites

All that will be needed is solving scalar linear ordinary differential equations. Thus, recall that the solution of

$$\frac{d}{dt}u(t) = S(t)u(t) + L(t) \tag{A4.1}$$

is

$$u(t_0 + \Delta t) = u(t_0)e^{\int_0^{\Delta t} S(t_0+v)dv} + \int_0^{\Delta t} L(t_0 + v)e^{\int_v^{\Delta t} S(t_0+w)dw} dv. \tag{A4.2}$$

Also recall that the "homogeneous" ($u(t_0) = 0$) solution is linear in L. We will need two special cases where $S(t) = -\tau$ is constant

(A4.3)

$$u(t_0 + \Delta t) = u(t_0)e^{-\tau\Delta t} + \frac{L_0}{\tau}\left[1 - e^{-\tau\Delta t}\right] \qquad L(t) = L_0$$

(A4.4)

$$u(t_0 + \Delta t) = u(t_0)e^{-\tau\Delta t} + \frac{L_0}{\tau' - \tau}\left[e^{-\tau\Delta t} - e^{-\tau'\Delta t}\right] \qquad L(t) = L_0 e^{-\tau'(t-t_0)}$$

Note that (A4.4) is only correct if $\tau' \neq \tau$; indeed

Warning 1. *"alpha-functions" are not currently implemented in* `ed.sniff`.

In the only other case we will encounter both, S and L, will be sums of exponentials

$$\begin{aligned} S(t_0 + \Delta t) &= S_0 + \sum_{\sigma\in\mathfrak{S}} S_\sigma(t_0)e^{-\tau_\sigma\Delta t} && \tau_\sigma > 0, S(t) \leq 0 \ \forall\ t \geq t_0 \\ L(t_0 + \Delta t) &= \sum_{\sigma'\in\mathfrak{L}} L_{\sigma'}(t_0)e^{-\tau'_{\sigma'}\Delta t} && \tau'_{\sigma'} > 0 \end{aligned} \tag{A4.5}$$

Abbreviating

$$b_\sigma := -\frac{S_\sigma(t_0)}{\tau_\sigma} \tag{A4.6}$$

$$f_{\sigma'} := \tau'_{\sigma'} + S_0 \tag{A4.7}$$

$$f_{\sigma,\sigma'} := \frac{f_{\sigma'}}{\tau_\sigma} \tag{A4.8}$$

the solution is

$$
\begin{aligned}
\text{(A4.9)}\quad u(t_0+\Delta t) &= u(t_0) e^{\Delta t S_0 + \sum\limits_{\sigma\in\mathfrak{S}} \frac{1-e^{-\tau_\sigma \Delta t}}{\tau_\sigma} S_\sigma(t_0)} \\
&\quad + \sum_{\sigma'\in\mathfrak{L}} L_{\sigma'}(t_0) \int\limits_0^{\Delta t} e^{-\tau'_{\sigma'} v + [\Delta t - v] S_0 + \sum\limits_{\sigma\in\mathfrak{S}} \frac{e^{-\tau_\sigma v} - e^{-\tau_\sigma \Delta t}}{\tau_\sigma} S_\sigma(t_0)} dv \\
&= e^{\Delta t S_0 + \sum\limits_{\sigma\in\mathfrak{S}} b_\sigma e^{-\tau_\sigma \Delta t}} \left[u(t_0) e^{-\sum\limits_{\sigma\in\mathfrak{S}} b_\sigma} + \sum_{\sigma'\in\mathfrak{L}} L_{\sigma'}(t_0) \int\limits_0^{\Delta t} e^{-f_{\sigma'} v - \sum\limits_{\sigma\in\mathfrak{S}} b_\sigma e^{-\tau_\sigma v}} dv \right] \\
&= e^{\Delta t S_0 + \sum\limits_{\sigma\in\mathfrak{S}} b_\sigma e^{-\tau_\sigma \Delta t}} \left[u(t_0) e^{-\sum\limits_{\sigma\in\mathfrak{S}} b_\sigma} + \sum_{\sigma'\in\mathfrak{L}} \frac{L_{\sigma'}(t_0)}{f_{\sigma'}} \int\limits_{e^{-f_{\sigma'}\Delta t}}^{1} e^{-\sum\limits_{\sigma\in\mathfrak{S}} b_\sigma y^{\frac{1}{f_{\sigma,\sigma'}}}} dy \right].
\end{aligned}
$$

`ed.sniff` calculates $u(t_0+\Delta t)$ by numerical quadrature using the line before the last line in (A4.9). Optionally (argument `transform_integral` in `Shunting_LIF` constructor) the last line can be used. This, however, appears to be never useful and will probably be removed.

In the special case

$$
\text{(A4.10)}\qquad S(t0+\Delta t) = S_0 + S_\sigma(t_0) e^{-\tau_\sigma \Delta t}
$$

(A4.9) reduces to

(A4.11)

$$
\begin{aligned}
u(t_0+\Delta t) &= e^{\Delta t S_0 + b_\sigma e^{-\tau_\sigma \Delta t}} \left[u(t_0) e^{-b_\sigma} + \sum_{\sigma'\in\mathfrak{L}} L_{\sigma'}(t_0) \int\limits_0^{\tau_\sigma \Delta t} \frac{e^{-f_{\sigma,\sigma'} v - b_\sigma e^{-v}}}{\tau_\sigma} dv \right] \\
&= e^{\Delta t S_0 + b_\sigma e^{-\tau_\sigma \Delta t}} \left[u(t_0) e^{-b_\sigma} + \sum_{\sigma'\in\mathfrak{L}} L_{\sigma'}(t_0) \int\limits_{b_\sigma e^{-\tau_\sigma \Delta t}}^{b_\sigma} y^{f_{\sigma,\sigma'}-1} e^{-y} dy \right] \\
&= e^{\Delta t S_0 + b_\sigma e^{-\tau_\sigma \Delta t}} \left[u(t_0) e^{-b_\sigma} + \sum_{\sigma'\in\mathfrak{L}} L_{\sigma'}(t_0) \left[\Gamma\left(f_{\sigma,\sigma'}, b_\sigma e^{-\tau_\sigma \Delta t}\right) - \Gamma\left(f_{\sigma,\sigma'}, b_\sigma\right) \right] \right]
\end{aligned}
$$

with $\Gamma(a,x) = \int_x^\infty e^{-v} v^{a-1} dv$ the (upper) incomplete gamma function. Since the GSL provides an implementation of the incomplete gamma function which is presumably faster than numerical quadrature (A4.10) is special-cased in `ed.sniff`.

Info 1. *Unfortunately the difference of incomplete gamma functions in (A4.10) is prone to loss of significance. Therefore if the relative difference*

$$
\text{(A4.12)}\qquad \left| \frac{\Gamma\left(f_{\sigma,\sigma'}, b_\sigma e^{-\tau_\sigma \Delta t}\right) - \Gamma\left(f_{\sigma,\sigma'}, b_\sigma\right)}{\Gamma\left(f_{\sigma,\sigma'}, b_\sigma e^{-\tau_\sigma \Delta t}\right) + \Gamma\left(f_{\sigma,\sigma'}, b_\sigma\right)} \right|
$$

falls below a preset value (argument `incomplete_gamma` *in* `Shunting_LIF` *constructor)* `ed.sniff` *falls back to numerical quadrature.*

A4.1 Mathematical model

A4.1.1 Neurones

`ed.sniff` uses the standard model of single-compartment linear leaky integrate-and-fire neurones, i.e. the state of a neurone is characterised by a single state variable u which is conveniently interpreted as the membrane potential. As long as the membrane potential is below a fixed threshold θ it evolves according to the equation

$$\frac{d}{dt}u(t) = -S_0 u(t) + I(t) \tag{A4.13}$$

Without loss of generality the resting potential of model neurones is zero. However, unlike other authors, we do not normalise out θ or the passive leak conductance S_0. The total synaptic current I may depend on u, see below. Whenever $u(t) = \theta$ an action potential is emitted, u immediately jumps to its reset potential u_r and is frozen for a refractory period $t_{\mathrm{refr}} \geq 0$.[1] Afterwards dynamics returns to equation (A4.13).

A4.1.2 Synapses

Info 2. *Since neurones in* `ed.sniff` *are single-compartment all incoming synapses of a given type are combined into a single object which, by abuse of language, will be called a synapse.*

Synapses σ in `ed.sniff` can be current- or conductance-based. Both types have an "observable" state variable g_σ and—possibly—additional "non-observable" state variables. The observable state of a current-based synapse is identical to the current it evokes. The observable state of a conductance-based synapse σ is its conductance S_σ. The corresponding synaptic current is then given by

$$I_\sigma(t) = [u_\sigma - u(t)]\, S_\sigma(t) \tag{A4.14}$$

where u_σ is the synapse's reversal potential.

Info 3. `ed.sniff` *special-cases purely shunting synapses ($u_\sigma = 0$). Indeed, conductance-based synapses are implemented as the sum of a purely shunting synapse and a current-based synapse with shared state variables.*[2]

Each of these types can either have monophasic (single exponential) or biphasic (difference of exponentials) dynamics.

Pulsed synapses

These are either monophasic

$$\frac{d}{dt}g_\sigma(t) = -\tau_\sigma g_\sigma(t) + \sum_{P\in\mathcal{P}} J_{P,\sigma} \sum_i \delta(t - t_{P,i} - \Delta_{P,\sigma}) \tag{A4.15}$$

---

[1] At the moment the membrane potential during refractoriness is irrelevant. This may, however, change should "graded synapses" ever be implemented for refractory neurones.

[2] To be entirely precise the states of the two synapses will typically differ by a constant factor.

or biphasic

$$\begin{aligned}\frac{d}{dt}g_\sigma(t) &= -\tau_\sigma g_\sigma(t) + g'_\sigma(t)\\ \frac{d}{dt}g'_\sigma(t) &= -\tau'_\sigma g'_\sigma(t) + \sum_{P\in\mathcal{P}} J_{P,\sigma}\sum_i \delta(t - t_{P,i} - \Delta_{P,\sigma})\end{aligned} \tag{A4.16}$$

Here g'_σ is the hidden state, $\tau_\sigma, \tau'_\sigma$ are the synaptic rates (reciprocal time constants), $\mathcal{P}$ is the set of presynaptic cells connected through σ, $\{t_{P,i}\}_i$ are the spike times of cell P and $\Delta_{P,\sigma}, J_{P,\sigma}$ are the corresponding synaptic delay and weight, respectively.

Warning 2. *To save a multiplication weights $\widetilde{J}_{P,\sigma}$ stored for biphasic synapses are interpreted by* `ed.sniff` *as $\widetilde{J}_{P,\sigma} = \frac{J_{P,\sigma}}{\tau'_\sigma - \tau_\sigma}$, cf. (A4.18) below. It is the user's responsibility to correct for that.* **In particular, τ_σ (argument `r_(shunt|full)_2` in `Shunting_LIF` constructor) must be smaller than τ'_σ (argument `r_(shunt|full)_1` in `Shunting_LIF` constructor)!** *In* `ed.sniff` *a biphasic current-based synapse will translate a presynaptic spike into the same total charge as a monophasic current-based synapse with the same τ_σ if the ratio of their stored weights is $\frac{\tau'_\sigma}{\tau'_\sigma - \tau_\sigma}$.*

Of course, in between spikes the solutions to (A4.15, A4.16) are

$$g_\sigma(t_0 + \Delta_t) = g_\sigma(t_0)e^{-\tau_\sigma \Delta t} \tag{A4.17}$$

and

$$\begin{aligned} g_\sigma(t_0 + \Delta_t) &= \left[g_\sigma(t_0) + \frac{g'_\sigma(t_0)}{\tau'_\sigma - \tau_\sigma}\right] e^{-\tau_\sigma \Delta t} - \frac{g'_\sigma(t_0)}{\tau'_\sigma - \tau_\sigma} e^{-\tau'_\sigma \Delta t}\\ g'_\sigma(t_0 + \Delta_t) &= g'_\sigma(t_0)e^{-\tau'_\sigma \Delta t}\end{aligned} \tag{A4.18}$$

respectively, cf. section A4.0.2.

Internally `ed.sniff` does not represent biphasic synpases using g_σ and g'_σ directly. The synaptic state is stored as $h_{1,\sigma} := g_\sigma + \frac{g'_\sigma}{\tau'_\sigma - \tau_\sigma}$ and $h_{2,\sigma} := -\frac{g'_\sigma}{\tau'_\sigma - \tau_\sigma}$. When a synaptic event arrives the corresponding stored weight $\widetilde{J}$ is instantly added to $h_{1,\sigma}$ and subtracted from $h_{2,\sigma}$. The rest of the time $h_{1,\sigma}$ and $h_{2,\sigma}$ decay exponentially with rates τ_σ and τ'_σ, respectively. Indeed,

Info 4. *Every synapse in* `ed.sniff` *is implemented as a set of state variables each of which decays exponentially with its own rate.*

Saturation. Optionally, pulsed synapses in `ed.sniff` support a simple model of synapse saturation. In this model the weight J of a synaptic event is replaced by a dampened weight $\widehat{J} := \frac{d_\sigma(t)J}{d_\sigma(t)+J}$ with

$$d_\sigma(t) := \begin{cases} g_{\max,\sigma} - g_\sigma(t) & \sigma \text{ monophasic} \\ g_{\max,\sigma} + h_{2,\sigma}(t) & \sigma \text{ biphasic}\end{cases} \tag{A4.19}$$

where $g_{\max,\sigma}$ is the saturation constant. Obviously, this model was chosen for computational economy, not biological plausibility.

Warning 3. *For a biphasic and a monophasic synapse with the same τ_σ to saturate at the same current the ratio of their saturation constants must equal $\frac{\tau_\sigma}{\tau'_\sigma - \tau_\sigma}$, cf. warning 2.*

A4.2 Event-driven integration scheme

The state of a neurone in `ed.sniff` is only updated when an event arrives. Broadly, events fall in two categories: External events (typically synaptic input) and self-events (e.g. the neurone's own spikes).

A4.2.1 External events

Whenever an external event arrives at a neurone and the neurone is not refractory its time stamp is replaced with the current time and all its state variables are updated according to their passive dynamics. If the event is synaptic it is accounted for by the receiving synapses[3]. If the neurone was predicted to fire a spike in the future, the corresponding pending event is removed from the scheduler. Based on the updated state a new prediction is made as to whether and when the neurone is expected to spike assuming no further external events. If a spike is predicted it is scheduled as a self-event and control is returned to the scheduler.

A4.2.2 Self-events

When a spiking self-event arrives the neurone's time stamp and synaptic state variables are updated and the membrane potential is reset. Synaptic events for all outgoing synapses are scheduled.

Info 5. *To unburden the scheduler and—more importantly—to accelerate postsynaptic processing of colocalised synapses synaptic events with the same delay are automatically grouped at the time the network is specified.*

If the refractory parameter of the neurone is positive the membrane potential is frozen and an unfreeze self-event is scheduled. Otherwise a new spiking prediction is made and if a spike is predicted to occur it is scheduled.

More events are described below.

A4.2.3 The scheduler

Event bookkeeping is handled by a scheduler which is organised as a block of time bins each of which contains an AVL tree. Unless events are distibuted very unevenly, using multiple bins helps keeping tree height, and thus access times, low. AVL trees are ordered balanced binary trees, i.e. elements can be inserted and removed in logarithmic time and the tree can be traversed *in order* in linear time. Of the latter property we only need that the first element can be identified in constant time. AVL trees are implemented in `ed.sniff` by means of a version of the pyavl library that was stripped down in the following way: To save some overhead leaves of AVL trees are not Python objects.

A4.3 State maintenace and spike prediction

Updating the synaptic state variables is simple and cheap. Each variable needs to be decreased exponentially according to the time passed since the last update.

---

[3] cf. info 5 below

To update the membrane potential an equation of type (A4.9) must be evaluated which is more expensive but still straightforward.

Info 6. *Cells with only one or no shunting conductances are special-cased, cf. (A4.11). For the latter case a specialised cell type* `Linear_LIF` *is also available. Only cells of type* `Linear_LIF` *can be presynaptic at graded and local synapses.*

Predicting spike times $u(t) = \theta$ is more involved. We will focus on neurones with shunting conductances.

A4.3.1 Coarse prediction

Fact 1. *The threshold θ can only be crossed from below if*

$$\frac{L(t)}{S(t)} \geq \theta. \tag{A4.20}$$

Therefore `ed.sniff` only performs a full (and expensive) spike prediction for times at which (A4.20) is predicted to be satisfied. To find these times all zeros of

$$r(t) := L(t) - \theta S(t) \tag{A4.21}$$

must be calculated. r being a linear combination of exponentials we can use

Fact 2. *A linear combination*

$$\sum_{i=1}^{N} g_i e^{-\tau_i t} \neq 0 \tag{A4.22}$$

of N exponentials has no more than $N - 1$ zeros

Proof. Without loss of generality one of the rates τ_i vanishes. Now, take the derivative and use induction. □

Similar to this proof `ed.sniff` uses derivatives to recursively find all future zeros. Neighbouring zeros of the derivative enclose at maximum one zero which is pinned down by bisection.

Remark 1. Taking advantage of the second derivative it should be possible to narrow down intervals where r changes sign, in such a way that they are either convex or concave. Then Newton's method could be safely used. This may be implemented in a future version of `ed.sniff`.

As for purely linear neurones: With those the membrane potential is itself a linear combination of exponentials, cf. (A4.4, A4.27). The above method applied directly to the membrane potential therefore suffices to predict the next spike.

A4.3.2 Actual prediction

Having obtained all future time intervals where (A4.20) holds, starting from the left `ed.sniff` determines whether one of them contains a threshold crossing $u(t) = \theta$. Using (A4.1) calculating the derivative is cheap. Therefore Newton's method is used.

Info 7. *If a spike happens to fall on or near the right interval boundary Newton's method may not be very efficient. It may be worthwhile to special-case this, but currently* `ed.sniff` *does not.*

This is safe because there is at most one threshold crossing in each interval. Therefore Newton's method can overshoot—in which case `ed.sniff` falls back to bisection—but it cannot overlook a spike.

Info 8. *Because most predicted spikes will be invalidated by intermittent synaptic events* `ed.sniff` *schedules a self-event to suspend Newton's algorithm as soon as the current guess lies more than a given delay ahead (argument* `granularity` *in* `Shunting_LIF` *constructor). This delay defaults to zero such that spike prediction is suspended after each iteration.*

A4.4 Further concepts

A4.4.1 Graded synapses

In `ed.sniff` a graded synapse is a synapse whose input is not derived from presynatic APs but from a presynaptic voltage-dependent quantity v_μ. Monophasic

$$\frac{d}{dt}g_\sigma(t) = -\tau_\sigma g_\sigma(t) + \sum_{\mu\in\mathcal{M}} J_{\mu,\sigma} v_\mu(t-\Delta_{\mu,\sigma}) \tag{A4.23}$$

and biphasic

$$\begin{aligned}\frac{d}{dt}g_\sigma(t) &= -\tau_\sigma g_\sigma(t) + g'_\sigma(t)\\ \frac{d}{dt}g'_\sigma(t) &= -\tau'_\sigma g'_\sigma(t) + \sum_{\mu\in\mathcal{M}} J_{\mu,\sigma} v_\mu(t-\Delta_{\mu,\sigma})\end{aligned} \tag{A4.24}$$

graded synapses are available. The state v_μ itself depends on the presynaptic membrane potential u_P either monophasically

$$\frac{d}{dt}v_\mu(t) = -\tau_\mu v_\mu(t) + u_P(t) \tag{A4.25}$$

or biphasically

$$\begin{aligned}\frac{d}{dt}v_\mu(t) &= -\tau_\mu v_\mu(t) + v'_\mu(t)\\ \frac{d}{dt}v'_\mu(t) &= -\tau'_\mu v'_\mu(t) + u_P(t)\end{aligned} \tag{A4.26}$$

For this mechanism to be compatible with the event-driven architecture of `ed.sniff` the presynaptic cell is required to be purely linear, i.e. to have only current-based synapses. To enforce this

Info 9. *Only neurones of type* `Linear_LIF` *are allowed to be donors of graded synapses in* `ed.sniff`*.*

As between events the membrane potential u_P of a purely linear neurone can be written as a sum of exponentials

$$u_P(t_0+\Delta t)=\sum_{i=1}^{N_P} h_{P,i}(t_0)e^{-\tau_{P,i}\Delta t}, \tag{A4.27}$$

cf. (A4.4), the same is true for the voltage-dependent variables

$$v_\mu(t_0+\Delta t)=\sum_{i=1}^{N_\mu} h_{\mu,i}(t_0)e^{-\tau_{\mu,i}\Delta t} \qquad \tau_{\mu,i}=\tau_{P,i}\ \forall\ i\in\{1,\dots,N_P\} \tag{A4.28}$$

and the observable state of the graded synapse

$$g_\sigma(t_0+\Delta t)=\sum_{i=1}^{N_\sigma} h_{\sigma,i}(t_0)e^{-\tau_{\sigma,i}\Delta t} \qquad \tau_{\sigma,i}=\tau_{\mu,i}\ \forall\ i\in\{1,\dots,N_\mu\}. \tag{A4.29}$$

The state variables $h_{\star,i}$ are partly redundant and relate as follows

(A4.30)

$$h_{\mu,i}=\begin{cases}
-\frac{h_{P,i}}{\tau_{P,i}-\tau_{\mu,N_\mu}} & v_\mu \text{ monophasic}, i\in\{1,\dots,N_P\}\\
v_\mu+\sum\limits_{i=1}^{N_P}\frac{h_{P,i}}{\tau_{P,i}-\tau_{\mu,N_\mu}} & v_\mu \text{ monophasic}, i=N_\mu\\
\frac{h_{P,i}}{\left(\tau_{P,i}-\tau_{\mu,N_\mu}\right)\left(\tau_{P,i}-\tau_{\mu,N_\mu-1}\right)} & v_\mu \text{ biphasic}, i\in\{1,\dots,N_P\}\\
-\frac{v'_\mu}{\tau_{\mu,N_\mu-1}-\tau_{\mu,N_\mu}} & \\
\quad-\sum\limits_{i=1}^{N_P}\frac{h_{P,i}}{\left(\tau_{\mu,N_\mu-1}-\tau_{\mu,N_\mu}\right)\left(\tau_{P,i}-\tau_{\mu,N_\mu-1}\right)} & v_\mu \text{ biphasic}, i=N_\mu-1\\
v_\mu+\frac{v'_\mu}{\tau_{\mu,N_\mu-1}-\tau_{\mu,N_\mu}} & \\
\quad+\sum\limits_{i=1}^{N_P}\frac{h_{P,i}}{\left(\tau_{\mu,N_\mu-1}-\tau_{\mu,N_\mu}\right)\left(\tau_{P,i}-\tau_{\mu,N_\mu}\right)} & v_\mu \text{ biphasic}, i=N_\mu
\end{cases}$$

and, analogously,

(A4.31)

$$\frac{h_{\sigma,i}}{J_\sigma}=\begin{cases}
-\frac{h_{\mu,i}}{\tau_{\mu,i}-\tau_{\sigma,N_\sigma}} & g_\sigma \text{ monophasic}, i\in\{1,\dots,N_\mu\}\\
\frac{g_\sigma}{J_\sigma}+\sum\limits_{i=1}^{N_\mu}\frac{h_{\mu,i}}{\tau_{\mu,i}-\tau_{\sigma,N_\sigma}} & g_\sigma \text{ monophasic}, i=N_\sigma\\
\frac{h_{\mu,i}}{(\tau_{\mu,i}-\tau_{\sigma,N_\sigma})(\tau_{\mu,i}-\tau_{\sigma,N_\sigma-1})} & g_\sigma \text{ biphasic}, i\in\{1,\dots,N_\mu\}\\
-\frac{g'_\sigma}{J_\sigma(\tau_{\sigma,N_\sigma-1}-\tau_{\sigma,N_\sigma})} & \\
\quad-\sum\limits_{i=1}^{N_\mu}\frac{h_{\mu,i}}{(\tau_{\sigma,N_\sigma-1}-\tau_{\sigma,N_\sigma})(\tau_{\mu,i}-\tau_{\sigma,N_\sigma-1})} & g_\sigma \text{ biphasic}, i=N_\sigma-1\\
\frac{g_\sigma}{J_\sigma}+\frac{g'_\sigma}{J_\sigma(\tau_{\sigma,N_\sigma-1}-\tau_{\sigma,N_\sigma})} & \\
\quad+\sum\limits_{i=1}^{N_\mu}\frac{h_{\mu,i}}{(\tau_{\sigma,N_\sigma-1}-\tau_{\sigma,N_\sigma})(\tau_{\mu,i}-\tau_{\sigma,N_\sigma})} & g_\sigma \text{ biphasic}, i=N_\sigma
\end{cases}$$

Warning 4. *For no good reason biphasic, but not monophasic, voltage mechanisms and graded synapses are not represented by the $h_{\star,i}$ in* `ed.sniff` *but by $\left[\tau_{\star,N_\star-1}-\tau_{\star,N_\star}\right]h_{\star,i}$. The user must adapt synaptic weights accordingly.*

Info 10. *In* `ed.sniff` *the presynaptic mechanisms of a given type of graded synapse (cf. info 2) must be compatible, i.e. they must have the same set of rates* $\{\tau_{\mu,i}\}_i$ *in (A4.28).*

Warning 5. *As the state of a graded synapse depends on the presynaptic voltage* all *events of the presynaptic cell must be forwarded to and processed by the postsynaptic cell. Therefore graded synapses can considerably slow down* `ed.sniff`*.*

Update rules

By way of example we partly spell out the update rules in the case of a biphasic presynaptic mechanism ($N_\mu = N_P + 2$) and a monophasic synapse ($N_\sigma = N_\mu + 1$).

Passive update. Before any event is handled all state variables are brought up-to-date by the simple rule

$$h_{\star,i} \mapsto h_{\star,i} e^{-\tau_{\star,i}\Delta t} \tag{A4.32}$$

where Δt is the difference between the event time and the old time stamp.

Presynaptic AP. Assume that the passive leak of P is the last term in the sum in (A4.27). Only this term will jump in the membrane potential:

$$h_{P,N_P} \mapsto h_{P,N_P} - \theta + u_r \tag{A4.33}$$

(A4.30, A4.31) dictate the corresponding changes in the voltage-mechanism

$$\begin{aligned}
h_{\mu,N_P} &\mapsto h_{\mu,N_P} - \frac{\theta - u_r}{\left(\tau_{P,N_P} - \tau_{\mu,N_\mu}\right)\left(\tau_{P,N_P} - \tau_{\mu,N_\mu-1}\right)} \\
h_{\mu,N_\mu-1} &\mapsto h_{\mu,N_\mu-1} + \frac{\theta - u_r}{\left(\tau_{\mu,N_\mu-1} - \tau_{\mu,N_\mu}\right)\left(\tau_{P,N_P} - \tau_{\mu,N_\mu-1}\right)} \\
h_{\mu,N_\mu} &\mapsto h_{\mu,N_\mu} - \frac{\theta - u_r}{\left(\tau_{\mu,N_\mu-1} - \tau_{\mu,N_\mu}\right)\left(\tau_{P,N_P} - \tau_{\mu,N_\mu}\right)}
\end{aligned} \tag{A4.34}$$

and the post-synapse
(A4.35)

$$\begin{aligned}
h_{\sigma,N_P} &\mapsto h_{\sigma,N_P} + \frac{J_\sigma(\theta - u_r)}{\left(\tau_{P,N_P} - \tau_{\sigma,N_\sigma}\right)\left(\tau_{P,N_P} - \tau_{\mu,N_\mu}\right)\left(\tau_{P,N_P} - \tau_{\mu,N_\mu-1}\right)} \\
h_{\sigma,N_\mu-1} &\mapsto h_{\sigma,N_\mu-1} - \frac{J_\sigma(\theta - u_r)}{\left(\tau_{\mu,N_\mu-1} - \tau_{\sigma,N_\sigma}\right)\left(\tau_{\mu,N_\mu-1} - \tau_{\mu,N_\mu}\right)\left(\tau_{P,N_P} - \tau_{\mu,N_\mu-1}\right)} \\
h_{\sigma,N_\mu} &\mapsto h_{\sigma,N_\mu} + \frac{J_\sigma(\theta - u_r)}{\left(\tau_{\mu,N_\mu} - \tau_{\sigma,N_\sigma}\right)\left(\tau_{\mu,N_\mu-1} - \tau_{\mu,N_\mu}\right)\left(\tau_{P,N_P} - \tau_{\mu,N_\mu}\right)} \\
h_{\sigma,N_\sigma} &\mapsto h_{\sigma,N_\sigma} - \frac{J_\sigma(\theta - u_r)}{\left(\tau_{\mu,N_\mu} - \tau_{\sigma,N_\sigma}\right)\left(\tau_{\mu,N_\mu-1} - \tau_{\sigma,N_\sigma}\right)\left(\tau_{P,N_P} - \tau_{\sigma,N_\sigma}\right)}
\end{aligned}$$

respectively.

Synaptic event. The presynaptic cell can only receive pulsed synapses. Assume an event of weight $J_{\sigma'}$ occurs at a synapse σ' and let σ' be e.g. biphasic. Let the $k-1^{\text{st}}$ and k^{th} term in the sum in (A4.27) correspond to its hidden and observable state variables, respectively. The membrane potential will then[4] experience the following changes:

$$\begin{aligned} h_{P,k-1} &\mapsto h_{P,k-1} - \frac{J_{\sigma'}}{\left(\tau_{P,k-1} - \tau_{P,N_P}\right)\left(\tau_{P,k-1} - \tau_{P,k}\right)} \\ h_{P,k} &\mapsto h_{P,k} + \frac{J_{\sigma'}}{\left(\tau_{P,k} - \tau_{P,N_P}\right)\left(\tau_{P,k-1} - \tau_{P,k}\right)} \\ h_{P,N_P} &\mapsto h_{P,N_P} - \frac{J_{\sigma'}}{\left(\tau_{P,k} - \tau_{P,N_P}\right)\left(\tau_{P,k-1} - \tau_{P,N_P}\right)} \end{aligned} \tag{A4.36}$$

As above this translates into rules for the voltage mechanism and the post-synapse by (A4.30, A4.31). However, the details—being straightforward as well as cumbersome—are omitted here.

A4.4.2 Local synpases

Local synapses in `ed.sniff` are very similar to graded synapses. The only difference is that the presynaptic mechanism of a local synapse is based on the state of one synapse terminating on the donor rather than the donor's membrane potential.

A4.5 Input and Output

A4.5.1 Poisson spikers

External input to `ed.sniff` networks is generated exclusively by `Spiker` instances. These are Poisson spikers with time-varying firing intensity.

Let $p(t)$ be the instantaneous firing density. Then the survival rate since t_0 is

$$s(t) = e^{-\int_{t_0}^{t} p(v)dv} \tag{A4.37}$$

A Poisson process with instantaneous firing density $p(t)$ can thus be simulated by drawing ξ from the uniform distribution on the unit interval and then solving

$$\ln \xi = -\int_{t_0}^{t} p(v)dv \tag{A4.38}$$

for the next spike time t.

`ed.sniff` implements the following functional forms of the firing intensity

$$p_n(t) = 0 \qquad \text{"nop"} \tag{A4.39}$$

$$p_f(t) = \begin{cases} 0 & t < t_{\text{last spike}} + t_{\text{refr}} \\ \tau & \text{else} \end{cases} \qquad \text{"fixed"} \tag{A4.40}$$

$$p_{pt}(t) = o + \widetilde{r}\left[p + (1-p)e^{-\tau_s t} - e^{-\tau_f t}\right] \qquad \text{"phasic-tonic"} \tag{A4.41}$$

$$p_o(t) = \left[o + a\cos\frac{t+\phi}{2\pi\omega}\right]_+ \qquad \text{"oscillatory"} \tag{A4.42}$$

---

[4] That is the theory; in practice warning 2 applies.

In (A4.40) $\widetilde{r}$ either equals $\frac{r}{p}$ (flag normalise not set) or $\frac{r}{p+(1-p)e^{-\tau_s t_{\max}}-e^{-\tau_f t_{\max}}}$ (flag normalise set) with $t_{\max} := \frac{\ln(1-p)+\ln\tau_s-\ln\tau_f}{\tau_s-\tau_f}$. Consecutive "epochs" each with any one of these functional forms can be pieced together. In the case of phasic-tonic and oscillatory spikers (A4.38) is solved using Newton's method.

A4.5.2 Event loggers

To record an `ed.sniff` simulation an instance of one of the two event logger classes `Write_All` and `Store_All` must be passed to the `process_event` method of the scheduler. The former will write events chronologically to a file, the latter will group them by receiving cell and store them in memory in a Python dictionary. Both provide limited support for event filtering. The `Store_All` class offers three event tallying methods:

1. recording events
2. counting events
3. making a phase histogram, assuming periodic firing rate modulation

A4.6 Miscellaneous implementation details

Synapse id's are integers based at `FIRST_SYN` in the follwing order

1. pulsed purely shunting monophasic,
2. graded/local purely shunting monophasic,
3. pulsed purely shunting biphasic,
4. graded/local purely shunting biphasic,
5. pulsed conductance-based monophasic,
6. graded/local conductance-based monophasic,
7. pulsed conductance-based biphasic,
8. graded/local conductance-based biphasic,
9. pulsed current-based monophasic,
10. graded/local current-based monophasic,
11. pulsed current-based biphasic,
12. graded/local current-based biphasic.

Synaptic rates are stored as negative numbers, the `(Linear|Shunting)_LIF` constructor flips the sign.

Graded and local synapses do not implement their postsynaptic part. They rather tap into an existing pulsed synapse which is specified as the second element of argument `gr_(shunt|full|lin)[_bi]` to the `Shunting_LIF` constructor.

Graded and local synapses can currently only terminate on cells of type `Shunting_LIF`. Lifting this restriction would in principle be possible but involve quite some work.

Graded synapses currently have a hard complexity limit (module constant `MAX_WEIGHT_GROUP`). This caps the number N_μ of state variables in (A4.28). The limit can be extended at compile time by changing `MAX_WEIGHT_GROUP` in the C source.

Graded and local synapses cannot currently handle refractory donors.

Event groups arise from automatic grouping of outgoing synapses by delay and target cell at the time the network is specified (method `set[_(graded |local)]_synapses` of `Cell` object). This optimisation reduces the number of scheduled events and avoids multiple state updates triggered by simultaneously arriving events. On the downside event loggers cannot currently resolve event groups which makes simulation logs less straightforward to read.

Appendix A5

`ed.sniff` class reference

`ed.sniff`: an event-driven simulator of networks of integrate-and-fire neurones

class `Cell` `()`

Cell (cell_type, id, spiking_rules, scheduler, g_full=NULL, g_shunt=NULL, g_lin=NULL, g_full_1=NULL, g_shunt_1=NULL, g_lin_1=NULL, g_full_2=NULL, g_shunt_2=NULL, g_lin_2=NULL, u=0.0, t=0.0)

Cell object.

Parameters

cell_type [`Linear_LIF` or `Shunting_LIF` or `Spiker`] **Note: constructor signature depends on cell type type**

id [str] cell identifier

spiking_rules [iterable] only if cell_type is `Spiker`; dicts describing consecutive "epochs"; see `Spiker` for details

scheduler [`Scheduler`] only if cell_type is `Spiker`; the scheduler to hook up with; the first spike is calculated and scheduled immediately; this still leaves time to create synapses

g_lin [iterable] only if cell_type is `Shunting_LIF` or `Linear_LIF`; initial conductances of linear ("current-based") synapses

g_lin_1 [iterable] only if cell_type is `Shunting_LIF` or `Linear_LIF`; initial values of first state variables of linear ("current-based") synapses

g_lin_2 [iterable] only if cell_type is `Shunting_LIF` or `Linear_LIF`; initial values of first state variables of linear ("current-based") synapses

g_full [iterable] only if cell_type is `Shunting_LIF`; initial conductances of full conductance-based synapses

g_full_1 [iterable] only if cell_type is `Shunting_LIF`; initial values of first state variables of full conductance-based synapses

g_full_2 [iterable] only if cell_type is `Shunting_LIF`; initial values of first state variables of full conductance-based synapses

g_shunt [iterable] only if cell_type is `Shunting_LIF`; initial conductances of purely shunting (reversal potential = resting potential) synapses

g_shunt_1 [iterable] only if cell_type is `Shunting_LIF`; initial values of first state variables of purely shunting (reversal potential = resting potential) synapses

g_shunt_2 [iterable] only if cell_type is `Shunting_LIF`; initial values of first state variables of purely shunting (reversal potential = resting potential) synapses

u [float] only if cell_type is `Shunting_LIF` or `Linear_LIF`; initial membrane potential

t [float] initial time; must not be in the future

`detach_synapses`

detach_synapses()

Remove all (pulsed | graded | local) outgoing synapses.

Returns None

`identifier`

the cell's identifier string

`set_graded_synapses`

set_graded_synapses (params)

Set outgoing graded synapses.

Parameters

params [ndarray of dtype `synapse_descriptor`] the synapse record

Returns None

The presynaptic (this) `Cell` must be of type `Linear_LIF`.

Each individual synapse is specified by a `synapse_descriptor` with the following fields:

delay [float] time difference between presynaptic AP and postsynaptic event

target [object] the postsynaptic `Cell`

type [int] the synapse type; this is the index into the synapse table of the target cell type plus an offset of `FIRST_SYN`

weight [float] the synaptic strength

Matching presynaptic voltage-mechanisms are found automatically. An exception is raised if there is none.

`set_local_synapses`

set_local_synapses (synapse_no, params)

Set outgoing local synapses.

Parameters

synapse_no [int] *presynaptic* synapse type based at `FIRST_SYN`

params [ndarray of dtype `synapse_descriptor`] the synapse record

Returns None

The presynaptic (this) `Cell` must be of type `Linear_LIF`.

Each individual synapse is specified by a `synapse_descriptor` with the following fields:

delay [float] time difference between presynaptic AP and postsynaptic event

target [object] the postsynaptic `Cell`

type [int] the synapse type; this is the index into the synapse table of the target cell type plus an offset of `FIRST_SYN`

weight [float] the synaptic strength

Matching local mechanisms of the donor synapse are found automatically. An exception is raised if there is none.

`set_synapses`

set_synapses (params)

Set outgoing pulsed synapses.

Parameters

params [ndarray of dtype `synapse_descriptor`] the synapse record

Returns None

Each individual synapse is specified by a `synapse_descriptor` with the following fields:

delay [float] time difference between presynaptic AP and postsynaptic event

target [object] the postsynaptic `Cell`

type [int] the synapse type; this is the index into the synapse table of the target cell type plus an offset of `FIRST_SYN`

weight [float] the synaptic strength

class `Linear_LIF`()

Linear_LIF (g_leak, r_lin=NULL, r_lin_1=NULL, r_lin_2=NULL, r_vm=NULL, r_vm_1=NULL, r_vm_2=NULL, sat_lin=NULL, sat_lin_bi local=NULL, u_reset=0.0, u_thresh=1.0, t_refr=0.0)

Linear leaky integrate-and-fire neurone type with linear synapses.

Use a `Linear_LIF` instance as first argument to the `Cell` constructor to create cells of this type.

Parameters

- **g_leak** [float] passive leak conductance
- **r_lin** [iterable] decay rates of monophasic synapses
- **r_lin_1** [iterable] decay rates of hidden state variables of biphasic synapses
- **r_lin_2** [iterable] decay rates of observable state variables of biphasic synapses
- **r_vm** [iterable] decay rates of monophasic voltage mechanisms
- **r_vm_1** [iterable] decay rates of hidden state variables of biphasic voltage mechanisms
- **r_vm_2** [iterable] decay rates of observable state variables of biphasic voltage mechanisms
- **sat_lin** [iterable] saturation constants of monophasic synapses
- **sat_lin_bi** [iterable] saturation constants of biphasic synapses
- **local** [iterable] specification dicts, one for each synapse
- **u_reset** [float] reset potential
- **u_thresh** [float] firing threshold; must be positive and greater *u_reset*
- **t_refr** [float] refractory period

Synapse-local mechanisms are specified as dicts with the following (optional) keys:

- **r_lm** [iterable] decay rates of monophasic mechanisms
- **r_lm_1** [iterable] decay rates of hidden state variables of biphasic mechanisms
- **r_lm_2** [iterable] decay rates of observable state variables of biphasic mechanisms

Synapses without local mechanisms can be indicated by *False* or *None* or an empty dict.

class `Scheduler()`

Scheduler(no_bins, cycle_time)

Scheduler object

Parameters

- **no_bins** [int] number of time bins, two at least; larger numbers speed up the scheduler as long as typical time bins contain at least one event
- **cycle_time** [float] time horizon of the scheduler; predicted events should not lie further in the future

Uses AVL trees to store future events.

`process_event`

process_event(output=NULL, steps=1)

Retrieve and processes one or more events from the scheduler

Parameters

- **output** [`Store_All` or `Write_All`] event logger; required to retrieve simulation output
- **steps** [int] maxmimum number of events to process; if network activity ceases earlier this is handled gracefully

Returns n, t

n [int] number of events processed

t [double] current simulation time

`to_recarray`

to_recarray()

Return all scheduled events and bin sizess.

This is mostly useful for introspection and debugging.

Returns (events, bin_counts)

events [ndarray of dtype `synapse_descriptor`] all scheduled events in chronological order; value stored in field delay is absolute time; field weight is only valid for individual pulsed synaptic events

bin_counts [ndarray] number of events in each scheduler bin

class `Shunting_LIF`()

Shunting_LIF (g_leak, r_shunt=NULL, r_full=NULL, r_lin=NULL, E_full=NULL, sat_shunt=NULL, sat_full=NULL, sat_lin=NULL, r_shunt_1=NULL, r_full_1=NULL, r_lin_1=NULL, E_full_bi=NULL, sat_shunt_bi=NULL, sat_full_bi=NULL, sat_lin_bi=NULL, r_shunt_2=NULL, r_full_2=NULL, r_lin_2=NULL, gr_shunt=NULL, gr_full=NULL, gr_lin=NULL, gr_shunt_bi=NULL, gr_full_bi=NULL, gr_lin_bi=NULL, u_reset=0.0, u_thresh=1.0, t_refr=0.0, granularity=0.0, transform_integral=False, incomplete_gamma=0.001)

Linear leaky integrate-and-fire neurone type with full synapses.

Use a `Shunting_LIF` instance as first argument to the `Cell` constructor to create cells of this type.

Parameters

g_leak [float] passive leak conductance

r_shunt [iterable] decay rates of monophasic purely shunting synapses

r_full [iterable] decay rates of monophasic conductance-based synapses

r_lin [iterable] decay rates of monophasic current-based synapses

E_full [iterable] reversal potentials of monophasic conductance-based synapses

sat_shunt [iterable] saturation constants of monophasic purely shunting synapses

sat_full [iterable] saturation constants of monophasic conductance-based synapses

sat_lin [iterable] saturation constants of monophasic current-based synapses

r_shunt_1 [iterable] decay rates of hidden state variables of biphasic purely shunting synapses **Important: must be larger than r_shunt_2!**

r_full_1 [iterable] decay rates of hidden state variables of biphasic conductance-based synapses **Important: must be larger than r_full_2!**

r_lin_1 [iterable] decay rates of hidden state variables of biphasic current-based synapses

E_full_bi [iterable] reversal potentials of biphasic conductance-based synapses

sat_shunt_bi [iterable] saturation constants of biphasic purely shunting synapses

sat_full_bi [iterable] saturation constants of biphasic conductance-based synapses

sat_lin_bi [iterable] saturation constants of biphasic current-based synapses

r_shunt_2 [iterable] decay rates of observable state variables of biphasic purely shunting synapses **Important: must be smaller than r_shunt_1!**

r_full_2 [iterable] decay rates of observable state variables of biphasic conductance-based synapses **Important: must be smaller than r_full_1!**

r_lin_2 [iterable] decay rates of observable state variables of biphasic current-based synapses

gr_shunt [3-tuple of iterables (rates, targets, sizes)] specification of monophasic graded purely shunting synapses

gr_full [3-tuple of iterables (rates, targets, sizes)] specification of monophasic graded conductance-based synapses

gr_lin [3-tuple of iterables (rates, targets, sizes)] specification of monophasic graded current-based synapses

gr_shunt_bi [3-tuple of iterables (rates, targets, sizes)] specification of biphasic graded purely shunting synapses

gr_full_bi [3-tuple of iterables (rates, targets, sizes)] specification of biphasic graded conductance-based synapses

gr_lin_bi [3-tuple of iterables (rates, targets, sizes)] specification of biphasic graded current-based synapses

u_reset [float] reset potential

u_thresh [float] firing threshold; must be positive and greater u_reset

t_refr [float] refractory period

granularity [float] the spike predictor is suspended as soon its best guess lies more than this parameter in the future

transform_integral [bool] **do not use!**

incomplete_gamma [float] threshold below which to assume loss of significance in relative difference of incomplete gamma functions

Each family of graded synapse is specified by three parameters:

rates [iterable] the decay rates of the presynaptic voltage mechanisms as a flat sequence

targets [iterable] the indices (based at `FIRST_SYN`) of the target synapses; these must be in the matching family

sizes [iterable] the sizes of the presynaptic voltage mechanisms; these must sum to the length of rates

class **`Spike_Counter`**`()`

Spike_Counter (ignore_before=0.0, ignore_after=inf)

For use with `Store_All` objects; counts events.

Despite the class name all kinds of events are counted.

Parameters

ignore_before [float] point in time to start counting from

ignore_after [float] point in time to cease counting after

`count`

count ()

Return the current count.

Returns

n [int] number of events recorded so far class **`Spike_Histogram`**`()`

Spike_Histogram (ignore_before, ignore_after, cycle, no_bins)

For use with `Store_All` objects; make phase histogram.

Events are binned according to time modulo cycle. Despite the class name all kinds of events are counted.

Parameters

ignore_before [float] point in time to start counting from

ignore_after [float] point in time to cease counting after

cycle [float] cycle time

no_bins [int] number of histogram bins to use; two at least

`counts`

current histogram bin counts (read only)

`frequencies`

frequencies (time)

Return normalised histogram in units of 1/time.

Parameters

time [double] current simulation time; the instance does not now itself! Must be later than ignore_before and will be replaced by ignore_after if it is later than that, cf. `Spike_Histogram` constructor

class **`Spiker`**`()`

Spiker (seed=0)

Poisson spiker with time-varying firing intensity.

Use a `Spiker` instance as first argument to the `Cell` constructor to create cells of this type.

Parameters

seed [int] for random number generator

The firing rate envelope of a spiker must be passed to the `Cell` constructor as argument spiking_rules as an iterable returning consecutive “epoch” descriptors. Epoch descriptors are 3-tuples (type, dt, params) with:

type [str] functional form of the envelope for the epoch; see below for legal values

dt [float] epoch duration

params [dict] parameters for envelope function

The following functional forms taking the indicated parameters are supported

“nop” ()

no spikes

“fixed” (tau, t_refr=0.0)

tau [float] firing rate not accounting for refractoriness

t_refr [float] absolute refractory period

fixed firing rate

“phasic-tonic” (

tau_fast, tau_slow, r=1.0, plateau=0.0, offset=0.0, normalise=1, ytol=1e-8)

tau_fast [float] faster exponential rate

tau_slow [float] slower exponential rate

r [float] target firing rate excluding offset; also see normalise

plateau [float] steady-state level relative to dynamic range; 0 <= plateau < 1

offset [float] fixed firing rate offset; must be nonnegative

normalise [int] whether to normalise steady-state (normalise=0) or maximal (normalise=1) firing rate to r

ytol [float] tolerance for Newton's method

modified difference of exponential accomodating a non-zero steady-state firing rate

"oscillatory" (

frequency, phase=0.0, offset=1.0, amplitude=1.0, ytol=1e-8)

frequency [float] oscillation frequency

phase [float] in units of cycles; phase=0 gives a cosine, phase=-1/4 a sine

offset [float] fixed firing rate offset; must be >= -amplitude

amplitude [float] oscillation amplitude

ytol [float] tolerance for Newton's method

oscillating firing rate

class **`Store_All`**`()`

Store_All (filter, recorder, event_dict=NULL, cell_watcher_args=NULL, cell_watcher_kwds=NULL, format=NULL)

Event logger writing to a dict with keys the `Cell` id's.

Events are therefore grouped by receiving `Cell` before they are tallied.

Parameters

filter [str] what kind of events to record

recorder [str] how to record events

event_dict [dict] the dict to record to; if not passed a new one will be created

cell_watcher_args [tuple] only needed if recorder is "count" or "histogram"

cell_watcher_kwds [dict] only needed if recorder is "count" or "histogram"

format [str] only needed if recorder is "list"

Filter can be one of

"all" : do not filter

"APs" : only record spikes

"no input" : ignore `Spiker` cells

"APs no input" : only record spikes not originating from `Spiker` cells

"APs no input but R" : only record spikes not originating from `Spiker` cells whose id does not start with "R"

Recorder can be one of

"list" : create a list for each `Cell`; requires format argument

"count" : create a `Spike_Counter` for each `Cell` passing cell_watcher_args and cell_watcher_kwds as args and kwds to the constructor

"histogram" : create a `Spike_Histogram` for each `Cell` passing cell_watcher_args and cell_watcher_kwds as args and kwds to the constructor

Format can be one of

"full" : for each event record a tuple (time, event type) if it is an event group and a tuple (time, event type, weight) if it is a single event. **Warning:** if the event is graded synaptic or local synaptic the weight will be gibberish!

"time" : only record event times

`log`

the dictionary of events recorded

class **`Write_All`**`()`

Write_All (file_name, filter)

Event logger writing to a file.

Writes one line with time, cell id, event code and weight per event. If the event is a group of events the weight will be omitted. If the event is graded weight will be gibberish. Destroy object to flush buffer.

Parameters

file_name [str] name of log file; file will be opened in append mode

filter [str] what kind of events to record

Filter can be one of

"all" : do not filter

"APs" : only record spikes

"no input" : ignore `Spiker` cells

"APs no input" : only record spikes not originating from `Spiker` cells

`classify_spikes``()`

classify_spikes(trains, lfp, dt, ang_disp, ang_dev, lfp_criterion, lower=0.0, use_last_lfp_sample=0, axis=-1)

Currently dysfunctional!

Separate synchronous and asynchronous spikes.

`lfp``()`

lfp(interneurones, filter, fx, fy)

Compute LFP on decimated grid from IN activity and filter.

Parameters

interneurones [ndarray of shape (nt, ny, nx)] firing rates of interneurones

filter [ndarray of shape (ny, nx)] must zero-pad to match shape of IN grid

fx [int] decimation factor for x-axis. Must divide nx. **Attention:** order of axes is y, x!

fy [int] decimation factor for y-axis. Must divide ny. **Attention:** order of axes is y, x!

Returns

lfps [ndarray of shape (nt, ny/fy, nx/fx)] the local field potential, obtained from interneurone activity by spatially filtering and decimating

`train_to_Dirac``()`

train_to_Dirac(trains, dt, nt, lower=0.0, axis=-1, interpolate=1)

Convert spike trains to sums of "Dirac functions".

Parameters

trains [ndarray of dtype object] spike trains; each train is either None or an iterable returning spike times

dt [float] size of time bins to use in output array

nt [int] number of time bins to use in output array

lower [float] left boundary of first time bin

axis [int] index of dimension where to insert time axis in output

interpolate [int] whether to linearly interpolate (1: yes, 0: no); if yes, a rectangle of width dt centred at spike time is tallied to the nearest bins according to area of overlap

Returns

Dirac [ndarray of dtype double] array of instantaneous firing rates with time resolution dt; array has shape of trains with time axis inserted as dimension no. axis

exception **`error`**

Bases: `exceptions.Exception`

`synapse_descriptor`

a numpy dtype with fields

'delay' : float

'target' : object

'type' : int

'weight' : float

used for synapses and events

note that itemsize is larger than sum of field sizes

`FIRST_SYN=5`

synapse count starts here

`MAX_WEIGHT_GROUP=5`

maximum number of state variables permissible in voltage mechanisms

Index

CV Martin Takeo Wiechert

*23.8.1973	Rüsselsheim, Hessen
1980-1984	Grundschule Frauenaurach (primary school)
1984-1993	Gymnasium Fridericianum Erlangen (grammar school)
1993	Abitur (≈ A-levels)
1998-2003	In 1998 I enrolled with the University of Bonn where I studied mathematics. In my Diplom (≈ MSc) thesis I carried out a number of biophysical calculations on vesicle transport by kinesin. I prepared it under the supervision of Prof. Wolfgang Alt and received my degree in 2003.
2003-2010	In 2003 I joined Dr. Rainer Friedrich's group at the MPI for medical research in Heidelberg. Combining computational modelling and mathematical analysis I investigated how the primary neural representation of odours is reformatted in the olfactory bulb. In 2007 Dr. Friedrich accepted a position at FMI in Basel and the laboratory relocated. I received my PhD on the 29th of November 2010.

Peer reviewed publications

[1] R.W. Friedrich, E. Yaksi, B. Judkewitz, and M.T. Wiechert. Processing of odor representations by neuronal circuits in the olfactory bulb. *Annals of the New York Academy of Sciences*, 1170(International Symposium on Olfaction and Taste):293–297, 2009.

[2] S.D. Wick, M.T. Wiechert, R.W. Friedrich, and H. Riecke. Pattern orthogonalization via channel decorrelation by adaptive networks. *Journal of computational neuroscience*, 28(1):29–45, 2010.

[3] M.T. Wiechert, B. Judkewitz, H. Riecke, and R.W. Friedrich. Mechanisms of pattern decorrelation by recurrent neuronal circuits. *Nature neuroscience*, 2010.
evaluated in:
L Maler. "This landmark paper demonstrates that standard neuron dynamics and network architecture can decorrelate patterns of [...]". *Faculty of 1000*, 16 Nov 2010. http://F1000.com/6053956.

Talks

[4] M.T. Wiechert and R.W. Friedrich. Neural computations in the olfactory bulb: from physiology to mathematical analysis of neural circuits. Talk at the FMI annual meeting, Sep 2007.

[5] M.T. Wiechert and R.W. Friedrich. Generic computational features of olfactory bulb-like networks. Invited talk at the 4th Giessbach meeting, May 2008.

[6] M.T. Wiechert and R.W. Friedrich. Pattern separation in the olfactory bulb by a generic mechanism in recurrent networks. Talk at the Swiss chemosensory meeting, Nov 2009.

[7] M.T. Wiechert, B. Judkewitz, H. Riecke, and R.W. Friedrich. Pattern separation by recurrent neuronal circuits: structure-function relationships. Invited talk at the Bench to bedside symposium, Jan 2010.

[8] M.T. Wiechert, B. Judkewitz, H. Riecke, and R.W. Friedrich. There's not two fat guys, there's only one and he's not fat! Why sparse is beautiful. Invited talk at the 4th INI/HIFO symposium "Neuroscience through the ceiling", Jul 2010.

[9] E. Yaksi, M.T. Wiechert, and R.W. Friedrich. Processing of odor-evoked activity patterns in the olfactory bulb. Invited talk at the XVIIth congress of the European chemoreception research organisation, Sep 2006.

Poster presentations

[10] M.T. Wiechert and R.W. Friedrich. Influence of connectivity on computational properties of OB-like networks, Nov 2007. Poster presentation at SfN's 37th annual meeting.

[11] M.T. Wiechert, C.J. Habermann, G. Laurent, and R.W. Friedrich. Multiplexing using synchrony in the zebrafish olfactory bulb, Oct 2004. Poster presentation at SfN's 34th annual meeting.

[12] M.T. Wiechert, B. Judkewitz, and R.W. Friedrich. Dynamic computations in network models of the olfactory bulb, Mar 2005. Poster presentation at Cosyne 05.

[13] M.T. Wiechert, B. Judkewitz, and R.W. Friedrich. Dynamic computations in network models of the olfactory bulb, Mar 2005. Poster presentation at the 6th Göttingen meeting of the German neuroscience society.

[14] M.T. Wiechert, B. Judkewitz, and R.W. Friedrich. Noise-tolerant pattern separation by recurrent neuronal networks, Oct 2009. Poster presentation at EMBO conference "The assembly and function of neuronal circuits".

[15] M.T. Wiechert, B. Judkewitz, H. Riecke, and R.W. Friedrich. Mathematical analysis of noise-tolerant pattern separation in the olfactory bulb and other brain areas, Oct 2009. Poster presentation at SfN's 39th annual meeting.